The metallic alloy FeRh undergoes a phase transition from an antiferromagnetic phase (AFP) to a ferromagnetic phase (FP) when heated above 400 K. The change in magnetic order results in a change in the net magnetization of the system from zero up to 1.2 kA/m after increasing the system temperature. This is an uncommon characteristic for a magnetic material since usually one observes a decrease of the magnetization upon heating. This discloses the possibility to apply FeRh to Heat-Assisted Magnetic Recording (HAMR) devices.

Universitätsverlag Regensburg

ISBN 978-3-86845-104-7

gefördert von:

Alumni der physikalischen Fakultät der Universität Regensburg e.V.

Universität Regensburg

Dissertationsreihe Physik - Band 36

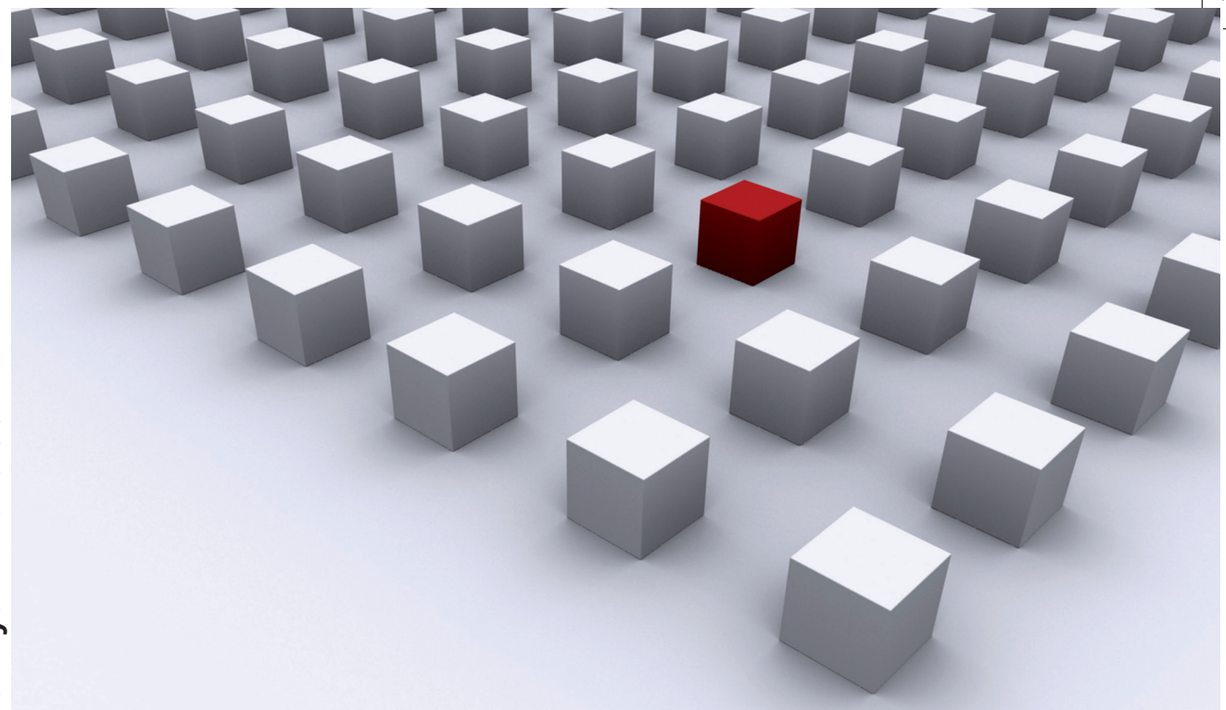

Federico Pressacco

Magnetization Dynamics across the First Order Phase Transition in FeRh Thin Films

Universitätsverlag Regensburg

Federico Pressacco

36

Dissertationsreihe Physik

Federico Pressacco

Magnetization Dynamics across the First Order Phase Transition in FeRh Thin Films

Magnetization Dynamics across the First Order Phase Transition in FeRh Thin Films

Dissertation zur Erlangung des Doktorgrades der Naturwissenschaften (Dr. rer. nat)
der Fakultät für Physik der Universität Regensburg
vorgelegt von

Federico Pressacco
Trieste
2013

Die Arbeit wurde von Prof. Dr. C. H. Back angeleitet.
Das Promotionsgesuch wurde am 10.01.2013 eingereicht.

Prüfungsausschuss:	Vorsitzender:	Prof. Dr. J. Fabian
	1. Gutachter:	Prof. Dr. C. H. Back
	2. Gutachter:	Prof. Dr. F. J. Giessibl
	weiterer Prüfer:	Prof. Dr. D. Bougeard

Dissertationsreihe der Fakultät für Physik der Universtität Regensburg, Band 36

Herausgegeben vom Präsidium des Alumnivereins der Physikalischen Fakultät:
Klaus Richter, Anderas Schäfer, Werner Wegscheider, Dieter Weiss

Federico Pressacco

Magnetization Dynamics across the First Order Phase Transition in FeRh Thin Films

Universitätsverlag Regensburg

Bibliografische Informationen der Deutschen Bibliothek.
Die Deutsche Bibliothek verzeichnet diese Publikation
in der Deutschen Nationalbibliografie. Detailierte bibliografische Daten
sind im Internet über http://dnb.ddb.de abrufbar.

1. Auflage 2014

Leibnizstraße 13, 93055 Regensburg

Konzeption: Thomas Geiger
Umschlagentwurf: Franz Stadler, Designcooperative Nittenau eG
Layout: Federico Pressacco
Druck: Docupoint, Magdeburg
ISBN: 978-3-86845-104-7

Weitere Informationen zum Verlagsprogramm erhalten Sie unter:
www.univerlag-regensburg.de

Contents

Motivation and Summary

The metallic alloy FeRh undergoes a phase transition from an anti-ferromagnetic phase (AFP) to a ferromagnetic phase (FP) when heated above 400 K. The change in magnetic order results in a change in the net magnetization of the system from zero up to 1.2 kA/m after increasing the system temperature. This is an uncommon characteristic for a magnetic material since usually one observes a decrease of the magnetization upon heating. This discloses the possibility to apply FeRh to Heat-Assisted Magnetic Recording (HAMR) devices. In those devices a laser pulse is used to locally and temporarily heat the system temperature in order to reduce the coercivity and hence making the magnetic switching easier[1]. In fact, FeRh can locally establish a magnetic field when driven into the ferromagnetic phase which can interact with the ferromagnetic recording element. To investigate the possibility of inducing ferromagnetic order and to determine the timescale of the transition we adopted a pump-probe scheme: a femtosecond laser pulse, the pump, is used to impulsively heat FeRh above the transition temperature and the subsequent dynamics is probed at different time delay after the excitation, by using, for example, a delayed laser pulse or an X-ray pulse as probe.

This work deals with the experimental investigation of the magnetization dynamics in thin films of FeRh. The main focus is in the possibility to generate ferromagnetic order and in determining the timescales at which the generation takes place. We performed pump-probe experiments where the excitation consists of 200 fs laser pulses at 800 nm which supplies the necessary energy to induce the transition. This allows us to detect and measure the temporal evolution of the dynamics triggered by the pump pulse.

The phase transition involves both the magnetic properties and the crystal structure of the system, implying a high degree of entanglement between electrons, atomic magnetic moments and phonons. In order to distinguish between the dynamics of the different systems involved, we used different probes. The magnetization dynamics has been investigated using the Magneto Optical Kerr Effect (MOKE). The probe consisted in the second harmonic of the laser pulse used to excite the system, which maintains the temporal characteristics of the fundamental, allowing a sub picosecond temporal resolution. The lattice dynamics has been addressed with the X-ray diffraction (XRD) technique, where

[1] for a review on the Heat-Assisted Magnetic Recording technology see for example Weller and Moser IEEE Vol.35, No.6, November 1999 "Thermal effect limits in ultra-high density magnetic recording", or Kryder *et Al* Proceedings of IEEE, Vol.96, No.11, "Heat Assisted Magnetic Recording"

the probe consisted of a 100 fs long pulse of coherent X-rays generated by a femto-slicing setup. From the comparison of the two measured dynamics we were able to determine the timescale of the different involved systems during the phase transition. Furthermore we supply a model able to explain the observed behaviors. We also demonstrate how it is possible to access the susceptibility of the system during the phase transition by measuring the magnetization curves during the development of the transition. This allows us to give a description of the influence of the external magnetic field on the onset of the ferromagnetic order.

We also addressed the magnetization dynamics by performing Ferromagnetic Resonance experiments across the phase transition. This technique allows to estimate the magnetic damping of the system and its anisotropies. This enables us to give a more detailed description of the system and on the response to external excitations.

The thesis is organized as follows:

Chapter 1 gives an introduction to the relevant physical concepts for this work. Since all the experiments have been performed on thin films of FeRh a particular attention is dedicated to the physical properties of this system.

Chapter 2 reports the different experimental techniques used in this work. The pump-probe experiments were all performed using a 800 nm laser pulse as source of the excitation. For this reason a brief description of the laser system is given. This allows us to introduce the experimental scheme used for the generation of ultrashort X-ray pulses, namely the femto-slicing technique. Finally we present the Ferromagnetic Resonance setup.

Chapter 3 collects the description of the different samples used in this work along with a preliminary characterization.

Chapter 4 presents the results of the FMR experiments and gives a first characterization of the magnetization dynamics across the phase transition. The magnetic energy landscape and the magnetization damping are determined for the system in the ferromagnetic phase

Chapter 5 contains the results of the time-resolved MOKE and time-resolved XRD experiments. Since both the experiments are performed under the same initial condition and with the same excitation method, we can compare the magnetic and lattice dynamics, determining the time scales. We supply a model which can well describe both the measured dynamics.

Chapter 6 presents the results of the measurements of the magnetization curves of FeRh during the development of the transition and the influence of an external magnetic field.

Chapter 7 summarizes all the conclusions and briefly discuss possible outlooks.

Appendix A reports the study of the demagnetization as a function of fluence of the ferromagnetic FeRh.

Appendix B collects the XMCD-PEEM images take at different temperatures of FeRh which show the onset and the expansion of the ferromagnetic phase.

Chapter 1

Introduction

In this chapter the theoretical concepts touched in the present work are reported. Since all the reported experiments are performed on FeRh samples, particular attention will be dedicated to the physical properties of this system. In the first section the basic concepts of magnetism are reported, along with a description of different types of magnetic order relevant for this work and with an introduction to the magnetic hysteresis curves. The following section gives a definition of the different contributions to the total energy energy. It will be shown how the energy landscape determines the dynamics of the magnetization of the system. In Section 1.3 a classification of phase transitions is reported and the particular case of FeRh is presented. At last a review of concepts of all optical excitation scheme and related phenomenological models are reported.

1.1 Magnetism in matter

The fundamental object of magnetism is the magnetic moment $\bar{\mu}$. It is associated with the total angular momentum $\mathbf{J}$ which is the sum of the orbital component $\mathbf{L}$ and a spin component $\mathbf{S}$, namely

$$\mathbf{J} = \mathbf{L} + \mathbf{S} \tag{1.1}$$

The spin part is the intrinsic angular momentum of the electron and can be described only in quantum-mechanical terms [1]. In a magnetic solid atoms are present that show a net magnetic moment. The magnetization of the material is defined as the density of the magnetic moments per unit volume. Considering a volume V of a magnetic material containing a certain amount of atoms (magnetic and non magnetic), the following definition of the magnetization $\mathbf{M}$ holds

$$\mathbf{M} = \frac{1}{V} \sum_{V} \bar{\mu_{at}} \tag{1.2}$$

As a consequence the dimensions of $\mathbf{M}$ are $[\frac{A}{m}]$. The magnetization in the following chapters will be a function of space and time, $\mathbf{M} = \mathbf{M}(\mathbf{r}, \mathbf{t})$.

1.1.1 Magnetic order

A magnetic material can show long range magnetic order. This means that the magnetic moments of the atoms in the material have spontaneously a preferred orientation. There are three players that determine this order. First the interaction of atomic moments with an external field, second the interaction of the magnetic moments among themselves and last the agitation of the magnetic moments due to non zero temperature. The first two tend to align the atomic moments along a certain direction while the latter tends to destroy any long range order by inducing a random orientation of each single moment. These are not all the aspects that can influence the orientation of the atomic moments, and further ones will be discussed later in this chapter. The interplay of the three contribution gives origin to different patterns of magnetic order. In FeRh the phase transition changes the magnetic order. We will show in the following chapters how the system can be driven from an Anti-Ferromagnetic Phase (AFP) to a Ferromagnetic Phase (FP) when raising the temperature. Furthermore we will show how, under certain experimental conditions, the system behaves as a paramagnet.

Paramagnetism

If the system has a non zero temperature ($T \neq 0$), and there is no interaction among the atomic moments or the interaction is too weak to overcome the thermal agitation, the atomic moments will be randomly oriented and the macroscopic value of the magnetization will be zero. The application of an external field H_{ext} tends to align the atomic moments inducing a non-vanishing magnetization. A magnetic material is called linear isotropic if the induced magnetization is proportional to the external field:

$$\mathbf{M} = \chi \mathbf{H}_{eff} \tag{1.3}$$

where the proportionality constant χ is the magnetic susceptibility, which is dimensionless. The application of a strong field will align all the atomic moments in the material and any further increase in the intensity of the field will have no effect on the magnetization. The material has reached the saturation magnetization $\bar{M}_s = n\bar{\mu}$, where n is the atomic density ($n = \frac{N}{V}$). The classical description of paramagnetism is due to Langevin. He assumed that the atomic moments in a material are free to rotate when put into an external field. From a quantum mechanical point of view the components of the magnetic moment are quantized and J can only assume discrete values either integer or half-integer. The theory developed by Langevin set J=∞, and is often referred to as the classical limit of paramagnetism [2]. It can be show that the magnetization is a function of the external field **B** and of the temperature, and can be written in term of the Langevin function L(y) as follows

$$M = M_S L(y) \tag{1.4}$$

where

$$L(y) = \coth(y) - (\frac{1}{y}) \tag{1.5}$$

and

$$y = \frac{\mu_b B}{3k_b T} \tag{1.6}$$

μ_B is the Bohr magneton and k_b is the Boltzmann constant. For the derivation and a more detailed discussion on the semiclassical treatment of paramagnetism and on the derivation of the Langevin function see [3]. The Langevin theory is successfully applied in systems such as diluted suspensions of ferromagnetic particles in non magnetic matrixes. In this case each particle has a macroscopic magnetic moment which can assume every orientation with respect to the external field. We will see how a similar situation can be found in thin films of FeRh under certain experimental conditions. This behavior is called paramagnetism, where the prefix "para" expresses the tendency of the atomic moments to align parallel to the external field (diamagnetism is the phenomenon where the atomic moments tend to align antiparallel to the external field).

Ferromagnetism

In the paramagnetic case at each temperature different from zero, if no external field is applied, the net magnetization will be zero across the material volume. If the atomic moments interact with one another then a spontaneous magnetization can arise for temperature $0 < T < T_C$ even if no external field H_{ext} is applied. This phenomenon is called ferromagnetism and T_C is the Curie temperature. In this case two types of interaction play a major role: the dipolar interaction and the exchange interaction. The dipolar interaction originates from the electromagnetic field generated by the atomic moments [4] and is weak with respect to the thermal agitation and the exchange interaction [3], but due to its long-range nature plays an important role for domain formation (see the section on the hysteresis). The exchange is a short range interaction that usually is effective within few interatomic distances, but which is much stronger than the dipolar interaction. If $T > T_C$ the material is in a paramagnetic state in which even if the exchange is still present, the thermal agitation randomly orients the magnetic moments. The exchange interaction is a consequence of the Pauli exclusion principle and of the Coulomb interaction between electrons of neighboring atoms. It can be understood and described only with quantum mechanics and is usually the dominating mechanism [5, 6]. Heisenberg has given a hamiltonian for a ferromagnetic material in which the spins of the first nearest neighbor atoms interact via an exchange constant [2]

$$\mathcal{H} = -2 \sum_{i>j} \mathcal{J}_{ij} \mathbf{S}_i \cdot \mathbf{S}_j \tag{1.7}$$

where i and j denote two neighboring lattice sites, $\mathcal{J}$ is the exchange integral, and $\mathbf{S}_{i,j}$ are the spins of the atoms. In this model the atoms are supposed to show only a spin

magnetic moment. This is particulary true for 3d metals where the presence of the internal crystal field quenches the orbital part of the total magnetic moment almost completely (for a more detailed discussion on the orbital quenching see for example Blundel's book "Magnetism in condensed matter" or Ashcroft-Mermin book "Solid state physics" [3, 7]). For ferromagnetic materials the integral $\mathcal{J}$ is positive. Hence the spin configuration that minimizes the energy (the expectation value of the Heisenberg hamiltonian on the ground state wavefunction) corresponds to the configuration in which all the spins are parallel aligned.

Antiferromagnetism

If the exchange integral is negative, $\mathcal{J} < 0$, the spins have to align antiparallel to each other in order to minimize the energy given by Eq.1.7. In this case, the formation of long range order is more complex and depends strongly on the boundary conditions and on the lattice structure. For example, in the case of a cubic lattice such as face-centred-cubic (fcc) or body-centred-cubic (bcc), the orientation of one atomic spin is indeed antiparallel with respect to all his nearest-neighbors. An anti-ferromagnet can be seen as composed by two interpenetrating ferromagnetic sublattices of opposite orientation. The macroscopic effect of anti-ferromagnetic order is that the net magnetization is identically zero across the volume of the material: $\mathbf{M}(\mathbf{r}) = 0$. As in the ferromagnetic case, order is established if $0 < T < T_N$, where T_N is the Neel temperature, which plays the same role as the Curie temperature for ferromagnetic materials. In response to the application of an external field to a anti-ferromagnetic material below T_N depends on the orientation and on the intensity of the field. If the field is applied perpendicular to the direction of the magnetic moments, it will induce the moments to rotate in order to align with the external field. However this mechanism is quite inefficient, because the exchange interaction, which is the dominating interaction, require fields of several Tesla to be overcome.

1.1.2 Hysteresis in Magnetic Materials

A ferromagnetic material picked randomly at a temperature below T_C will usually show no net macroscopic magnetization. In fact the system divides into regions of uniform magnetization called magnetic domains, but the orientations of the magnetization of different domains are randomly distributed. The regions are separated by domains walls. The formation of domains results from the balance of different competing energy contributions like the magnetic exchange which tends to orient every magnetic moment parallel to one another, the magneto-crystalline anisotropy which favors the alignment along a certain crystallographic direction and the dipolar interaction which, even if it is small compared to the others, favors a configuration where the net magnetization is zero [8]. The application of an external field can alter the established equilibrium configuration by making the domains showing a local magnetization aligned in the direction of the external

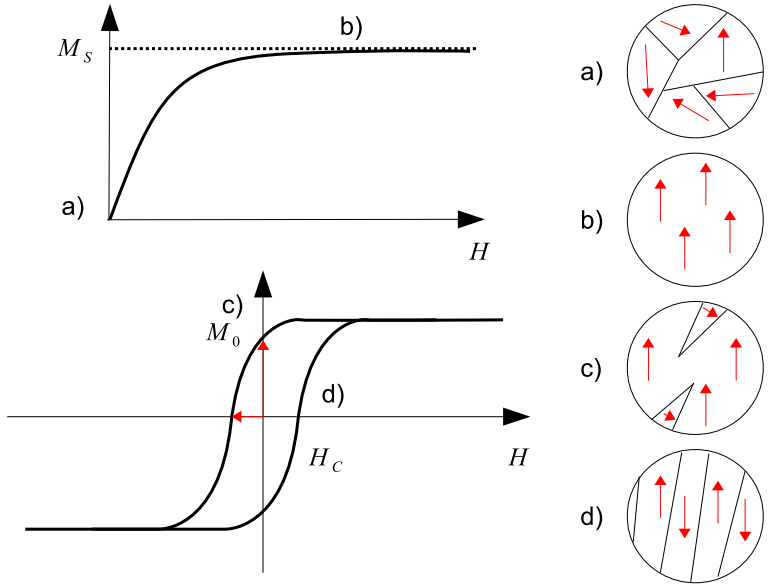

Figure 1.1: Top: Schematic of a virgin curve of a ferromagnetic material. Each single ferromagnetic domain has a magnetization with a random orientation regardless of the anisotropy. (a) If no external field is applied the average magnetization is zero. (b) The application of an external field H makes the domains with the magnetization parallel to H energetically favored, inducing an expansion of those domains. When all the magnetic moment are aligned the magnetization reaches its maximum M_s. (c) If the field H is set to zero most of the moments remain aligned but there is a nucleation of domains with a misaligned magnetization, $M = M_0 < M_S$. (d) For $H = -H_c$ half of the material has a magnetization directed opposite to the saturation direction and $M = 0$.

field energetically favored. The presence of the field will induce the motion of the domain walls so that some domain will expand while others will shrink [9][7]. If the field is strong enough the expansion of the domains will be irreversible, and at the end the entire material volume will be a unique coherent domain. When the system is in this configuration it is said to be saturated. The process is depicted in the top part of Fig.1.1. Starting from a magnetic configuration where the local magnetization of the domains averages to zero, the presence of the external field will induce macroscopic magnetization until saturation ((a) and (b) in Fig.1.1). If one plots the value of the magnetization versus the applied field during this process one obtains the "virgin curve" of the material. Once the system is in the saturated state, by reversing the orientation of the external field and by keeping

its intensity large enough, it is possible to reverse the orientation of the magnetization of the material. This process is called magnetic switching. By measuring the value of the magnetization of the material as a function of the external field one obtains the so called hysteresis loop, sketched in the bottom part of Fig.1.1. Two quantities can be extracted from the hysteresis loop: the remanence magnetization M_0 and the coercive filed H_c. M_0 is the magnetization obtained when the external field is set to zero after having saturated the sample and is usually of the order of magnitude of M_s. The coercive field H_c is the field necessary to set the magnetization to zero. By reversing the direction of the external field $\mathbf{H}$, domains with opposite direction of the magnetization will nucleate in the sample and will start to expand since they are energetically favored. When they occupy exactly the half of the sample volume the total magnetization will be zero. The intensity of $\mathbf{H}$ needed to reach this configuration is called the coercive field. Its value depends on how mobile the domains walls are, and can range from few $[A/m]$ for soft magnetic materials to $10^6\,[A/m]$ for permanent magnets.

1.2 Magnetic energy and magnetization dynamics

1.2.1 Energy in magnetic materials

The total energy per unit volume of a magnetic material can be written as the sum of different contributions.

$$E_{tot} = E_a + E_z + E_{ex} + E_d \tag{1.8}$$

The first term is the anisotropy contribution to energy. In most of the magnetic material there are preferred directions for the magnetization. The orientation of this direction reflects the symmetry and the band structure of the underlying crystal, and one can distinguish between uniaxial, cubic and orthorhombic. For the FeRh compound the cubic anisotropy plays a major role. It is convenient to write the cubic anisotropy term as

$$E_a = -\frac{K_1^{||}}{2}(\alpha_x^4 + \alpha_y^4) - \frac{K_1^{\perp}}{2}\alpha_z^4 - K_U^{\perp}\alpha_z^2 - K_U^{||}\frac{(\hat{\mathbf{n}}\cdot\mathbf{M})^2}{M_s^2} \tag{1.9}$$

where $K_1^{||}$,$K_1^{\perp}$,$K_U^{||}$, and $K_U^{\perp}$ are the constants that describes the strength of uniaxial and fourfold anisotropy. The and α_i are the direction cosines of $\mathbf{M}$ along the crystallographic axes [100], [010] and [001]. $\hat{\mathbf{n}}$ is the unit vector along the in-plane uniaxial anisotropy axes.

The second term is called the Zeeman term and originates from the interaction of the magnetization with an external field

$$E_z = -\mu_0 M_s \int_V \mathbf{M}\cdot\mathbf{H}_{ext}dV \tag{1.10}$$

The alignment of the magnetization with the external field is favored since the Zeeman energy reaches a minimum.

The third term is the exchange contribution which originates from the interaction of the spins among themselves. The energy contribution can be calculated starting from Eq.1.7, and, in a continuum model, it can be written as

$$E_{ex} = A \int_V (\nabla \mathbf{M}^2 dV) \tag{1.11}$$

where the integral extends only on the sample because the magnetization is zero elsewhere and A is the magnetic exchange stiffness which is a constant proportional to the exchange constant $\mathcal{J}$ [9, 3].

The last term is the demagnetizing energy contribution. At the boundaries of a finite volume material the perpendicular component of the magnetization generates magnetic surface charges, the density of which is proportional to the divergence of $\mathbf{M}$. The distribution of these charges generates a demagnetizing field $\mathbf{H}_d$ [4]. Since $\nabla \cdot \mathbf{B} = 0$ and $\nabla \cdot \mathbf{B} = \mu_0(\nabla \cdot \mathbf{H} + \nabla \cdot \mathbf{M})$, the following relation holds

$$\nabla \cdot \mathbf{H}_d = -\nabla \cdot \mathbf{M} \tag{1.12}$$

showing that the demagnetizing field $\mathbf{H}_d$ is directed opposite to the magnetization. The energy contribution of of the demagnetizing field can be calculated as follows

$$E_d = \frac{1}{2}\mu_0 \int_{space} \mathbf{H}_d^2 dV = -\frac{1}{2}\mu_0 \int_{sample} \mathbf{M} \cdot \mathbf{H}_d \tag{1.13}$$

where the last step is valid because the magnetization is zero outside the sample. The determination of the intensity and the direction of $\mathbf{H}_d$ for a sample of arbitrary shape is non trivial. On the other hand it is simple in the case of an ellipsoidally shaped magnetic material with a uniform magnetization. In this case assuming that the axes of the ellipse are directed along the cartesian axes, the demagnetizing field can be calculated as

$$\mathbf{H}_d = -\hat{N}\mathbf{M} \tag{1.14}$$

where $\hat{N}$ is known as the demagnetizing tensor [3]. If $\mathbf{M}$ is parallel to one of the axes, the tensor can be diagonalized:

$$\hat{N} = \begin{pmatrix} N_x & 0 & 0 \\ 0 & N_y & 0 \\ 0 & 0 & N_z \end{pmatrix} \tag{1.15}$$

where $N_{x,y,z}$ are the demagnetizing factors which have to satisfy the condition $Tr\hat{N} = 1$. In the present work the samples consist of thin films. They can be considered as ellipses with two infinity axes (lets say $\hat{x}$ and $\hat{y}$) and one vanishing axes ($\hat{z}$). In this case the demagnetizing factors are $N_x = N_y = 0$ and $N_z = 1$ [8, 4]. If the magnetization lies in

the xy-plane no demagnetizing field is present. If the magnetization has a z-component different from zero, a demagnetizing field proportional to the z component tends to force the magnetization to lie in the film plane.

In general, the equilibrium direction of the magnetization will be obtained by minimizing the total energy functional. In particular the functional can be written as $E_{tot} = -\mu_0 \mathbf{M} \cdot \mathbf{H}_{eff}$, where $\mathbf{H}_{eff}$ is an effective field and the energy will be minimal if $\mathbf{M}$ and $\mathbf{H}_{eff}$ are parallel. The effective field can be calculated from

$$\mathbf{H}_{eff} = -\frac{1}{\mu_0} \nabla_{\mathbf{M}} E_{tot} \tag{1.16}$$

and remembering Eq.1.8, the effective field can be seen as the sum of different fields

$$\mathbf{H}_{eff} = \mathbf{H}_z + \mathbf{H}_{ex} + \mathbf{H}_a + \mathbf{H}_d \tag{1.17}$$

If an external excitation induces a change in one of this field, the effective field will change its orientation and it will be no longer parallel to the magnetization. To minimize again the total energy of the system the magnetization will rotate until the new equilibrium position is reached.

1.2.2 Magnetization dynamics and damping

Suppose to have a saturated magnetic material. The time evolution of the magnetization has been addressed for the first time by Landau and Lifshitz in 1935 [10] by proposing the so called Landau-Lifshitz equation (LL)

$$\frac{d\mathbf{M}}{dt} = \gamma \mu_0 (\mathbf{M} \times \mathbf{H}_{eff}) + \frac{\lambda}{M_S^2} (\mathbf{M} \times (\mathbf{M} \times \mathbf{H}_{eff})) \tag{1.18}$$

where $\gamma = \frac{g|e|}{2m_e}$ with e the electron charge, m_e the electron mass, $g = 2.0023$ the g-factor of the free electron, and λ a phenomenological parameter with the dimensions of an inverse time. The field $\mathbf{H}_{eff}$ has been introduced in Eq.1.16. It can be seen that in Eq.1.18 only the $\mathbf{H}$ fields can be use by the virtue of $\mathbf{B} = \mu_0(\mathbf{H} + \mathbf{M})$. This equation has been modified by Gilbert in 1956 with the introduction of a damping term depending on the time derivative of the magnetization itself. This equation is known as Landau-Lifshitz-Gilbert equation (LLG) [11] and can be written as:

$$\frac{d\mathbf{M}}{dt} = \gamma \mu_0 (\mathbf{M} \times \mathbf{H}_{eff}) + \frac{\alpha}{M_S} (\frac{d\mathbf{M}}{dt} \times \mathbf{M}) \tag{1.19}$$

The first term on the right hand side is the precessional term while the second is the damping term. α is a dimensionless parameter known as damping constant. The damping term is both perpendicular to $\mathbf{M}$ and $\frac{d\mathbf{M}}{dt}$, and tends to align the magnetization along $\mathbf{H}_{eff}$, see Fig.1.2.

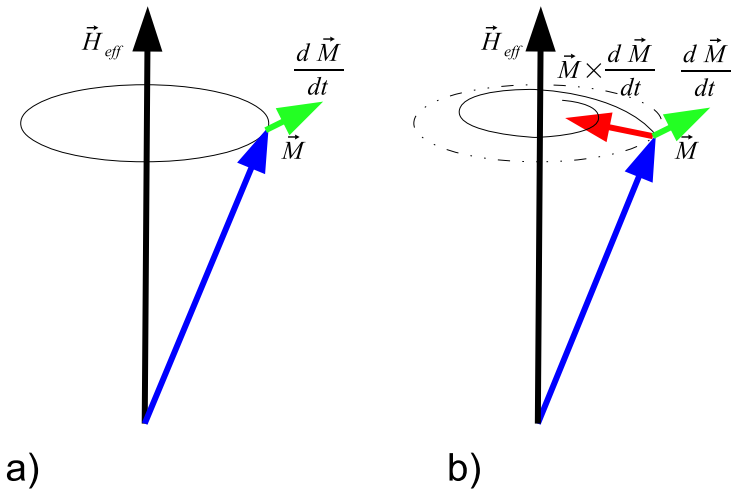

Figure 1.2: a. In absence of a damping mechanism the magnetization will precess around the $\mathbf{H_{eff}}$ at a constant frequency. b. The Gilbert damping term point toward $\mathbf{H_{eff}}$ inducing a relaxation to the low energy configuration where $\mathbf{H_{eff}}$ and $\mathbf{M}$ ar parallel.

The relaxation of the magnetization precession in real materials is an unavoidable process, and its efficiency is summarized by the parameter α. The magnetic damping is sample dependent and mostly does not reflect the intrinsic properties of the material [12]. Nevertheless one can distinguish between intrinsic and extrinsic damping. The intrinsic damping is due to unavoidable processes such as eddy currents, phonon drag, spin-orbit coupling and intra- and inter-band transitions. The extrinsic damping is mainly due to the finite sizes of the sample, or structural inhomogeneities or defects. Usually one refers to the damping of a material as the minimum measured value of α for that material.

1.3 Phase Transitions in magnetic materials: the FeRh case

In this section basic concepts of phase transition theory will be briefly resumed. In particular the concepts of "order parameter", transition order.

A system in thermodynamic equilibrium will occupy a state in which the free energy

$\mathcal{F}$ is minimal [13]. The free energy is a thermodynamical potential which is function of temperature T, pressure P, and number of particles N. The thermodynamical state of the system is defined by those quantities. A first attempt to model phase transitions is the phenomenological theory[1] of Landau [10]. The free energy is written as a function of an order parameter ϕ , defined so that it is zero in the initial phase, which is an equilibrium state of the system. Hence, $\mathcal{F}$ has to show a minimum at $\phi = 0$. It has to be possible to expand the free energy around this minimum in powers of the "order parameter". In the Landau theory the free energy is also a function of a field H which is conjugate to the order parameter as a natural variable [14],

$$\phi = -\left(\frac{\partial \mathcal{F}}{\partial H}\right)_T \tag{1.20}$$

The Landau free energy is also a function of the temperature T which is the conjugate variable of the entropy $S = -\left(\frac{\partial \mathcal{F}}{\partial T}\right)_H$, while the dependence on the pressure and on the density is neglected.

The order of the phase transition is defined in terms of the continuity of the order parameter ϕ and its derivatives, as a function of the temperature. If the order parameter is discontinuous then the transition is said to be of first-order, if the first derivative of the order parameter is discontinuous the transition is said to be of second-order, and so on. The temperature at which the discontinuity occurs determines T_t. Examples of transition temperatures are the afore mentioned Curie Temperature T_C for ferromagnets, the Neél temperature T_N for anti-ferromagnets which are related to a second order phase transition, and the freezing or the boiling temperature of water which are instead related to a first order phase transition.

We take now in consideration the case of FeRh. This system is a magnetic metallic alloy which has been studied for the first time 1939 by Fallot and Hocart [16]. The system shows different behavior as a function of the composition [17] and on the presence of different atomic species [15]. In this work we will investigate only the stoichiometric binary alloy $Fe_{50}Rh_{50}$. At room temperature this system shows an anti-ferromagnetic state where the magnetic moments are present only on the Fe ions and are antiferromagnetically coupled. By increasing the temperature the system undergoes a first order phase transition from the anti-ferromagnetic phase (AFP) to a ferromagnetic phase (FP). In this case the magnetization plays the role of the order parameter and in the transition it changes "abruptly"[2] from zero up to a maximum value of 1250 emu/cm^3. The system then behaves as a ferromagnet: when increasing the temperature, the magnetization decreases to zero when the Curie temperature is reached at T= T_C = 460 C. This is the well know second order phase transition from a ferromagnetic phase to the paramagnetic phase (PP). In Fig.1.3 the magnetization is plotted as a function of temperature (measurement made by

[1] see later in this chapter for a definition of "phenomenological theory"

[2] A more detailed description of the phase transition can be found in the chapter where the samples characteristics are decribed

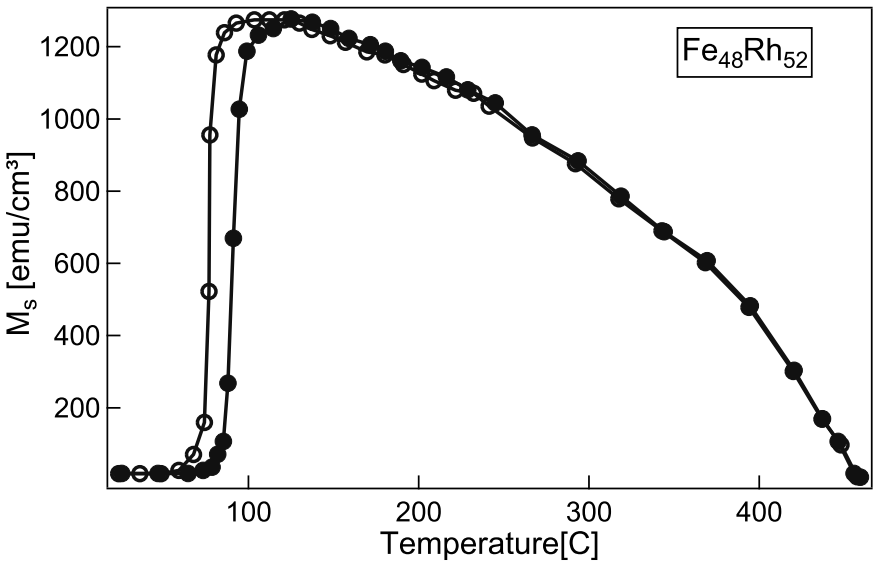

Figure 1.3: Temperature dependence of the saturation magnetization of a 700$\mathring{A}$ thick film of $Fe_{48}Rh_{52}$ upon heating above the Curie temperature and following cooling back to room temperature. The two phase transition are clearly indicated. Picture from [15].

Thiele and coworkers [15]). The existence of two temperature dependent phase transitions of different order is a very particular aspect of this system. This makes it suitable for the investigation of the physical mechanisms responsible for the phase change. Further more it discloses the possibility of generating magnetic order corresponding to a net magnetization by increasing the temperature of the system, while a common ferromagnetic system shows the opposite behavior.

1.4 Laser induced dynamics: a phenomenological approach

Most of the experiments presented in this work make use of a laser pulse as a source of energy to excite the system. The understanding of the triggered processes requires that the electronic and atomic configuration of the system are known. Furthermore the comprehension of the dynamics requires a detailed knowledge of the interaction of the photons with the electrons of the system during the excitation and of the interaction of

the electrons with the ions and with themselves during the relaxation (namely after the interaction of the laser pulse with the system). It can be easily understood that to give a complete quantum-mechanical description of the system is a formidable task, which goes far beyond our ability of solving the equations governing such processes either analytically or numerically. Nevertheless we need a model that allows us to make predictions of the results of our experiments, and following what we said before such a model has necessarily to be phenomenological. With the term "phenomenological" we intend a model which can give a qualitative and quantitative mathematical description of some observed phenomena, within the framework of a theory, in terms of quantities not directly calculated from the principles of that theory[3]. For example, thermodynamics is a phenomenological description of heat transfer process within the framework of statistical mechanics.

The models we will use are based on the concept of thermal bath (in literature sometimes referred to as heat reservoir). A thermal bath accounts for a part of the system, or for the ensemble of one kind of particles (electrons) or quasi-particles (e.g. phonons) present in the system, by assigning to it a temperature T_i and a heat capacity C_i. The concept of temperature is however related to an equilibrium state of the considered subsystem. We can assign properly a temperature to a subsystem if it obeys Fermi-Dirac (FD) statistics in case of fermions (electrons) or Bose-Einstein statistics in case of the bosons (phonons, magnons). We will see that the validity of the temperature assignment depends on the timescale at which the dynamics is observed. The thermal bath is then put in contact with the other ones and with the surrounding environment via coupling terms g_{i-j}. The dynamics of the system is then written in term of coupled differential equations. The variables of these equations are the temperatures T_i, while the heat capacities and the coupling constants are the coefficients of the equations.

The strongest assumption is that the status of the subsystem is fully given by its temperature T_i which is taken as the variable in the equation system governing the dynamics. C_i and g_{i-j} are the aforementioned "quantities" not calculated from the principles of the theory and their value is chosen so that the solutions of the equations is in good agreement with the results of the experiments.

In the following sections we present two models that are widely used to describe the dynamics triggered by a laser pulse in a metal and in a magnetic system. Even if they are the results of crude approximations, it turns out that their predictions are in good agreement with the experimental results.

Both models share how the excitation is modeled: since the status of the system is given by its temperature, the laser excitation is put into the equation system as a heat source with a temporal dependence given by the laser temporal profile. Moreover since the photons interact with the electrons, the heat source term will be present only in the equation related to the electronic system. The energy absorbed will then be redistributed to the other subsystems via the coupling terms in the differential equations.

[3]Definition of "phenomenology" according to [18]:"A theory that expresses mathematically the results of observed phenomena without paying detailed attention to their fundamental significance."

Two Temperature Model

In the case of a non-magnetic metal, one usually describes the laser-induced dynamics with a Two-Temperature Model (2TM) originally proposed by Anisimov and coworkers [19]. In this model only electron and phonons are present, and both are described as thermal baths with temperatures T_e and T_p, heat capacities C_e and C_p, and obeying to FD and BE statistics, respectively. Before the optical excitation both systems have the same temperature $T_{p,i}$=$T_{e,i}$, which is equal to the ambient temperature. The heat capacities (and eventually their dependence on temperature) of the two subsystems are usually derived by the Sommerfeld model of a free electron gas for the electronic subsystem and from the Debey model for phonons [7].

The optical excitation delivers its energy to the electronic system, and since the photon energies in most experiments range from 1.58 to 3.16 eV, which are hundred time k_bT at room temperature, it induces a non-thermal distribution of the electrons by populating electronic levels far above the Fermi energy (E_F). The non-thermal electrons created by the optical excitation start to thermalize due to electron-electron scattering. This process, mediated by the Coulomb interaction, redistributes the electronic population as dictated by a FD statistics compatible with a higher electronic temperature. The lifetime of the non-thermal electrons has been estimated to be of the order of 10 fs for excitation of 1 meV [20], implying that the electron system thermalization takes place within few hundreds of fs [21, 22].

The high temperature of the electrons increases the probability of emission of phonons, hence the electron system starts to deliver energy to the lattice via the electron-phonon scattering process. The thermalization of the two subsystems takes from 0.5 ps for transition metals alloys [23] up to 2 picoseconds in pure metals [24, 25]. The two temperature model is well described by the following coupled equations:

$$C_e(T_e)\frac{\partial T_e}{\partial t} = \nabla k_e \nabla T_e - g_{e-p}(T_e - T_p) + P(t) \tag{1.21}$$

$$C_p(T_p)\frac{\partial T_p}{\partial t} = g_{e-p}(T_e - T_p) \tag{1.22}$$

where $C_{e,p}$ are the temperature dependent heat capacities of electrons and phonons, k_e is the thermal conductivity of the electronic system and g_{e-p} is the electron phonon coupling constant. The first term on the right-hand-side of Eq.1.21 accounts for the heat diffusion due to electrons in the sample volume, while the last term gives the power delivered by the laser pulse. In Eq.1.22 only the interaction term is present since the laser is fully absorbed by the electrons and the thermal conductivity of phonons is much smaller then that of electrons. The model seems to be oversimplified but it can well predict the electron and phonon dynamics in different metallic systems [26, 27, 28].

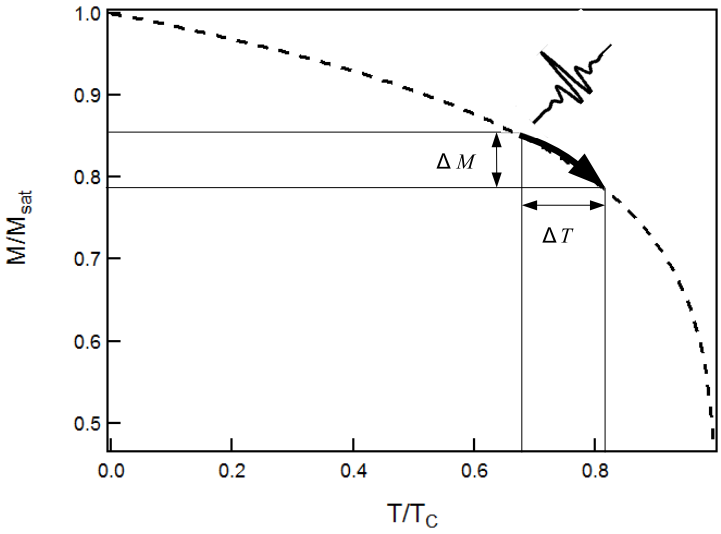

Figure 1.4: Schematic picture of the M-T curve of a conventional ferromagnetic material. The increase of temperature induced by the laser pulses corresponds to a decrease of the magnetization.

Three Temperature Model

In close relation with the assumptions of the 2TM, Vaterlaus and coworkers proposed a model that accounts for the spin dynamics of ferromagnets: the Three Temperature Model [29]. In this model, spins are introduced as a third thermal bath characterized by its own temperature T_s and heat capacity C_s. The temperature of the spin system determines the magnetic state of the material through the M(T) curve, and hence knowing the temporal dependence of the temperature one derives the dynamics of the magnetization: M(t)=M(T(t)), Fig.1.4. This approach was successfully used by Beaurepaire and coworkers in [30] and further by Hohlfeld and coworkers [31]. In that case, since the increase of the temperature induced a decrease in the magnetization, the phenomenon has been named laser induced demagnetization. In this case the model is described by a set of three coupled differential equations

$$C_e(T_e)\frac{\partial T_e}{\partial t} = \nabla k_e \nabla T_e - g_{e-p}(T_e - T_p) - g_{e-s}(T_e - T_s) + P(t) \tag{1.23}$$

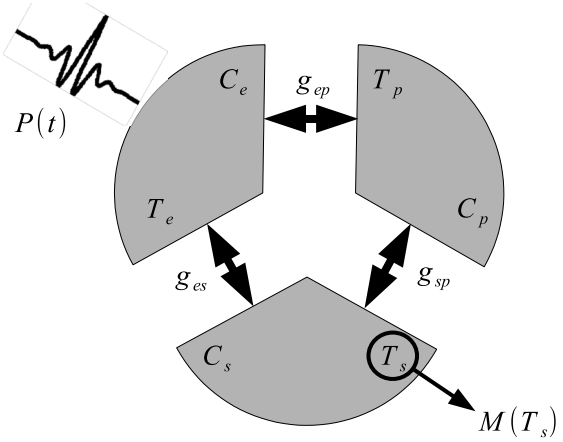

Figure 1.5: The three interacting heat baths of the Three Temperature Model.

$$C_p(T_p)\frac{\partial T_p}{\partial t} = g_{e-p}(T_e - T_p) + g_{p-s}(T_p - T_s) \tag{1.24}$$

$$C_s(T_s)\frac{\partial T_s}{\partial t} = g_{e-s}(T_e - T_s) + g_{p-s}(T_p - T_s) \tag{1.25}$$

Similarly to the two temperature model, the parameter g_{e-s} and g_{p-s} are the electron-spin and phonon-spin interaction constants and C_s is the heat capacity of the magnetic system. Also in this case the laser pulse interacts only with the electrons (the source term P(t) is present only in the first equation), the following thermal equilibration is up to the coupling term due to the mutual interaction of the subsystems, Fig.1.5. The determination of the coupling constants is of fundamental importance to apply the model to experimental data. Different strategies and approaches has been used to determine the coupling constants [32, 33, 34], producing model prediction in good agreement with the experimental data. However a definitive method to determine the coupling constant is still missing and the underlying physical origin of the coupling is still matter of debate.

References

[1] B. H. Bransden and C. J. Joachim. *Physics of atom and molecules.* Prentice Hall, second edition, 2003.

[2] J. M. D. Coey. *Magnetism and magnetic materials.* Cambrige University Press, 2010.

[3] S. Blundel. *Magnetism in condensed matter.* Oxford University Press, 2001.

[4] D. J. Griffiths. *Introduction to electrodynamics.* Prentice Hall, third edition, 1999.

[5] C. Kittel. Physical theory of ferromagnetic domains. *Rev. Mod. Phys.*, 21:541, 1949.

[6] R. E. Peierls. *Quantum Theory of Solids.* Oxford University Press, second edition, 1956.

[7] N. W. Ashcroft and N. D. Mermin. *Solid State Physics.* Thomson Learning, 1976.

[8] G. Bertotti. *Hysteresis in Magnetism.* Accademic Press, 1998.

[9] A. Huber and R. Schaefer. *Magnetic Domains- The analysis of magnetic microstructures.* Springer Verlag, 2000.

[10] L. D. Landau and E. Lifshitz. on the theory of dispersion of magnetic permeability in ferromagnetic bodies. *Phys.Z. Sowjetunion*, 8:153, 1935.

[11] T. L. Gilbert. *Formulation, fundation and application of the phenomenologial theory of ferromagnetism.* PhD thesis, Illinois Istitute of technology, 1956.

[12] B. Heinrich. Spin relaxation in magnetic metallic layers and multilayers. In *Ultrathin magnetic structures III.* Springer Verlag, 2005.

[13] K. Huang. *Statistical Machanics.* Weil, second edition, 1987.

[14] K. Binder. Theory of first order phase transitions. *Rep. Prog. Phys.*, 50:783–859, 1987.

[15] J.-U. Thiele, S. Maat, and E.E. Fullerton. FeRh/FePt exchange spring films for thermaly assisted magnetic recording. *Appl. Phys. Lett.*, 82(17):2859, 2003.

[16] M. Fallot and R. Hocart. Les alliages du fer avec les metaux de la famille du platine. *Rev. Sci.*, 77:498, 1939.

[17] Swartzendruber. L. J. The Fe-Rh (iron-rhodium) system. *Bulletin of Alloy Phase Diagrams*, 5(5):456, 1984.

[18] J. Thewlis. *Concise dictionary of physics.* Pergamon Press, 1973.

[19] S. I. Anisimov, B. L. Kapeliovich, and T. L. Perelman. Electron emission from metal surfaces exposed to ultrashort laser pulses. *Sov, Phys. JEPT*, 39:375, 1974.

[20] R. Knorren, K. H. Bennemann, R. Burgermeister, and M. Aeschlimann. Dynamics of excited electrons in copper and ferromagnetic transition metals: theory and experiments. *Phys. Rev. B*, 61:9427, 2000.

[21] B. Hillebrands and K. Ounadjela. *Spin Dynamics in confined magnetic structures 2.* Springer, 2003.

[22] H.-S. Rhie, H. A. Duerr, and W. Eberhaedt. Femtosecond electron and spiun dynamics in Ni/W(110) films. *Phys, Rev. Lett*, 90(24):247201, 2003.

[23] B. Koopmans, M. van Kampen, J. T. Kohlhepp, and de Jonge W. J. M. Ultrafast magneto-optics in Ni; magnetism or optics? *Phys, Rev. Lett*, 85:844, 2000.

[24] G. Grimwall. *The electron-phonon interaction in metals.* Norht Holland, 1981.

[25] J. Hohlfeld, S.-S. Wellershoff, J. Guedde, V. Jaenke, and E. Matthias. Electron and lattice dynamics following optical excitation of metals. *Chem. Phys*, 251:237, 2000.

[26] M. Hase, K. Ishioka, J. Demsar, K. Ushida, and M. Kitajima. Ultrafast dynamics of coherent optical phonons and nonequilibrium electrons in transition metals. *Phys, Rev. B*, 71:184301, 2005.

[27] H.E. Elsayed-Ali, T. B. Norric, M. A. Pessot, and G. A. Mourou. Time resolved observation of electron-phonon relaxation in copper. *Phys, Rev. Lett*, 58:1212, 1987.

[28] H. E. Elsayed Ali and T. Juhasz. Femtosecond time resolved thermomodulation of thin gold films with differnt crystal structures. *Phys, Rev. B*, 47:13599, 1992.

[29] A. Vaterlaus, T. Beutler, T. Guarisco, M. Lutz, and F. Meier. Spin-lattice relaxation in ferromagnets studied by time-resolved spin-polarized photoemission. *Phys. Rev. B*, 46:5280, 1992.

[30] E. Beaurepaire, J.-C. Merle, A. Daunois, and J.-Y. Bigot. Ultrafast spin dynamics in ferromagnetic nickel. *Phys. Rev. Lett*, 76:4250, 1996.

[31] J. Hohlfeld, E. Matthias, R. Knorren, and K. H. Bennemann. Nonequilibrium magnetization dynamics of nichel. *Phys, Rev. Lett*, 78(25):4861, 1997.

[32] J.-Y. Bigot, M. Vomir, and E. Beaurepaire. Coherent ultrafast magnetism induced by femtosecond laser pulses. *Nat. Mat.*, 5:515, 2009.

[33] B. Koopmans, G. Malinowski, F. Dalla Longa, D. Steiauf, M. Faehnle, T. Roth, M. Cinchetti, and M. Aeschliman. Explaining the paradoxically diversity of ultrafast laser-induced demagnetization. *Nat. Mat.*, 13:259, 2009.

[34] G. Malinowski, F. Dalla longa, J. H. H. Rietjens, P. V. Paluskar, R. Huijink, J.M. Swagten, and B. Koopmans. Control of speed and efficiency of ultrafast demagnetization by direct transfer of spin angular mementum. *Nat. Mat.*, 4:855, 2008.

Chapter 2

Experimental Techniques

In the present chapter the experimental techniques used in this thesis to investigate the dynamics in the system are reported and discussed. Description of the laser system used and of the pump-probe experimental framework are reported. In the present work the pump-probe experiments are all performed with an 800 nm laser pulse, that optically pumps the system, and different probes. The time resolved magneto-optical Kerr uses an optical probe, namely the second harmonic of the fundamental beam, while the time resolved X ray diffraction experiments use an ultrashort X-ray probe. As a complementary technique to access the dynamics of the system, the ferromagnetic resonance technique (FMR) has been used. FMR provides information on the magnetic damping and on the anisotropy of the system. The time-resolved MOKE and the FMR experiments have been performed at the University of Regensburg in the group of Prof. Dr. C.H. Back, while the time resolved X-Ray diffraction experiments have been performed at the Paul Scherrer Institute in Villigen (Switzerland) at the Femto beamline.

2.1 Laser systems

One of the fastest event available in experimental physics are laser pulses. The time duration of the pulses generated with a laser system ranges from hundred picoseconds (1 ps = 10^{-12}s) to hundreds of attoseconds (1 as=10^{-18} s). In this thesis most of the experiments have been performed with the laser radiation generated by a commercially available RegA-Mira system composed by the following units:

- Verdi V-5 diode pumped continuous wave Nd:YVO_4 laser;
- Mira 900 mode locked Ti:Sa laser;
- Verdi V-10 diode pumped continuous wave Nd:YVO_4 laser;
- RegA 9000 regenerative amplifier;

The system supplies radiation at 72 kHz of repetition rate (RR) composed of laser pulses less than 200 fs long, with a maximum energy and peak power of 5 μJ and 25 MW, respectively.

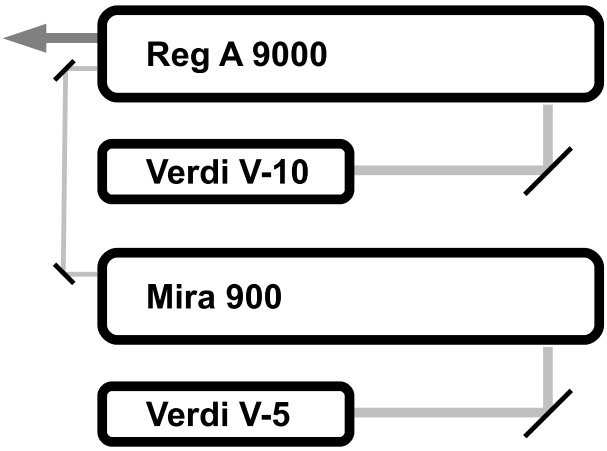

Figure 2.1: Scheme of the Mira-RegA amplified system. The continuous wave radiation (CW) generated by a Verdi-5V is used to produce the seed beam in a Mira 900. The seed is then passed to the RegA head where it is amplified by a CW beam from the Verdi-10V.

The scheme of the Mira-RegA amplified system is reported in Fig.2.1. The Mira 900 is a mode-locked Ti:sapphire laser [1] operating at 82 MHz repetition rate. The crystal amplifies the modes compatible with the cavity only in a bandwidth of about 350 nm around the central wavelength of 800 nm. This range is further reduced to less then 150 nm by the mirrors in the cavity and by a birefringent filter. In the Mira only one pulse of light is amplified. The pulse is initiated by an opto-mechanical modulator operating at a frequency which allows a single pulse of light to bounce back and forth once in the cavity. Such a procedure guarantees that the amplified modes are phase locked with respect to one another. The in-phase superposition of the modes present in the cavity gives origin to the formation of an ultrashort pulse [2]. This highly intense pulse passes through a Kerr lens which passively mode-locks the modes together. The Kerr lens focuses the beam onto an aperture, but does not change the diameter of the CW radiation present. This allows to separate the two components by changing the aperture of a slit. This gives rise to a self stabilized mode-locked pulsed radiation that no longer needs the opto-mechanical modulator. The Mira is optically pumped with a Verdi V5 diode laser that supplies a 5 W continuum radiation of 532 nm wavelength. The output of the Mira 900 enters the Reg-A 9000 which is a regenerative amplifier [3], optically pumped by a Verdi V10 diode laser

which supplies a continuum wave radiation of 10 W at 532 nm. The ultrafast pulses from the Mira are stretched and amplified in the RegA cavity. A Faraday insulator allows the seed pulse to reach a SiO_2 acusto-optic cavity dumper that injects it into the main cavity. The pulse is amplified after 20 to 35 round trips in the cavity. At this point the cavity dumper once again opens the cavity, sending the amplified pulse back to the Faraday insulator. Here it is separated by the incoming radiation with a polarizer. The pulse is compressed down to less than 200 fs after multiple reflection on a compressor grid. The radiation is released with a repetition rate of 72 kHz and each pulse carries about 4 μJ of energy at 800 nm wavelength.

2.2 Pump probe techniques

The pump-probe method allows to access the dynamics induced in a system after an external excitation. If the investigated dynamics develops on a time scale of nanosecond (1ns=$10^{-9}s$), then the excitation and the probe mechanism requires events faster then this. So far the fastest events available are laser pulses. Commercially available laser systems can generate pulses shorter than hundred femtoseconds (1fs=$10^{-15}s$). In the present work the excitation of the system is due to a high intensity laser pulse, called pump. The pump pulse supplies the energy necessary to impulsively heat the system. As shown in the three temperature model the energy is first absorbed by the electrons and then delivered to the other subsystems like lattice vibrations or magnetic modes. The probe depends on the physical properties investigated. The different probes will be discussed in the corresponding subsections.

The basic concepts of the pump probe technique is that, after the system has been excited by an external laser pulse, the probe measures the properties of the system at different time delays. One single measurement is composed by two steps: 1) the pump excites the system at a certain time t_0, 2) after a time delay, the probe interacts with the excited system. A pump-probe experiment consists of a series of measurements where the relative delay between pump and probe changes. It is required that the system relaxes back to the unperturbed state after the excitation and before the following measurement. The time distance between two excitations is dictated by the RR of the laser, for example at 72 kHz the time distance is 13.8 μs which is much longer than the relaxation time of the investigated dynamics (on the order of a few ns). Furthermore the dynamics of the system has to be repetitive, meaning the system has to respond to the external stimulus always with the same dynamics. This guarantees the reproducibility of the measurements and hence of the experiments.

There are two fundamental characteristics of this technique that have to be kept in mind. First the time duration of the probe determines the time in which the radiation interacts with the system, hence the physical properties investigated are time averaged over this time. This means that the pulse duration of the probe determines the time reso-

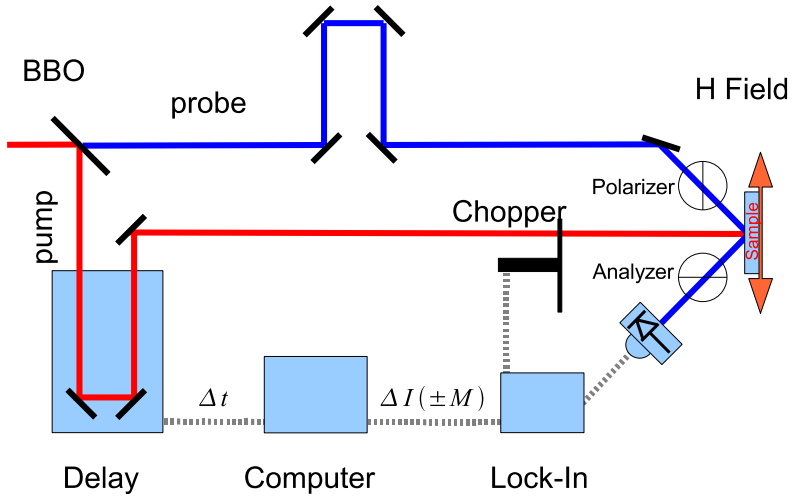

Figure 2.2: Setup scheme for a Time Resolved MOKE experiments. Part of the fundamental laser radiation is frequency doubled by a BBO crystal and separated in two optical branches. The 800 nm radiation (pump) is mechanically chopped at a frequency close to 2 kHz which allows the use of a lock-in amplifier. The 400 nm radiation (probe) passes through a polarizer to ensure it is linearly polarized before hitting the sample.

lution of the experiment. Second the time at which the physical properties are measured is determined by the relative time delay between pump and probe. When the two pulses hit the system at the same time, this identifies the temporal overlap and is denoted as t_0, which marks the beginning of the excitation. The time delays are evaluated with respect to t_0. In Fig.2.2 the schematic view of a time resolved MOKE setup is reported. In this case the pump and probe are laser radiations of different frequencies. A delay in the pump with respect to the probe is induced by a motorized linear stage which changes the length of the optical path of the pump.

A single event is hardly detectable and the Signal-to-Noise ratio (SNR) related to a single measurement is usually very low. But the stroboscopic nature of the experiments allows to apply different strategies to enhance the SNR. One consists in a modulation of the pump at a frequency different from the RR of the laser, allowing to use a lock-in amplifier. Another consist in averaging over a long time scale in which the contributions of many events are summed up.

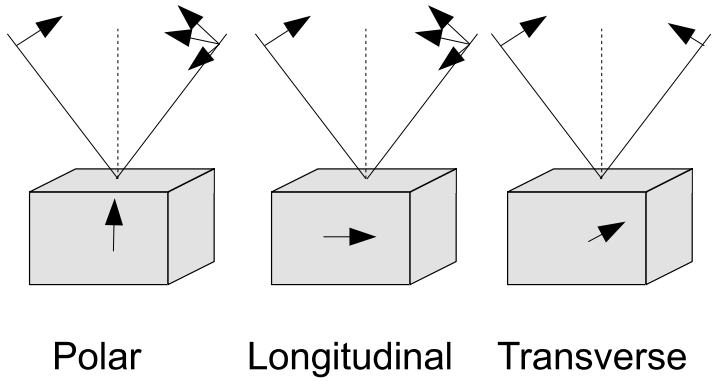

Figure 2.3: Possible MOKE configurations. a) Polar configuration: the magnetization lies in the incident plane and is perpendicular to the surface of the sample; b) Longitudinal configuration: as before but the magnetization is parallel to the surface plane of the sample. c) Transverse configuration: the magnetization is perpendicular to the incidence plane. In a) and b) the polarization plane of the reflected light is rotated, while in c). the polarization plane is conserved but the intensity of the radiation is changed. For more details see [6].

2.3 Time resolved Magneto Optical Effect

The magneto-optic effect can be described macroscopically by the change of the dielectric tensor of a material due to the magnetic order. The appearance of off diagonal elements which depend on the magnetization are responsible for the change of the polarization state of the incident light in transmission (Faraday effect) or in reflection (Kerr effect). Since the work of John Kerr in 1877 [4], the interaction of magnetic moments and light is one of the preferred tools to investigate magnetism in condensed matter. The magneto-optical Kerr effect consists of the rotation of the polarization plane of the light reflected from a ferromagnetic material [5]. One can distinguish between three different configurations corresponding to different orientations of the magnetization and the incidence plane of light [6]. The optical response of a ferromagnetic material is described by the dielectric tensor, which in the case of an isotropic material with a uniform magnetization $\mathbf{M}$, can be written as following:

$$\epsilon = \begin{pmatrix} \epsilon_{xx} & \epsilon_{xy} & \epsilon_{xz} \\ -\epsilon_{yx} & \epsilon_{yy} & \epsilon_{yz} \\ -\epsilon_{zx} & -\epsilon_{zy} & \epsilon_{zz} \end{pmatrix} \tag{2.1}$$

The diagonal elements have time-reversal symmetry, hence are even in $\mathbf{M}$, and are related to the reflectivity of the material. The off diagonal elements ϵ_{ij} are related to the $i \times j$ component of the magnetization, and they are antisymmetric with respect to time-reversal, hence they change sign upon magnetization reversal [7]. It can be shown that when one of the configurations described in Fig.2.3 is chosen, the total rotation in the polarization plane, θ_T can be written as follows:

$$\tilde{\theta}_T = G_0 + \sum_i K_i M_i = \tilde{\theta}_S + \tilde{\theta}_A \tag{2.2}$$

where G_0 and K_i are effective Fresnel coefficients, and are collecting the dependance of the rotation on sample material and thickness, as well as on wavelength and angle of incidence. The last part of Eq.2.2 implies that the Kerr rotation has two contributions, the first, $\tilde{\theta_S}$, symmetric upon sign change of the magnetization $\mathbf{M}$ and the second $\tilde{\theta_A}$ antisymmetric. Doing experiments where the Kerr rotation is measured in opposite direction of the magnetization allows to detect the antisymmetric part $\tilde{\theta_A}$, even if $\tilde{\theta_S}$ is non zero: in fact $\tilde{\theta_T}(\mathbf{M}) - \tilde{\theta_T}(-\mathbf{M}) = 2\tilde{\theta_A}$. The time evolution of the Kerr rotation is tightly related to the time evolution of the magnetization. As proposed by Kampfrath and coworkers in [8], the total rotation of the incidence plane can be written as follow

$$\tilde{\theta}_T(t) = \Phi[\mathbf{M}(t), t] = G_0(t) + \sum_i K_i(t) M_i(t) \tag{2.3}$$

where $\Phi[\mathbf{M}(t), t]$ is a functional of $\mathbf{M}$. Experimentally it is possible to set a configuration in which the rotation is due to only one component of the magnetization. Assuming that the orientation of the magnetization remains constant, the induced rotation is dominated by only one component of $\mathbf{M}$, and that a weak perturbation approach is applicable, the change in time of the Kerr rotation can be written as follows:

$$\Delta\tilde{\theta}(t) = \Delta G(t) + M_0 \Delta F(t) + F_0 \Delta M(t) \tag{2.4}$$

In many cases it is legitimate to assume that the Fresnel coefficients do not change with time, allowing the further simplification:

$$\Delta\tilde{\theta}(t) = F_0 \Delta M(t) \tag{2.5}$$

this last equation shows how the magnetization and the induced Kerr rotation are related. In fact from Eq.2.4 and Eq.2.5 remembering the approximations made so far we can write:

$$\frac{\Delta\tilde{\theta}(t)}{\tilde{\theta}} = \frac{\Delta M(t)}{M} \tag{2.6}$$

This equation plays a key role in the experimental investigation of magnetization dynamics by optical probes, because it relates the time evolution of the measured quantity $\Delta\theta$ with the time evolution of the magnetization of the system.

TR-MOKE in the crossed polarizer configuration

To measure the rotation of the polarization plane we adopted a crossed polarizer configuration, see Fig.2.2. In this configuration two polarizers are used. The first is placed in front of the sample and is called polarizer (P), the second is placed after the sample in front of the photodetector and is called analyzer (A). Assuming that in (P) the amplitude of the electric field is normalized and omitting the oscillatory term $e^{i(\mathbf{k}\cdot\mathbf{r}-\omega t)}$, the polarization state of the incoming radiation can be described in terms of the Jones vectors as follows:

$$\mathbf{E} = E_s\mathbf{e_s} + E_p\mathbf{e_p} = \begin{pmatrix} E_s \\ E_p \end{pmatrix} = \begin{pmatrix} \sin\alpha_p \\ \cos\alpha_p \end{pmatrix}, \text{ at P} \tag{2.7}$$

where α_P denotes the orientation of the axis of the polarizer and hence the direction of the incidence plane before the sample.

It can be shown that the reflection from a magnetic system is governed by the following Jones matrix:

$$S = \begin{pmatrix} r_s & \tilde{\theta} \\ -\tilde{\theta} & r_p \end{pmatrix} \tag{2.8}$$

where r_s and r_p are the complex reflection coefficients acting on the s- and p-polarized component of the incident radiation, while $\tilde{\theta} = \theta + i\epsilon$ is the antisymmetric part of the Kerr rotation introduced in Eq.2.2. The Jones matrix has this form because the induced Kerr rotation is small ($|\tilde{\theta}| \simeq 10^-3$ rad). The crossed configuration consists in setting the analyzer (A) angle α_A almost perpendicular to the polarizer angle α_P. Setting $\alpha_P = 90$ and $\alpha_A \simeq 0$ the intensity after the analyzer can be evaluated as follows:

$$I = |\begin{pmatrix} sin\alpha_A & cos\alpha_A \end{pmatrix}\begin{pmatrix} r_s & \tilde{\theta} \\ -\tilde{\theta} & r_p \end{pmatrix}\begin{pmatrix} sin\alpha_P \\ cos\alpha_P \end{pmatrix}|^2 = R(\alpha_A^2 + 2\alpha_A\theta + \theta^2 + \epsilon^2) \tag{2.9}$$

where $R = |r_s|^2$. Keeping only the terms up to θ, the static intensity after the analyzer can be written as follow:

$$I = R(\alpha_A^2 + 2\alpha_A\theta) \tag{2.10}$$

In the previous expression, the first term ($\mathrm{R}\alpha_A^2$) has no dependence on M, while the second one does, and in particular it is an odd function of M. To keep the non-magnetic background small α_A has to be kept small, but not too small in order to keep the second order term of $\tilde{\theta}$ in Eq.2.9 negligible [7]. The induced change in the intensity can be derived by Eq.2.10 and the following relation holds:

$$\Delta I(t) = \alpha_A^2\Delta R(t) + 2R_0\alpha_A\Delta\theta(t) \tag{2.11}$$

The symmetry with respect to **M** if preserved, allowing to separate the two contributions by recording the change in intensity for opposite orientations of the magnetization. In fact the induced change in the reflectivity is obtained by taking the sum of the two recorded intensities, while the difference gives the change in the Kerr rotation:

$$\begin{cases} I(t,\mathbf{M}) - I(t,-\mathbf{M}) & = 4R_0\alpha_A\Delta\theta(t) \\ I(t,\mathbf{M}) + I(t,-\mathbf{M}) & = 2\alpha_A^2\theta\Delta R(t) \end{cases} \tag{2.12}$$

This shows how the presented detection scheme allows to measure both the optical and the magnetic dynamics induced in the system by performing the experiment for opposite orientation of the magnetization.

2.4 Time resolved X-Ray diffraction

To investigate the structure of a physical system an X-ray diffraction technique is required. The explanation of this requirement has been given by W.L.Bragg and W. H.Bragg (Nobel Laureates in 1915). The incident radiation is specularly reflected by the atomic planes present in the lattice of crystal. A diffraction spot will be found when the reflected radiation from the different atoms in the atomic plane has a constructive interference with the radiation reflected by the neighboring planes. This is true if the distance between the planes, d is a multiple of the wavelength of the incident light, λ. This condition is summarized in Bragg's law

$$2d\sin\phi = n\lambda \tag{2.13}$$

where ϕ is the incidence angle of the light with respect to the surface, and n is an integer denoting the diffraction order. The distance between the atomic planes d is of the same order as the interatomic distance, for this reason one needs X-ray radiation to see the diffraction pattern. The Bragg law does not contain any reference to the basis structure or to the position of the atoms in the lattice. However this information is important to estimate the intensity of the diffraction peak of the different orders [9].

Until the development of the Free Electron Lasers (FEL) [10], the most brilliant x-ray source was the synchrotron. It is a storage ring where charged particles (electrons or positrons) are accelerated up to a speed close to the speed of light and kept in orbital motion. The particles are accelerated in bending magnets placed on the circuit which keep them on the circular orbit and in insertion devices such as wigglers or undulators where a set of alternating magnets make the trajectory of the particles sinusoidal. In this devices the emission of x-ray takes place. In a synchrotron ring the distribution of the electrons is not uniform, but they rather travel in bunches. The non uniformity of the electron distribution will also imply that the X-ray radiation generated is non uniform. The electron bunch dimension will determine the x-ray pulse dimension which for the third generation synchrotron is known to be hundred of picoseconds. By modifying the

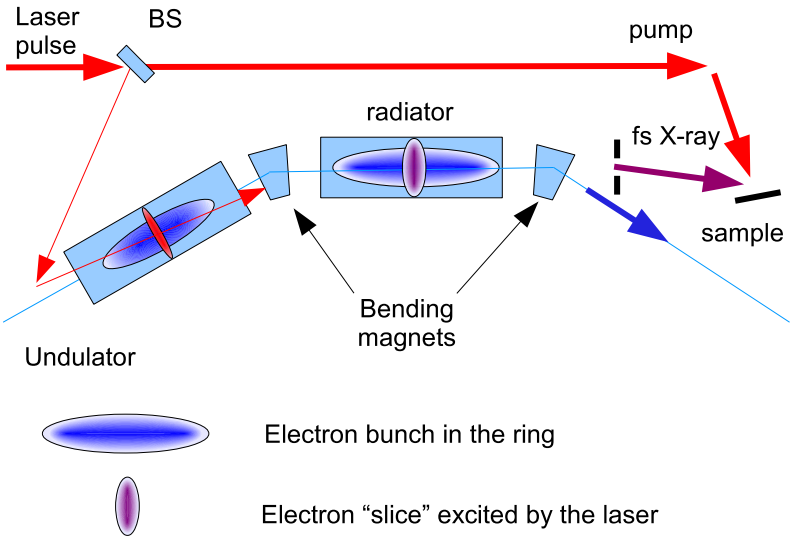

Figure 2.4: Scheme of the femtoslicing setup implemented at the FEMTO beam line at SLS. The generation of a fs X-ray pulse is a two step process. The first step consist in the interception with the laser pulse of the electron bunch in an undulator where a fraction of the electrons is excited. The electron bunch along with the excited electron travel trough a second undulator (radiator) where the X-rays are generated. The X-rays from the excited electrons are separated from the main beam with an aperture.

filling factor of the storage ring one can adjust the momentum compaction factor α (bunch length $\propto \sqrt{\alpha}$) reducing the pulse length to a few picoseconds. The price paid with this operation is to induce instability in the ring electron flux with a consequent lower X-ray quality. In the middle of the 90's however an alternative technique to produce shorter X-ray pulses has been developed, the so called femtoslicing.

Femtoslicing is a synchrotron based experimental technique which allows to generate X-ray pulses by the interaction between a high intensity laser field and the electron bunch stored in the ring [11]. In 1996 Zholents and Zolotover in 1996 proposed the concepts for an ultrashort X-ray radiation which has then been realized for the first time by Schoenlein in the year 2000 at the Advanced Light Source (ALS). The process can be divided into three steps: 1) the interaction of the electron bunch with a highly intense 100-fs laser pulse in a wiggler (modulator); 2) the separation of the energy modulated electrons; 3) the radiation of 100-fs X-ray pulse by the 100-fs electron slice in an undulator (radiator),

as shown in Fig.2.4. The so produced X-ray pulse will then be separated from the core X-ray beam by the introduction of apertures in the optical path. The strong electric field present in a laser pulse can modulate the energy of the electron in the bunch if the laser wavelength λ_l is comparable to the fundamental wavelength of the undulator $\lambda_1 = \lambda_u(1+K^2/2)/2\gamma^2$ where λ_u is the wavelength of the undulator, γ is the Lorentz factor and $K = eB_0\lambda_u/2\pi m_0 c = 93.4B_0\lambda_u$. The experiments reported in this work have been performed at the FEMTO beamline at the Swiss Light Source (SLS). This beam line uses a wiggler of 17 periods, $B_0 = 1.98[T]$, $\lambda_u = 13.8[cm]$ and $\gamma = 4720$. To excite the electron bunch a conventional Ti:sapphire Kerr-lens mode-locked oscillator is used. It is phase-locked to the fifth submultiple of the synchrotron rf-master oscillator (500 MHz) with an estimated jitter of less than 1 picosecond [12]. This beam is split into two parallel optical paths one to excite the electrons in the storage ring, generating the X-ray probe pulse, and the other sent directly to the sample to optically excite the system. This specifics give $\lambda_1 = 1000[nm]$ that can be tuned to match the laser wavelength $\lambda_l = 805[nm]$. By using a 2 mJ laser pulse the energy modulation achieved is $\Delta E/E = 0.5\ 10^{-3}$ which is almost 6 times the energy spread of the electron bunch. After a chicane the energy modulation translates to a spatial separation of 2 mm in the undulator where the X-rays are produced. The introduction of a mechanical slit in the optical path of the X-ray beam allows to separate the sliced x-ray pulse from the main beam. The X-ray pulse produced at FEMTO has a duration of 140 fs, which determines the temporal resolution of the experiment.

2.5 Ferromagnetic Resonance

Ferromagnetic resonance (FMR) is a technique that addresses the magnetization dynamics in a magnetic system by means of energy absorption of electromagnetic waves in the microwave frequency range [13]. The conventional FMR experimental setup in sketched in Fig.2.5. A gunn diode generates a sinusoidal wave of fixed frequency f_{RF} which propagates in a waveguide. The wave guide is shorted and the sample is placed in the proximity of the short. This end of the wave guide is placed in between the yoke of an electromagnet that generates the external magnetic field H_{DC}. The rf-field excites the magnetization in the sample while the external DC field is swept across the resonance condition. After the interaction of the rf-wave with the sample the reflected wave energy loss is measured by a microwave diode detector as a function of the external field. To enhance the SNR, the DC field is modulated at a reference frequency ω_{ref} in order to allow a lock-in amplification.

The relative orientation of the external field H_{DC} and the magnetization of the system determines the geometry of the FMR measurement and the resonance condition. We talk of in-plane FMR (IP-FMR) when the magnetization and the external field lie in the

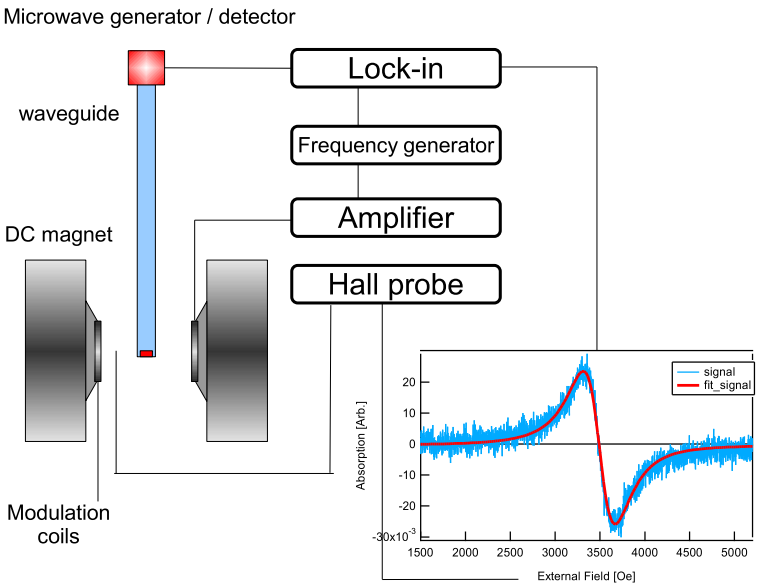

Figure 2.5: Conventional FMR setup. The sample is placed at the short of a waveguide where the electromagnetic field generated by a gunn diode is reflected back to the detector. The waveguide end is located in the 3 cm wide gap of an electromagnet generating an external DC field up to 2.1 T. A couple of small coils is used to modulate the DC field at a reference frequency controlled by a frequency generator and fed into the lock-in amplifier. The external field is swept and the radio frequency losses are measured. A typical FMR line-shape is reported in the inset.

magnetic film plane. In this case the resonance condition is given by [14]

$$\left(\frac{\omega}{\gamma}\right)^2 = \mu_0 \mathfrak{B}_{eff} \mathfrak{H}_{eff}\Big|_{H_{FMR}} \tag{2.14}$$

where γ is the gyromagnetic ratio, $\omega = 2\pi f$, $\mathfrak{B}_{eff}$ is the effective magnetic induction, and $\mathfrak{H}_{eff}$ is the effective magnetic field. The samples used in this work show an in-plane magnetic anisotropy that depends on the substrate (see previous chapter). In this case the resonance condition is written as $\mathfrak{B}_{eff} = \mu_0(H_{DC} + M + H_{ani})$ and $\mathfrak{H}_{eff} = H_{DC}$. In case of a fully saturated sample the relation of the rf-driving field $\mathbf{h}^{rf}$ and the rf-component of the magnetization $\mathbf{m}^{rf}$ is given by the imaginary part of the rf-susceptibility χ^{rf}, so that

$\chi^{rf} = \frac{m^{rf}}{h^{rf}}$. The following relation holds [15]

$$Im[\chi] = M_s \frac{\mathfrak{B}_{eff}}{\mathfrak{B}_{eff} + \mu_0 \mathfrak{B}_{eff}}\bigg|_{H_{FMR}} \frac{\Delta H}{\Delta H^2 + (H_{DC} - H_{FMR})} \tag{2.15}$$

$$\Delta H = \alpha \frac{\omega}{\gamma \mu_0} \tag{2.16}$$

where ΔH is the half width at half maximum (HWHM) linewidth . The imaginary part of the rf-susceptibility has a Lorentzian shape. This formula is applicable in the case of saturated samples. The validity of this assumption across the phase transition in FeRh will be discussed in chapter 5. Since the DC field is modulated and the signal is amplified by a lock-in, the actual recorded trace is proportional to the derivative with respect to the field of the Eq.2.15.

In the perpendicular configuration the magnetization and the field H_{DC} are both perpendicular to the sample plane. In this case the resonance condition is given by [15]

$$\left(\frac{\omega}{\gamma}\right)^2 = \mu_0 (H_{FMR} - M_s + H_{ani}) \tag{2.17}$$

Usually, one extracts from the measured FMR spectrum the position of the peak, e.g. the resonance field (see Eq.2.14 and Eq.2.17) and the linewidth, (Eq.2.16). From the angle and frequency dependence of the resonance field one can extract information on the g-factor and on the internal fields. From the angle and frequency dependence of the linewidth one can extract information on the intrinsic and extrinsic damping and on the underlying physical mechanisms. In the present work particular attention has been devoted to the area of the resonance and to its dependence on temperature. The area of the absorption peak is, as customary in absorption spectroscopy, directly proportional to the number of resonators involved in the process [16]. In the case of FeRh the number of spins in the ferromagnetic phase, the only ones contributing to FMR, varies with temperature. Hence the area under the resonance peak will change proportionally.

Amplitude, resonance field and linewidth are extracted from the experimental data via a fitting procedure using an asymmetrical Lorentzian function. The asymmetry in the FMR spectrum has to be taken into account, because the contact of the sample with the waveguide can mix real and imaginary part of the susceptibility $\chi = \chi' \sin(\epsilon) + i\chi'' \cos(\epsilon)$. The asymmetrical absorption function f_A is given by [15]

$$f_A \propto \chi' \sin(\epsilon) + \chi'' \cos(\epsilon) \propto \frac{\Delta H \cos(\epsilon) + (H + H_{FMR}) \sin(\epsilon)}{\Delta H^2 - (H + H_{FMR})^2} \tag{2.18}$$

The function used to fit the data is the derivative with respect to the field of Eq.2.18, namely

$$\frac{df_A}{dH} = -\frac{2(H - H_{FMR})\Delta H \cos(\epsilon)}{[\Delta H^2 - (H + H_{FMR})^2]^2} - \frac{(\Delta H^2 - (H + H_{FMR})^2)\sin(\epsilon)}{[\Delta H^2 - (H + H_{FMR})^2]^2} \tag{2.19}$$

Once the fit has been performed and the parameters H_{FMR}, ΔH and ϵ are known, the area under the absorption peak is obtained by numerical integration

$$F = \int_0^\infty f_A(H) dH \tag{2.20}$$

The value of the integral is proportional to the number of the resonator present in the sample. A detailed discussion of its meaning will be given in Chapter 4.

References

[1] D.E. Spencer, P.N. Kean, and W. Sibbett. 60-fs pulse generation from a self-mode-locked Ti:sapphire laser. *Opt. Lett.*, 16:42, 1991.

[2] Coherent Inc. *The Mira seed laser operator's manual.* 2005.

[3] J. Squier, F. Salin, G. A. Mourou, and D. Harter. 100-fs pulse generation and amplification in Ti:al2o3. *Opt. Lett.*, 16:324, 1991.

[4] J. Kerr. On the rotation of the plane of polarization by reflection from the pole of a magnet. *Phil. Mag*, 3:321, 1877.

[5] P.N. Argyres. Theory of Faraday and Kerr effect in ferromagnetics. *Phys. Rev*, 97:334, 1955.

[6] S. Blundell. *Magnetism in condensed matter.* Oxford University Press, 2001.

[7] B. Hillebrands and K. Ounadjela, editors. *Spin dynamics in confined magnetic structures II*, volume 2. Springer Verlag, 2003.

[8] T. Kampfarth, G. Ulbrich, F. Leuenberger, M. Muenzenberg, B. Sass, and W. Felsch. Ultrafast magneto-optical response of iron thin films. *Phys. Rev. B*, 65:104429, 2002.

[9] C. Kittel, editor. *Introduction to Solid state physics.* John Wiley and Sons, seventh edition, 1996.

[10] D. A. G. Deacon, L. R. Elias, J. M. J. Madey, G J. Ramian, H. A. Schwettman, and T.I. Smith. First operation of a free electron laser. *Phys. Rev. Lett.*, 38:892, 1977.

[11] A.A. Zholents and M. S. Zolotorev. Femtosecond X-ray pulses of synchrotron radiation. *Phys. Rev. Lett.*, 76:912, 1996.

[12] P. Beaud, S.L. Johnson, A. Streun, R. Abela, D Abramsohn, D Grolimund, F. Krasniqi, T. Schmidt, V. Schlott, and G Ingold. Spatiotemporal stability of a femtosecond hard-x-ray undulator source studied by control of coherent optical phonons. *Phys. Rev. Lett.*, 99:174801, 2007.

[13] B. Heinrich. Radio frequency techniques-ferromagnetic resonance in ultrathin film structures. In B. Heinrich and J.A.C. Bland, editors, *Ultrathin magnetic structure II.* Springer Velag, Berlin, 1994.

[14] M. Binder. *Magnetization dynamics of Rare-Earth doped magnetic films.* PhD thesis, University of Regensburg, Regensburg, Germany, 2006.

[15] G. Woltersdorf. *Spin-pumping and two-magnon scattering in magnetic multilayers.* PhD thesis, Simon Fraser University, Burnaby, Canada, 2004.

[16] R.S. Alger and I. Hayashi. *Electron paramagnetic resonance: techniques and applications.* Interscience Publishers, 1968.

Chapter 3

Samples

The FeRh system has been studied for the first time by Fallot and Horact in 1939. They reported for the first time a magnetic phase transition at a temperature higher then room temperature (RT) in non stoichiometric compounds [1]. The samples considered in the present work are stoichiometric compounds of FeRh meaning that the same amount of Fe and Rh ions is present in the system. FeRh compounds have a CsCl structure where the Fe ions sit at the corners of the cubic cell while the Rh ions are placed at the center of the cube. The samples are said to be homogeneous if the aforementioned proportion holds and the distribution of the ions is the same in all the cubic cells. The lattice constant is $a_0 = 2.986 \pm 0.004\ \mathring{A}$ [2].

The samples studied in this work are thin films of FeRh epitaxially grown on different substrates. To prevent oxidation some of the samples have been capped with thin layers of Pt or Ta. The films and the capping layers have been deposited by co-magnetron sputtering from elemental targets. The list of the samples is summarized in Tab.3.1. NC0 sample has been made at the MINT research center in the University of Alabama in the group of Prof. Dr. T. Suzuki. NC1, Pt1 and Pt2 have been made at the University of California, San Diego by Dr. V. Uhlir in the group of Prof. Dr. E. E. Fullerton, and Ta1,

Name	Thickness d_{FeRh}	Capping	substrate
NC0	30 nm	no	MgO
NC1	30 nm	no	MgO
NC2	50 nm	no	MgO
NC3	50 nm	no	Al_2O_3
Pt1	30 nm	Pt (2nm)	MgO
Pt2	30 nm	Pt (2nm)	MgO
Ta1	50 nm	Ta (2nm)	MgO
Ta2	50 nm	Ta (2nm)	Al_2O_3

Table 3.1: List of the sample considered in this work, and characteristics of the films

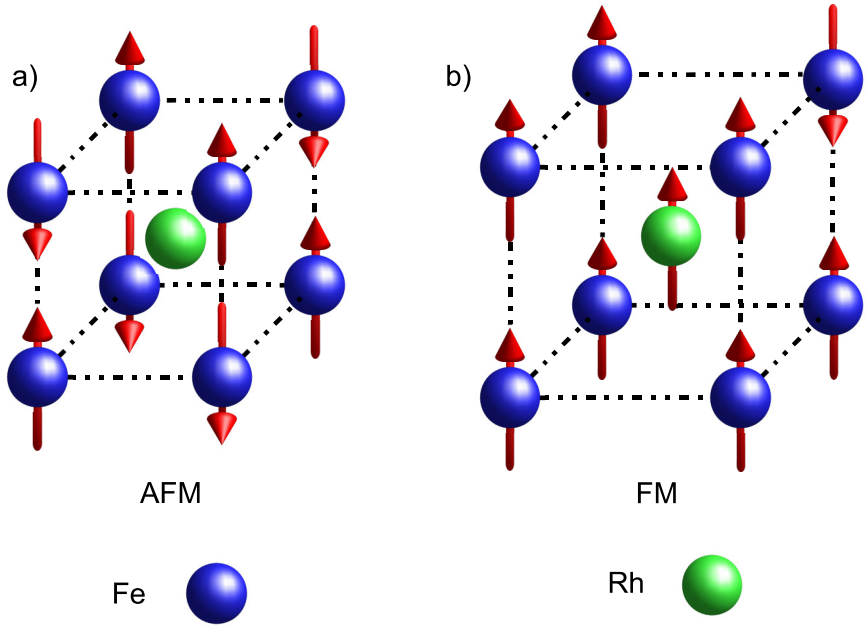

Figure 3.1: On the left side the FeRh antiferromagnetic order below the critical temperature is shown. The Fe ions carry a magnetic moment of 3.3 μ each while the Rh ions have no net magnetic moment. In the ferromagnetically ordered phase the Fe ions carry a magnetic moment of 3.1 μ and the Rh ions a magnetic moment of 0.9 μ_b. The unit cell is expanded in the ferromagnetic phase and the volume is increased by 1 percent.

Ta2, NC2 and NC3 have been made in the same group by S. Moyerman.

FeRh shows a first order phase transition driven by temperature [3]. At room temperature (RT), the system is in the Anti-Ferromagnetic Phase (AFP) where the Fe ions carry a magnetic moment of 3.3 μ and are antiparallelly aligned. In this phase the Rh ions show no net magnetic moment, see Fig.3.1 a). When the temperature is raised above a certain critical temperature T_{tr}, the system enters in a Ferromagnetic phase (FP). In this phase the Fe magnetic moments change to 3.1 μ and align along the same direction. At the same time the Rh ions gain a net magnetic moment of 0.9 μ pointing along the same direction as the Fe moments. The transition is accompanied by an expansion of the volume of the cubic cell of about 1%, see Fig. 3.1 b) [4, 5]. In case of bulk samples the expansion is isotropic, while for thin films the expansion is constrained by the interaction

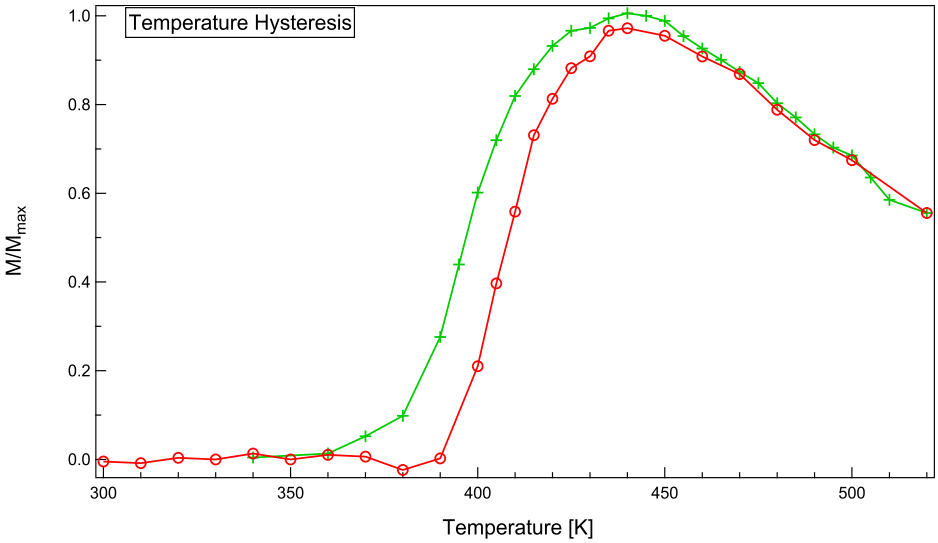

Figure 3.2: Magnetization vs temperature measured with static MOKE on NC0 sample. For each temperature a hysteresis loop has been measured with a maximum external field of 1 kOe and the value of the magnetization has been extracted. The two transition temperatures are $T_{AF\to F} = 402.5$ K and $T_{F\to AF} = 397.5$ K. The hysteresis width is 10 K indicating a very homogeneous sample (see text).

with the substrate, and the volume tends to expand in the direction perpendicular to the film plane. The samples considered in the present work are grown either on MgO(100) or on $Al_2O_3(0001)$ (sapphire). Due to the lattice constant mismatch in the former case the base area (interface between film and substrate) is slightly expanded, while in the latter case slightly compressed [6].

The first step to study the phase transition is to determine the critical temperature T_{cr}. To do this one has to measure the dependence of the magnetization or of the magnetic moment with temperature. The result of this measurement is called the M-T curve [7], where the temperature is raised up to a value greater than T_{cr} (heating branch) and then lowered back to the initial temperature, usually RT (cooling branch). A typical M-T curve for FeRh is reported in Fig.3.2. The measurement is made on sample NC0 and at each temperature step a full hysteresis loop has been measured by using the Magneto-Optical Kerr Effect (MOKE, see Chapter 3 for description and references) with a maximum external field of 1 kOe. The reported values are the saturation magnetization at the maximum field applied, $M_S(H = 1\text{kOe})$. The curve shows a temperature hysteresis, in fact the cool-

ing branch results to be shifted toward lower temperatures with respect to the heating branch. This sort of magnetic inertia [7] is always present in homogeneous FeRh films. Three information can extracted from the M-T curves: the transition temperature from AFP to FP ($T_{AFP\rightarrow FP}$), the transition temperature from FP back to AFP ($T_{FP\rightarrow AFP}$), and the hysteresis width $\Delta T = T_{AFP\rightarrow FP} - T_{FP\rightarrow AFP}$. $T_{AFP\rightarrow FP}$ is defined as the temperature at which the magnetization reaches the half of the maximum value in the heating branch, and accordingly $T_{FP\rightarrow AFP}$ on the cooling branch. The value of the transition temperatures and of the hysteresis width depends critically on the composition and on the homogeneity of the sample. For a homogeneous and stoichiometric system ΔT ranges from 10 to 20 K and the full transition develops in a temperature range of about 20 to 30 K. Non stoichiometric or inhomogeneous samples show a broad hysteresis width (greater than 20 K) and the transition is smeared over a large temperature range (up to 80 K resulting in samples showing a net magnetization even below RT). The M-T curves of all the samples considered in this work are reported in Fig.3.3 and Fig.3.4, while the transition temperatures values are reported in Tab.3.2. The data reported in Fig.3.3 have been measured via SQUID magnetometry with an external applied field of 3 Tesla. It has been shown by Maat and coworkers in [8] that a strong external field can linearly shift both $T_{AFP\rightarrow FP}$ and $T_{FP\rightarrow AFP}$ toward lower values, giving a linear shift constant $a = -8\,K/T$. The values of the temperatures reported in Tab.3.2 have been rescaled accordingly.

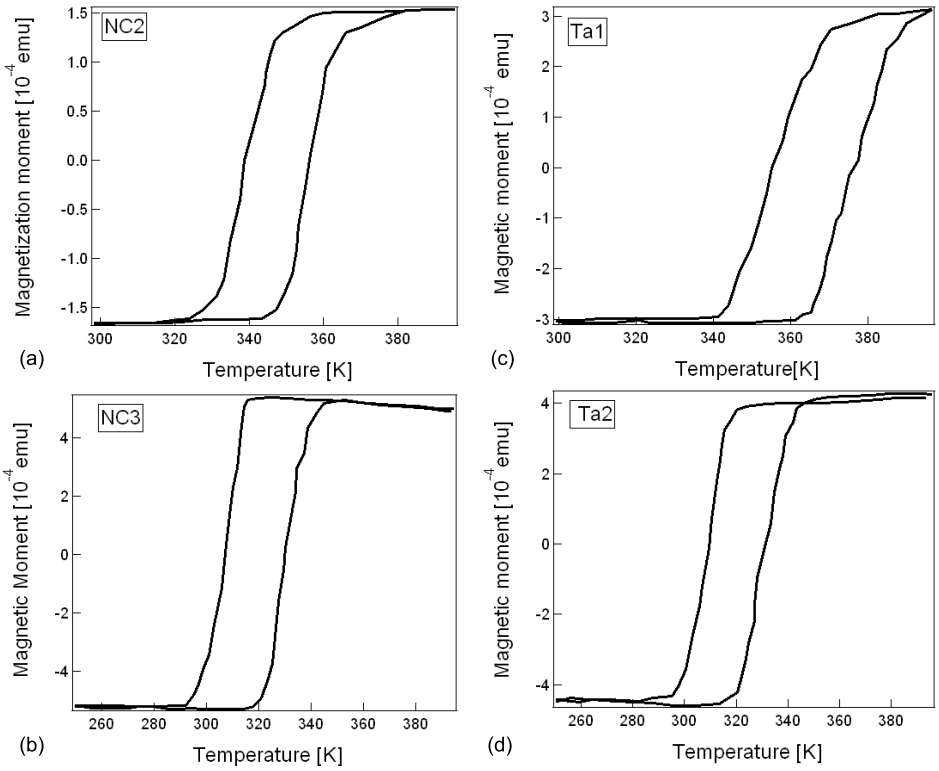

Figure 3.3: Magnetization vs temperature measured with SQUID for the samples NC2, NC3, Ta1,Ta2. The measurements have been made using a 3 Tesla external field inducing a shift of -27 °K. The curves have been manually centered around zero. The measurements have been made at UCSD by S. Moyerman.

The reported quantities show that the overall quality of the samples is good. The differences in the values of the transition temperatures can be ascribed to the interaction of the films with the different substrates and capping layers. The sample which most fulfills the requests of homogeneity and stoichiometry is NC0, where the hysteresis width is minimal. On the other side the sample grown on Al_2O_3 (NC3 and Ta2) exhibits the broadest width pointing to a bigger degree of inhomogeneity. For this reason most of the experiments reported in this work have been performed on samples grown on MgO.

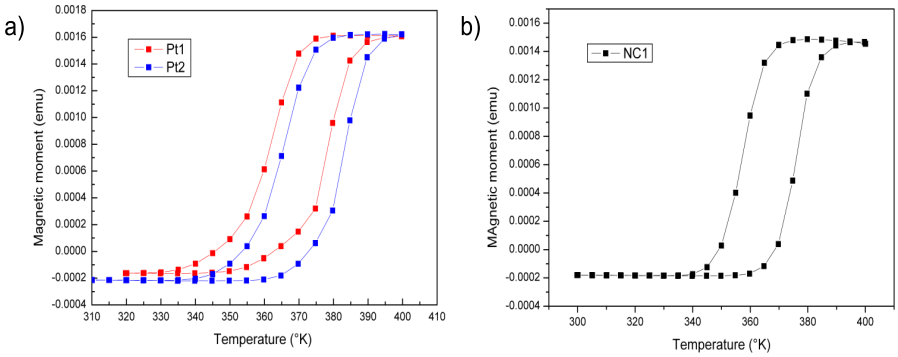

Figure 3.4: Magnetization vs temperature measured with Vibrating Sample Magnetometry (VSM) for the samples Pt1, Pt2, and NC1. The negative moment at room temperature is the diamagnetic contribution from the substrate. The measurements have been made at UCSD by Dr. V. Uhlir.

Name	$T_{AFM \to FM}$ [K]	$T_{FM \to AFM}$ [K]	ΔT [K]	Substrate
NC0	405	395	10	MgO
NC1	376.7	357.9	18.8	MgO
NC2	383.3	366.7	17.6	MgO
NC3	327	349.9	22.9	Al_2O_3
Pt1	378.5	361.7	16.8	MgO
Pt2	383.3	365.7	17.6	MgO
Ta1	403.3	382.4	20.9	MgO
Ta2	336.7	357.9	21.7	Al_2O_3

Table 3.2: List of the transition temperatures and of the hysteresis width of samples considered in this work.

References

[1] M. Fallot and R. Hocart. Les alliages du fer avec les metaux de la famille du platine. *Rev. Sci.*, 77:498, 1939.

[2] E. Kren, L. Pal, and P. Szabo. Neutron diffractionh investigation of the antiferromagnetic-ferromagnetic transformation in the FeRh alloy. *Phys. Lett.*, 9(4):297, 1964.

[3] J. S. Kouvel and C. C. Hartelius. Anomalous magnetic moments and transformations in the ordered alloy FeRh. *J. Appl. Phys.*, 33(3):1343, 1962.

[4] V. L. Moruzzi and P. M. Marcus. Antiferromagnetic-ferromagnetic transition in FeRh. *Phys. Rev. B*, 46(5):2864, 1992.

[5] J. B. McKinnon, D. Melville, and E. W. Lee. The antiferromagnetic-ferromagnetic transition in iron-rhodium alloys. *J. Phys. C: Solid State Phys.*, 3:S46, 1970.

[6] S. O. Mariager. private communication, 2011.

[7] B. Bergman, G. Ju, J. Hohlfeld, R. J. M. van de Veerdonk, J.-Y. Kim, X. Wu, D. Weller, and B. Koopmans. Identifying growth mechanism for laser-induced magnetization in FeRh. *Phys. Rev. B*, 73:060407R, 2006.

[8] S. Maat, J.-U. Thiele, and E. E. Fullerton. Temperature and field hysteresis of the antiferromagnetic-to-ferromagnetic phase transition in epitaxial FeRh films. *Phys. Rev. B*, 72:214432, 2005.

Chapter 4

Ferromagnetic Resonance measurements

The scope of this chapter is to give a first characterization of the magnetic phase transition of FeRh, and to present the results of the investigated magnetization dynamics with the ferromagnetic resonance (FMR) technique. The angular dependence of the position and of the linewidth allow to determine the anisotropy constants of system. Further more the role of the two-magnon scattering in the damping process has been demonstrated. The minimal linewidth measured for the FeRh alloy is $\alpha = 0.0013 \pm 0.0008$.

4.1 Introduction

The first order character of the phase transition implies the coexistence of two phases which differ from one another in the magnetic order. Different orders will interact differently with an external applied magnetic field and hence, in an FMR experimental setup, resonance conditions of the ferromagnetic phase will be different from that of the anti-ferromagnetic phase. It has been demonstrated by Kittel that indeed the resonance condition in a ferromagnet and in an anti-ferromagnet are different [1]. In our setup we match the resonance conditions of a material by sweeping the external static field from a 10^3 A/m up to $1.5\ 10^6$ A/m. When the resonance conditions are met an absorbtion peak is recorded. In the case of FeRh, if only the anti-ferromagnetic phase is present, namely the system is at room temperature (RT), with our setup we can not measure any resonance peak up to the maximum reachable field, meaning that the resonance condition for the AFP is met outside our field range. On the contrary, if $T > T_{FP}$ and the system is ferromagnetic, we can measure a resonance peak. This preliminary test allows us to say that within $1.5\ 10^6$ A/m the resonance peak measured is due to the FP. This was not *a priori* known, and gives us a phase sensibility in our FMR measurements. By rising the temperature, allowing the ferromagnetic phase to nucleate and expand, the change in the absorption peak of the FP is monitored. The appearance of the FP resonance

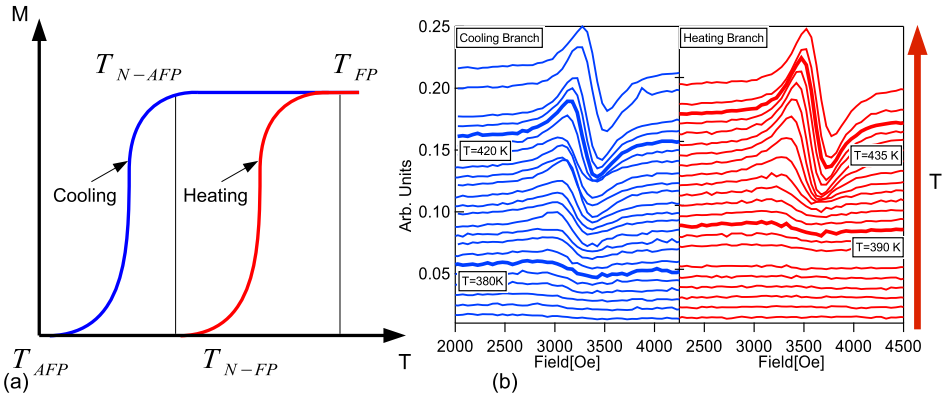

Figure 4.1: (a) Magnetization as a function of temperature. Four temperature are indicated (see text). At T_{AFP} and T_{FP} the system is completely in an anti-ferromagnetic or ferromagnetic phase, respectively. T_{N-FM} and T_{N-AFM} on the other hand, indicate where the nucleation of a different phase starts. (b) The FMR line-shapes of the NC0 sample at different temperatures for the heating and the cooling branch are reported. In the plot the four aforementioned temperatures are indicated.

peak has been recorded as a function of the temperature and the results are reported in Fig.4.1 (b). The red set of curves refers to the heating branch while the blue one to the cooling branch. It can clearly be seen that the FMR line-shape is not present at RT and rises with temperature. To give a more quantitative description of the process one needs to define a new set of temperatures. Referring to Fig.4.1 (a), T_{N-FP} is the temperature in the heating branch (red line) at which for the first time it is possible to measure an FMR line-shape. This temperature corresponds to the nucleation of ferromagnetic domains in the antiferromagnetic phase. T_{FP} is the temperature at which the intensity of the line-shape saturates, corresponding to a fully ferromagnetic phase. In the same way, in the cooling branch (blue line), one defines T_{N-AFP} as the temperature at which the AFP nucleates and the height of the resonance peak is reduced. T_{AFP} is the temperature at which the resonance peak vanishes. In Fig.4.1(b), the thicker curves indicate the four temperatures for the NC0 sample.

Along with the temperature dependence, we will also study the angular dependence of the FMR peak. In this case on can achieve knowledge of the magnetic energy landscape and determine the anisotropy constants of FeRh. This experiments will depend on the lattice symmetries present in the the system. To study the anisotropies present in the ferromagnetic phase we need the system to be ferromagnetic, hence the temperature of the sample has been set to 425 K, well above T_{FP}, to be sure that the ferromagnetic phase is fully developed.

In the following we will briefly discuss the lattice configuration together with the expected energy landscape of FeRh and its effects on the resonance conditions. FeRh films grow epitaxially with a (001) orientation and the alignment of the crystallographic directions is such that $[100]_{FeRh} \parallel [110]_{MgO}$, as characterized by X-ray diffraction, see Fig4.2 (a). The FeRh films have a cubic lattice symmetry while the outer interfaces introduce an additional out-of-plane uniaxial symmetry. In order to describe the magnetic energy density for this case it is convenient to split the anisotropy energy density functional into respective in-plane and perpendicular uniaxial and four-fold components:

$$\epsilon_{\text{ani}} = -\frac{K_1^{\parallel}}{2}\left(\alpha_x^4 + \alpha_y^4\right) - \frac{K_1^{\perp}}{2}\alpha_z^4 - K_U^{\perp}\frac{\alpha_z^2}{M_S^2} - K_U^{\parallel}\frac{(\hat{n}\cdot\mathbf{M})^2}{M_S^2} \tag{4.1}$$

where the $\alpha_x, \alpha_y, \alpha_z$ represent the direction cosines of the magnetization vector along the [100], [010], and [001] crystallographic directions, respectively (see Fig. 4.2(a)). $K_1^{\parallel}$, $K_1^{\perp}$, $K_U^{\parallel}$ and $K_U^{\perp}$ are constants describing the strength of the in-plane and perpendicular parts of the fourfold and uniaxial anisotropies. The two contributions to the anisotropy energy functional are depicted in Fig.4.2(b). The upper energy surface is the uniaxial anisotropy term. Since it shows a minimum in the XY plane this means that the magnetization is pushed to lie in the [100][010] plane. The lower energy surface is the cubic anisotropy term. The presence of four minima in the [100][010] plane indicates a four-fold in-plane anisotropy.

Neglecting the effect of damping the ferromagnetic resonance condition can be calculated when the expression of $\epsilon(\theta, \phi)$ is known using the following expression [2, 3]:

$$\omega_{\text{FMR}} = \frac{\gamma}{M\sin\theta}\left[\frac{\partial^2\epsilon_{tot}}{\partial\phi^2}\frac{\partial^2\epsilon_{tot}}{\partial\theta^2} - \left(\frac{\partial^2\epsilon_{tot}}{\partial\theta\partial\phi}\right)^2\right]^{\frac{1}{2}} \tag{4.2}$$

It can be shown that for an in-plane magnetization the resonance condition deduced by Eq.4.2 is given by [4]

$$\left[\frac{\omega}{\gamma}\right]^2 = \left[-H\cos(\theta_H - \theta_{eq}) + 4\pi M_{eff}(12\sin^2\theta_{eq} - 1) + \frac{K_1}{M_{sat}}(12\sin^4\theta_{eq} - 15\sin\theta_{eq} + 3)\right] \left[H\frac{\sin\theta_H}{\sin\theta_{eq}} + \frac{2K_{eff}}{M_{sat}} + \frac{K_1}{M_{eff}}(\sin^2\theta_{eq} - 1)\right] \tag{4.3}$$

with

$$4\pi M_{eff} = M_{sat} + \frac{2(K_u) + K_1}{M_{sat}},\ K_{eff} = K_u + K_1 \tag{4.4}$$

If the external field lies in the plane of the system, $\theta_H = 90$ the resonance has the following form [5]:

$$\left[\frac{\omega}{\gamma}\right]^2 = [H + 4\pi M_{sat}]\left[H + \frac{2K_{eff}}{M_{sat}}\right] \tag{4.5}$$

This expression can be used to evaluate the magnetic anisotropies, M_{eff} and K_{eff}.

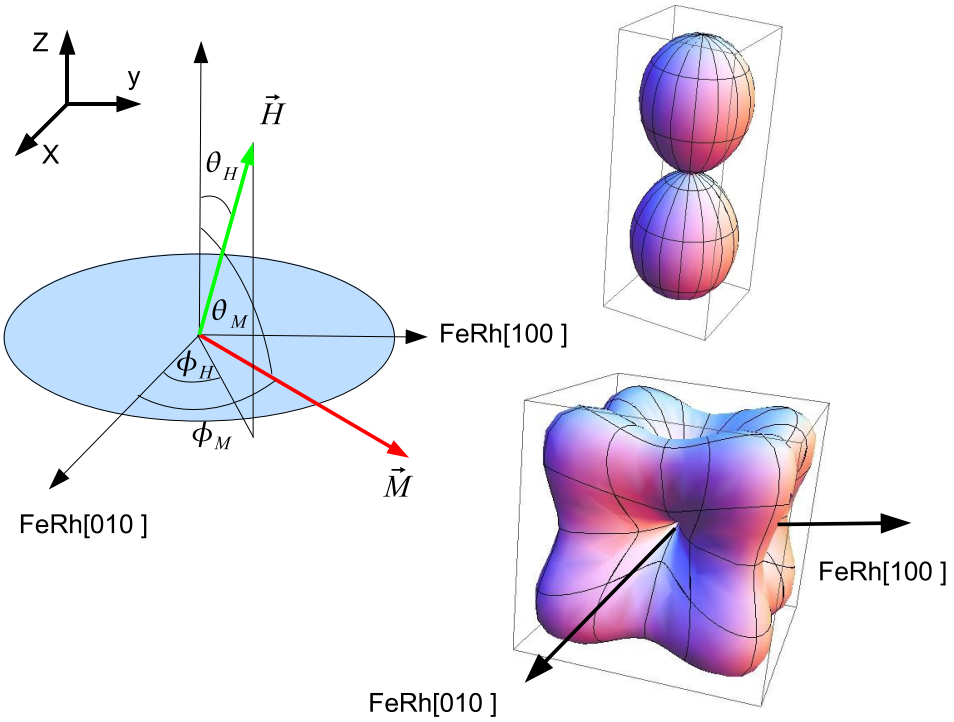

Figure 4.2: (a) Crystallographic directions and definition of the angles. The relative orientation of the axis of FeRh with respect to the MgO substrate axes are depicted. The magnetization **M** is expressed in polar coordinates (θ_M,ϕ_M). The external field **H** can rotate in the plane of the film (θ_H) on rout of the film plane (ϕ_H). (b) Energy surfaces of the first two contributions to the anisotropy energy in FeRh. Top: uniaxial anisotropy term. Bottom: cubic anisotropy term.

4.2 Temperature dependent FMR

The FMR signal has been measured in a temperature range of 80K across the transition in an in-plane configuration with a fixed external frequency of 22 GHz. In Fig.4.3 a) the peak intensity is reported as a function of temperature. The value is extracted according to Eq.2.20. In an absorption process the value of the intensity is evaluated as the integral of the absorption line and is proportional to the number of resonators present in the system [6]. In the FeRh system only the magnetic moments of the ferromagnetic domains will contribute to the absorption of the electromagnetic energy in the waveguide. For

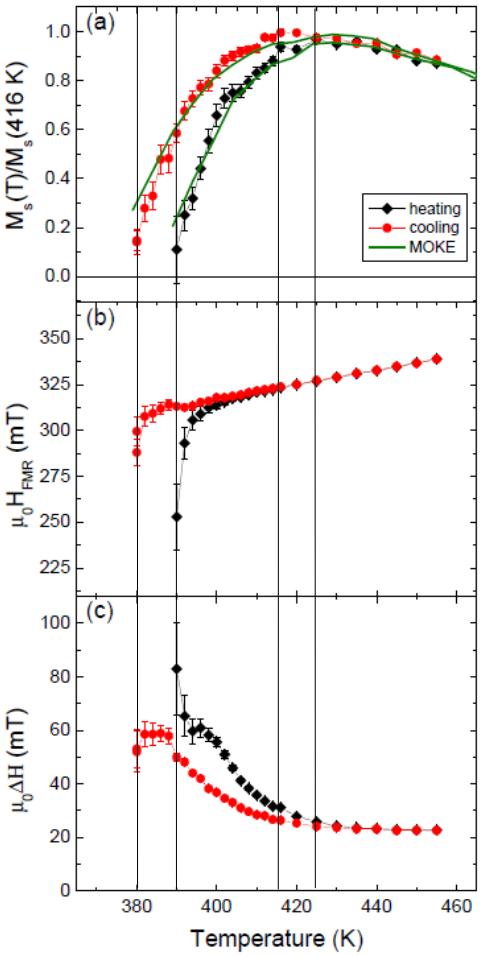

Figure 4.3: The results of the temperature dependent FMR measurement on FeRh. The vertical line correspond to the temperatures defined in the introduction of the chapter a) The integral intensity of the FMR line (corresponding to the integral of the absorption, Eq.2.20) the green line corresponds to the saturation magnetization extracted from MOKE measurements. b) Position of the resonance field H_{FMR}. c) FMR linewidth as a function of temperature.

this reason in the heating branch for $T_{N-FP} < T < T_{FP}$ the intensity of the FMR line increases with increase of temperature, and accordingly in the cooling branch for $T_{AFP} < T < T_{N-AFP}$ it will decrease. It can be shown (Fig.4.3(b)), by superimposing the value of the saturation magnetization extracted from static MOKE measurements, that the temperature dependence of the intensity mimics the dependence of the value of the saturation magnetization M_S. In fact also the saturation magnetization is proportional to the amount of the system volume occupied by the ferromagnetic phase. Usually the intensity of the FMR peak is not used to determine the magnetization of a sample because to extract the actual value of M_S a detailed knowledge of the response function of the setup is needed [6]. In our case this measurement is useful to identify the FeRh absorption peak, and for determining the temperatures defined in the introduction.

In Fig.4.3 b) the position of the resonance field H_{FMR} is reported as a function of temperature. The linear dependence of the position of the resonance peak is due to the change of the anisotropy constants as reported in [5]. This linear dependance can be traced during the transition except when $T \simeq T_{N-FP}$ and $T \simeq T_{AFP}$, where the detection of the signal is difficult due to the low intensity (see Fig.4.3 a). The fact that the change is in the anisotropy constants implies that the ions in the ferromagnetic regions carry the maximum moment since the ferromagnetic domains are formed, confirming the first order nature of the transition where an abrupt change in the total magnetic moment take place within the unit cell.

In Fig.4.3 (c) the dependence of the linewidth on temperature is reported. In the heating branch we see a decrease of the linewidth for increasing temperature down to a minimal value of 25 mT, starting from a value of 83 mT. A similar behavior can be identified in the cooling branch even if it turns out to be shifted by approximately 10 K towards lower temperatures. Assuming that the value of the linewidth for this configuration is the one at T=450K the major increase takes place for $T < T_{FP}$ and $T_{AFP} < T$. In this temperature region the magnetic system in non homogeneous due to the presence of the domains. To give a clear explanation of this phenomenon is not an easy task and at the moment no suitable models have been found in literature. We argue that the presence of the domain boundaries can induce a broadening of the linewidth, since it introduces regions of non uniform orientation of the magnetic moments.

4.3 Anisotropy constants and frequency dependence

In order to determine the magnetic energy landscape (hence the anisotropy fields), the in-plane and out-of-plane angular dependencies of the resonance field have been measured when the system is completely in the ferromagnetic phase, setting $T = 425$ K.

In Fig.4.4(a) the variation of H_{FMR} as a function of the in-plane angle ϕ_H is reported. A sinusoidal behavior suggesting a four-fold anisotropy is clear. This is induced by the strain exerted by the MgO substrate on the film due to lattice mismatch. Beside the

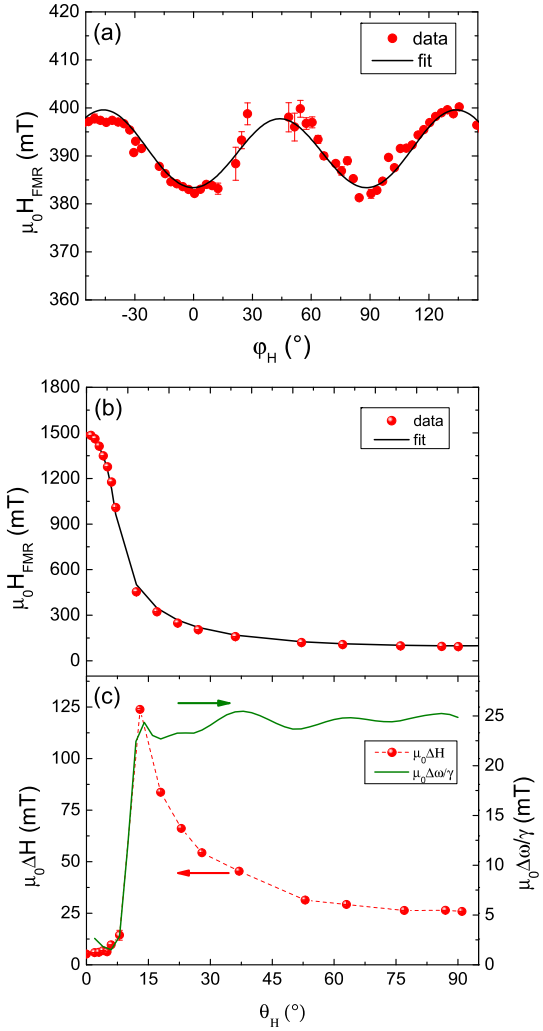

Figure 4.4: (Color online) Angular dependence of FMR at 425 K. (a) in-plane measurements at 22 GHz: Position of the resonance as function of the angle ϕ_H. Out-of-plane measurements at 10 GHz: (b) FMR position and (c) FMR linewidth (in field and frequency) of the resonance as a function of the out-of-plane angle θ_H. All out-of-plane measurements are performed at $\phi_H = 45°$.

case of MgO substrates the samples grown on sapphire do not show such a sinusoidal behavior, suggesting the existence of an easy plane. In Fig.4.1 (b) we report the variation of H_{FMR} as a function of the out-of-plane angle θ_H. The strong variation from the in-plane to the out-of-plane configuration is due to the in-plane orientation of the magnetization is energetically favorable due to the demagnetizing fields, similarly to the case of Zn-Y [7]. From these measurements all magnetic parameters are determined by fitting $H_{\mathrm{FMR}}(\theta, \phi)$ to the free energy density. By this procedure we find the effective magnetization $\mu_0 M_{\mathrm{eff}} = \mu_0 M_{\mathrm{S}} - K_{\mathrm{U}}^{\perp}/M_{\mathrm{S}}$ and the anisotropy fields $\mu_0 H_1^{\perp} = 2K_1^{\perp}/M_{\mathrm{S}}$, $\mu_0 H_1^{\parallel} = 2K_1^{\parallel}/M_{\mathrm{S}}$ and $\mu_0 H_{\mathrm{U}}^{\parallel} = 2K_{\mathrm{U}}^{\parallel}/M_{\mathrm{S}}$. In order to obtain the values of the anisotropy constants we additionally determine the saturation magnetization M_{S} at $T = 425$ K by performing vibrating sample magnetometry (VSM). All resulting magnetic parameters are listed in Table 1. The out-of plane anisotropy field is remarkably large and reduces the effective demagnetizing field $\mu_0 M_{\mathrm{eff}}$ compared to $\mu_0 M_{\mathrm{S}}$ by 0.3 T. Considering the large film thickness this anisotropy is very likely a bulk effect in FeRh and related to the $\mathrm{L1_0}$ crystal structure (alternating Fe and Rh atomic planes).

constant	value	unit
$\mu_0 M_{\mathrm{eff}}$	1.122 ± 0.001	T
$\mu_0 M_{\mathrm{S}}$	1.460 ± 0.020	T
$\mu_0 H_1^{\perp}$	$(-3.2 \pm 1) \times 10^{-4}$	mT
$\mu_0 H_{\mathrm{U}}^{\parallel}$	-1 ± 2	mT
$\mu_0 H_1^{\parallel}$	-8.8 ± 0.3	mT
$K_{\mathrm{U}}^{\perp}$	$(5.2 \pm 0.1) \times 10^5$	$\mathrm{J/m^3}$
$K_1^{\perp}$	(0.23 ± 0.8)	$\mathrm{J/m^2}$
$K_{\mathrm{U}}^{\parallel}$	$(7.3 \pm 1.6) \times 10^2$	$\mathrm{J/m^3}$
$K_1^{\parallel}$	$(6.4 \pm 0.8) \times 10^3$	$\mathrm{J/m^3}$

Table 4.1: Magnetic parameters of FeRh/MgO(001) determined by FMR. The value for $\mu_0 M_{\mathrm{S}}$ was measured independently by vibrating sample magnetometry

The out-of-plane angular dependence of the FMR linewidth is reported in Fig. 4.4(c). The linewidth (red dots) reaches its minimum value when the magnetization is oriented perpendicular to the film plane. The following increase (maximum occurs for $\theta_H = 15°$) is due to the dragging of the magnetization behind the external field.

From the measurements of the linewidth as a function of angle and as a function of frequency one can derive information on the damping and on its origin. The contribution to the damping and hence to the linewidth can be extrinsic and intrinsic. Three are the process that originates the intrinsic contribution: eddy currents, magnon-phonon scattering and spin-orbit coupling [8]. Eddy currents play a negligible role in ultra-thin sample and phonon-magnon scattering leads to a too small contribution to explain the

measured damping in ferromagnetic metallic systems [8]. The most important source of damping in metallic ultrathin films is the interaction of itinerant electron [9]. Heinrich and coworkers proposed a model where they estimated the effect on the damping of the interaction of itinerant s-p electron and localized d sates [10]. A detailed description of the model is behind the scope of this work. On the other hand the extrinsic contribution to the damping is mostly due to the presence of defects, or inhomogeneities, and to the two-magnon scattering. The former can be only reduced by improving the quality of samples, but only until a certain extent: one can never get a defect-free sample. The latter mechanism can be turned off when the sample magnetization and the external field are perpendicular to the sample plane, namely when $\theta_H = 0$ [9, 11]. Hence by performing an out of plane angular dependence of the linewidth is possible estimate the contribution to the damping of the two-magnon scattering by comparing the measured linewidth in the in-plane and in the out-of-plane configurations. Hurben and Patton have shown how this effect is clearly visible if one derive the frequency linewidth dependence on the angle $\Delta\omega\left(\theta_H\right)$ [12]:

$$\Delta\omega\left(\theta_H\right) = \left(\frac{d\omega}{dH}\right)_{\text{at FMR}} \Delta H\left(\theta_H\right) \tag{4.6}$$

where we derived $\frac{d\omega}{dH}$ from Eq.4.2. In Fig.4.4 (c) the angular dependence of ΔH and $\Delta\omega$ is shown, where Eq.4.6 has been used to extract $\Delta\omega$. The increase by a factor of 5 in the linewidth found in the in-plane configuration is caused by two magnon scattering (see Fig4.4(c)).

To estimate the intrinsic damping, the frequency dependence of the linewidth has been measured in the perpendicular configuration, where the two magnon scattering contribution is ruled out, as shown in Fig.4.5. It has been shown that the intrinsic contribution to the damping has a linear dependence on the frequency and is expected to go to zero if the frequency is zero [9]. Nevertheless, extrapolating the linewidth at zero frequency from the experimental data, in many samples a non zero linewidth is found [13]. For this reason we analyzed the frequency dependence data using the following relations

$$\omega_{\text{FMR}} = \gamma\left[H_{\text{FMR}} - 4\pi M_{\text{eff}}\right] \tag{4.7}$$

$$\mu_0\Delta H\left(\omega\right) = \mu_0\Delta H\left(0\right) + \alpha\frac{\omega}{\gamma} \tag{4.8}$$

The first equation is used to extract the value of γ , and once γ is know the g-factor can be derived. In the second equation, the first models the behavior of the intrinsic contribution to the damping while $\Delta H\left(0\right)$ gives the extrinsic contribution, in particular the one coming from defects. From the fit we obtained $\gamma = 1.836 \cdot 10^7 Hz/Oe$ corresponding to a g-factor of 2.05 ± 0.06. The value of γ is then used to fit the frequency dependence of the linewidth from which we extracted the Gilbert damping $\alpha = 0.0013 \pm 0.0008$. The results of the fit are reported in Fig.4.5. We obtained a value of $\Delta H\left(0\right)$=5.3±0.4 mT. Since there are no data on FeRh thin films, we can not comment on the quality the considered sample.

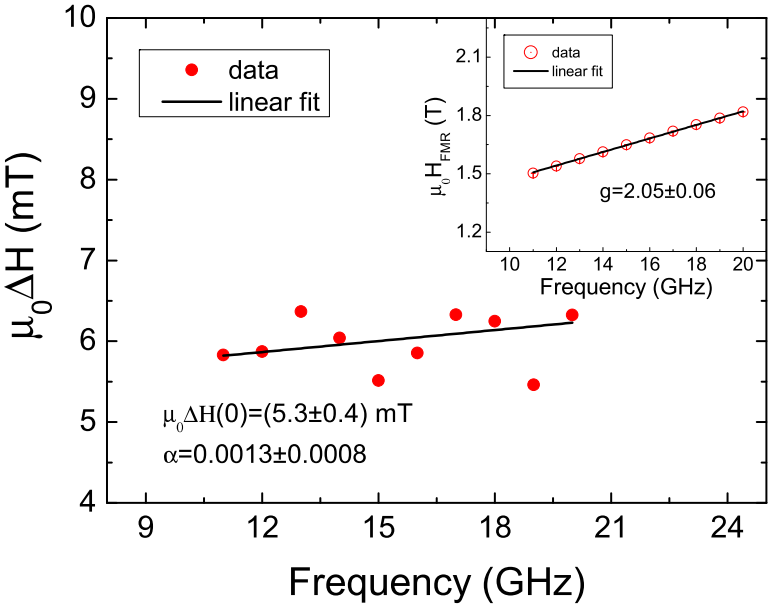

Figure 4.5: (Color online) Frequency dependence of the resonance linewidth and position (Inset) measured in the perpendicular configuration ($\theta_H = 0°$) at 425 K. From these measurements the Gilbert damping constant and the g-factor are determined.

4.4 Conclusions

In conclusion we investigated the dynamic properties of single crystalline FeRh thin films by ferromagnetic resonance. The comparison of the temperature dependence of magnetic moment and the position of the resonance, allowed us to describe qualitatively the nucleation and the growth of the magnetic domains and to confirm the first order nature of the phase transition. The energy landscape of the magnetization has been investigated by studying the angular dependence of the FMR lineshape of the FeRh in the ferromagnetic phase. We where able to determine the anisotropy constants of a thin film of FeRh which where not reported in literature sofar. Further more we where able to identify and estimate the role of the two-magnon scattering process in the damping. This allows us to extract the value of the g-factor and of the Gilbert damping parameter α.

References

[1] F. Keffer and C: Kittel. Theory of antiferromagnetic resonance. *Phys. Rev.*, 85:329, 1952.

[2] S. V. Vonsovskii, editor. *Ferromagnetic resonance.* Pergamon Press, 1966.

[3] H. Suhl. Ferromagnetic resonance in nickel ferrite between one and two kilomegacycles. *Phys, Rev.*, 97:555, 1955.

[4] C. Kittel and P. McEuen. *Introduction to solid state physics*, volume 7. Wiley New York, 1976.

[5] F. Gerhardter, Y. Li, and K. Baberschke. Temperature-dependent ferromagnetic-resonance study in ultrahigh vacuum: Magnetic anisotropies of thin iron films. *Phys. Rev. B*, 47:11204, 1993.

[6] R.S. Alger and I. Hayashi. *Electron paramagnetic resonance: techniques and applications.* Interscience Publishers, 1968.

[7] M.J. Hurben, D.R. Franklin, and C.E. Patton. Angle dependence of the ferromagnetic resonance linewidth in easy-axis and easy-plane single crystal hexagonal ferrite disks. *J. Appl. Phys.*, 81:7458, 1997.

[8] B. Heinrich and J.A.C. Bland. *Ultrathin Magnetic Structures: Measurement techniques and novel magnetic properties*, volume 2. Springer Verlag, 2005.

[9] G. Woltersdorf. *Ph.D. Thesis.* PhD thesis, Martin-Luther-Universität, Halle, 2004.

[10] B Heinrich, D. Fraitovà, and V Kambersky. The influecnce of the s-d exchange on relaxation of magnetos in metals. *Phys. Stat. Sol.*, 23:501, 1967.

[11] B. Heinrich and JF Cochran. Ultrathin metallic magnetic films: magnetic anisotropies and exchange interactions. *Adv. Phys.*, 42:523, 1993.

[12] M.J. Hurben *et al.* Theory of two magnon scattering microwave relaxation and ferromagnetic resonance linewidth in magnetic thin films. *J. Appl. Phys.*, 83:4344, 1998.

[13] Celinsky Z. and B. Heinrich. Ferromagnetic resonance linewidth of Fe ultrathin films grown on a bcc Cu substrate. *J. Appl. Phys.*, 70:5935, 1991.

Chapter 5

Magnetization and structural dynamics across the phase transition.

In this chapter the interplay between electronic, lattice, and magnetic systems in FeRh triggered by an ultra-fast laser pulse is investigated. In particular the time scales at which the different dynamics develop are extracted and compared. In order to explain the correlation between the structural change and the onset of the magnetization, a phenomenological model is proposed and discussed. Part of the reported results have been published in Physical Review Letters [1].

5.1 Introduction

Many different experimental groups focused their attention on the dynamics of the phase transition in FeRh [2, 3, 4]. There are two aspects which make this topic of extreme interest both from a technological and theoretical point of view. First, in this transition one observes the onset of ferromagnetic order by increasing the temperature above a critical value which is above room temperature. Usually the onset of the ferromagnetic order is the result of a process where the system is cooled below T_C starting from a paramagnetic state. Such a process is usually slow because it is limited by the possibility of thermally removing energy from the system. The second interesting aspect is that the magnetic transition is accompanied by an isotropic expansion of the volume of the system, suggesting a strong interaction between the lattice and the magnetic order.

Since the pioneering work of Beaurepaire 1996 [5], one of the preferred tools to investigate ultra-fast magnetization dynamics are laser pulses, used as an ultra-fast excitation source. In the cited work, for the first time the magnetization change induced by a laser pulse has been observed, and, more specifically a reduction of the magnetization, called laser induced demagnetization. Since then, the same effect has been measured in many magnetic materials and the study of demagnetization dynamics became one of the principal tools for the investigation of interaction between the magnetic system, electrons and

phonons.

The transition in FeRh offers the extraordinary possibility to generate ferromagnetic order out of an anti-ferromagnetic ground state by using a laser pulse as an ultra-fast source of heat. Such a kind of phenomenon can be of great interest for the development of magnetic devices in which the manipulation of the magnetic state can be performed at a picosecond or sub-picosecond scale. By performing pump-probe experiments on a thin film of FeRh and by measuring the time resolved Kerr rotation, Ju and coworkers claimed to have observed the onset of the magnetization within a picosecond, see Fig.5.1 [6]. Almost simultaneously Thiele and coworkers reported to have observed an even faster onset of the magnetization [2].

In this chapter we report the results of pump-probe experiments performed to identify and determine the time scales of the phase transition by selectively probing the electronic, magnetic and lattice response to the ultra-fast optical excitation of the system. We do this by performing Time-Resolved MOKE (TR-MOKE) and Time-Resolved X-Ray Diffraction (TR-XRD)experiments described in chapter 2. In order to compare the results all the experiments have been performed on the Ta1 sample, and under the same experimental conditions (starting temperature, fluence, wavelength and pulse duration of the pump pulse.)

5.2 Transient reflectivity

The easiest experiment to perform in order to determine if it is possible to induce the phase transition in a thin film of FeRh with our laser system, consists in measuring the time resolved reflectivity as a function of fluence. Thermo-reflectivity has been used since a long time to determine the relaxation time of metals optically excited with an ultra-short laser pulse [7]. In this case the energy delivered to the electronic system increases the electronic temperature on a timescale comparable to the laser pulse temporal duration. The energy is then transferred to the lattice by electron-phonon coupling [8]. The reflectivity shows a peak in correspondence to the arrival of the laser pulse due to the increase of the electronic temperature, followed by an exponential decay where the energy is first delivered to the lattice and then it diffuses through the whole system volume due to thermal transport. This dynamics can be well described in terms of a Two-Temperature model where also the heat diffusion into the substrate is taken into account [9]. Ju and coworkers in [6] report the fluence dependence of the reflectivity for a 100-nm thick sample of $Fe_{45}Rh_{55}$ grown on MgO(100). In this work it has been shown that the reflectivity of FeRh does not decay monotonically after the electronic peak for fluences $\Phi_{Tr} > 5.8$ mJ/cm^2, but reaches a second maximum after 30-35 ps and then starts an exponential decay. The extra feature in the reflectivity signal has been attributed to the phase transition since the anomalous change in both the lattice constants and in the magnetic order can influence the electronic occupation of the system's bands and hence the optical absorption, giving an unambiguous

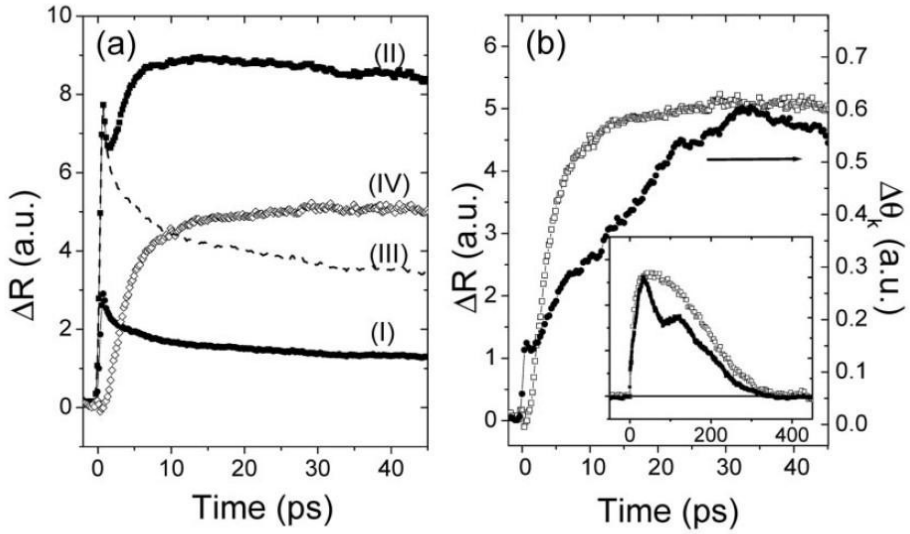

Figure 5.1: Data reported by Ju and coworkers in [6]. (a) The sub- and super-threshold thermo-reflectivity of a FeRh thin film (curve (I) and (II) respectively). The reflectivity shows a second maximum after the electronic peak for super-threshold fluences. The open circles (IV) curve is the extracted anomalous contribution to the reflectivity observed obtained by subtracting a rescaled subthreshold curve (III) (see discussion in text). (b) The closed circle curve represent the Kerr rotation induced by the laser pulse compared to the anomalous contribution to the reflectivity. The early jump is interpreted by the authors as an onset of the ferromagnetic order at ps-scale. Figure from [6].

fingerprint of the transition. In order to extract the so called "lattice contribution" to the reflectivity, a subthreshold reflectivity curve (which does not show a second peak after the electronic one) has been rescaled so its electronic peak height matches the height of the electronic peak of the super-threshold curve and than subtracted from the latter [6, 3], see Fig.5.1.

We investigate the reflectivity change induced by a laser pump pulse to determine if we can induce the transition from the AFP to the FP and we applied the procedure of Ju to separate the "lattice contribution" from the reflectivity. For our experiments we used the laser system described in Chapter 3 in an all-optical pump-probe experimental setup where the pump beam has been focused down to 51 μm spot size and the probe to 21 μm, to guarantee that the probe volume is uniformly heated. The results of our experiment are shown in Fig.5.2(a) where the full delay scans for 5 different fluences are reported. It can be seen that for the first two fluences (0.7 and 1.3 mJ/cm^2) the

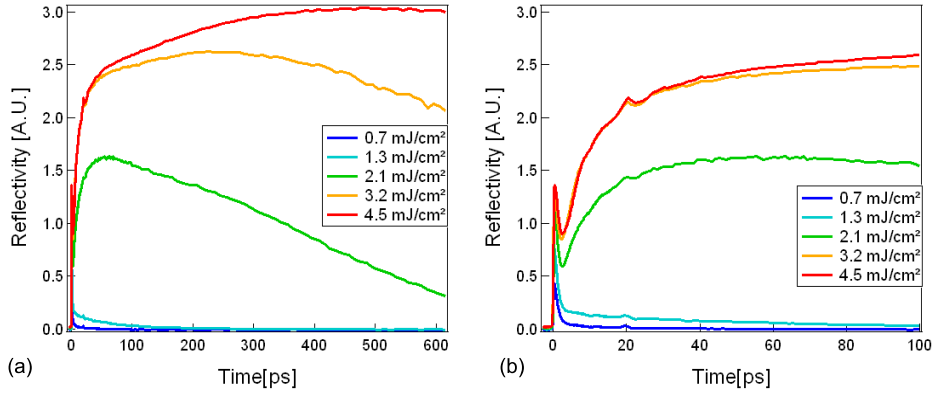

Figure 5.2: (a) Laser induced transient reflectivity measured on Ta1. The measurement are shown for 5 different fluences. For the two lowest ones the decay after the electronic peak is monotonic. (b) For all the fluences greater than Φ_{Tr} a second maximum is reached.

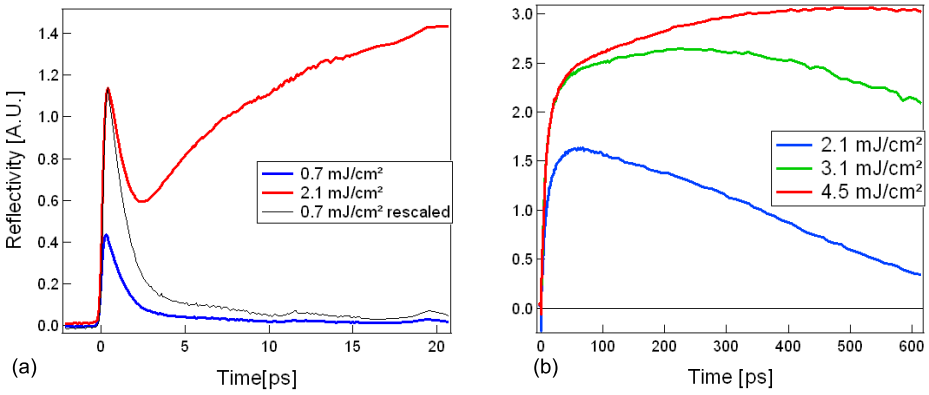

Figure 5.3: (a) To extract the contribution of the phase transition to the reflectivity a subthreshold curve (blue) is rescaled (black) and then subtracted from a superthreshold curve (red). (b) The contribution from the transition for all the superthreshold reflectivity curves.

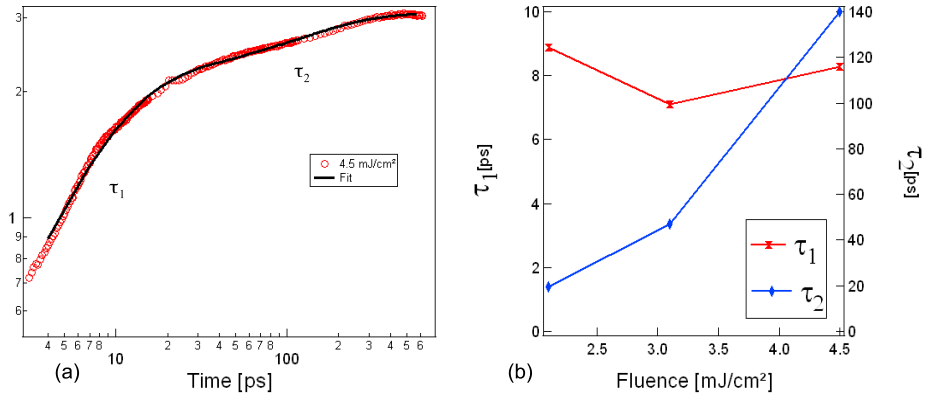

Figure 5.4: (a)The result of the fit of the rising part of the "lattice contribution" signal for 4.5 mJ/cm^2 in a log-log scale. The two different time constants account for the two different slopes in observed in the signal (b) Time constants extracted from the fit on Ta1 for different fluences.

reflectivity, after the electronic peak, shows an exponential decay towards zero, which is typical for the subthreshold regime, namely if no phase transition occurs the system behaves as a standard metal well described by the Two Temperature model. For fluences higher than 1.3 mJ/cm^2 a deviation from the normal metal behavior starts 4-5 ps after the electronic peak. We find that the value of the threshold fluence for Ta1 is $1.3 < \Phi_{tr} < 2.1$ mJ/cm^2. The differences between the values of the thresholds reported by various groups can be attributed to the difference between the samples, since it depends critically on the quality of the sample, wavelength of the incident radiation and presence and composition of a capping layer. The rise of the extra contribution to the reflectivity can be better appreciated by plotting the reflectivity in a 100 ps delay range after the laser excitation, see Fig.5.2 (b). Furthermore an oscillation can be noticed in all the curves at 20 ps. These oscillations are due to the reflection of the elastic waves generated by the laser pulse from the substrate interface and are called phonon echoes [10, 11]. Since the elastic waves travel at the speed of sound in FeRh, it is possible to measure it knowing the thickness d of the sample. By using $v_s = 2d/\Delta t$ and with $d = 50$ nm and Δt=20 ps, we obtained v_s= 5 km/s, which is in good agreement with values reported in the literature [12], or determined with time resolved X-ray diffraction (see next section). The relaxation back to zero is related to heat diffusion since it develops on a nanosecond range, and only little more information can be extracted from this part, since it is expected that the three subsystems (electron, phonons and magnetic order) are at thermal equilibrium and all together relax back to the ground state. For this reason the results of the fit of the relaxation are not reported nor discussed.

By processing the reflectivity curves as proposed by Ju, we extracted the contribution of the phase transition for the fluences above threshold, Fig.5.3(a). A curve taken with a fluence below threshold (blue curve) has been rescaled (black curve) so that the electronic peak height will match the one of a curve taken with a fluence above threshold (red curve), and than subtracted from the latter curve. The procedure has been applied to all the curves with fluence above threshold and the results are reported in Fig.5.3(b). In order to compare the dynamics entailed by the extra contribution to the reflectivity with the magnetization dynamics probed by the MOKE and with the X-ray diffraction data, we try to fit the rising part of the curves with a single exponential function. It turns out that the "lattice contribution" to the reflectivity is well fitted by a double exponential function, where the fit parameters are the time constants τ_1^R and τ_2^R. The function used in the following is:

$$f(t) = A * exp(\frac{t}{\tau_1^R}) + B * exp(\frac{t}{\tau_2^R}) \tag{5.1}$$

This implies that the modification of the optical absorption induced by the phase transition is the result of at least two different processes. The results of the fitting procedure are reported in Fig.5.4(a). From the fit we extracted the value of the time constants and plotted versus the fluence, Fig.5.4(b). The time constant τ_1^R shows a weak dependence on the fluence. It can be seen it remains almost constant with an average value of 8.1±0.9 ps. On the other side τ_2^R increases with increasing fluences, ranging from 20 up to 140 ps. For a further interpretation of this behavior the dynamics of the reflectivity will be compared to the magnetization and to the lattice dynamics discussed in the following sections. In order to determine the origin of the extra contribution to the reflectivity, the extracted time constants will be compared to those extracted from MOKE and X-ray data. If the hypothesis of a lattice origin proposed by Bergmann and coworkers is correct, the time constant extracted from the reported curves is expected to be comparable with the ones extracted from the lattice dynamics. We will show that the time scales of the reflectivity are quite different from the timescales extracted from the following experiments.

5.3 Transient X-ray diffraction

In order to distinguish the magnetic and electronic dynamics from the lattice one, we performed time resolved X-ray diffraction experiments at the FEMTO beamline at the Swiss Light Source (SLS). Since every change in the crystal structure of the system corresponds to a change in the diffraction pattern, the lattice dynamics induced by the laser pulse is investigated by the measurement of the change in position, intensity and shape of the Bragg peak related to the reflection from the crystal planes of FeRh. In order to distinguish between the reflections coming from the FeRh and the reflections coming from the substrate, static x-ray diffraction experiments have been performed on NC0 and NC1. The experiments have been performed by S.O. Mariager at SLS using a Seifert

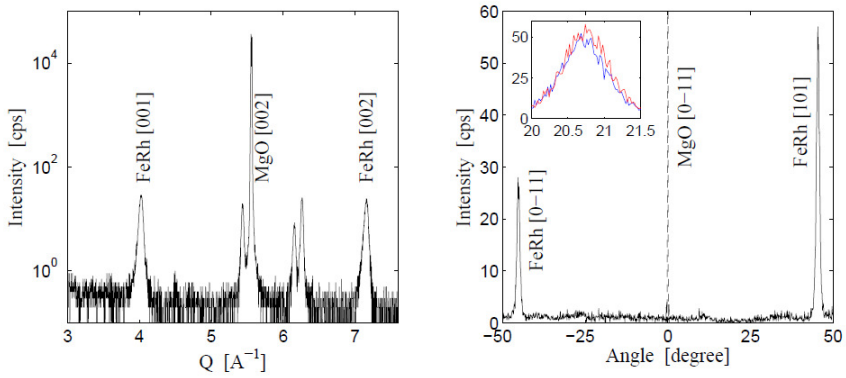

Figure 5.5: X-ray diffraction characterization of NC0. Left: the specular scan reveals the orientation of the crystal with respect to the substrate, in particular it has been found the that $[001]_{FeRh} \parallel [001]_{MgO}$. Right: The epitaxy of the crystal has been determined from the in-plane rotation scan: $[110]_{FeRh} \parallel [100]_{MgO}$. The absence of secondary peak indicate a single crystal sample. The measurement and the figure has been made by S.O. Mariager, and taken from [13].

$(\theta - 2\theta)$ scan is reported. The presence of the FeRh [001] and [002] peaks, together with the MgO [002] reveal the orientation of the planes parallel to the the substrate plane of the system. Using the Bragg law an average lattice constant of 3.02 Å has been estimated. This value is about 1% bigger then the tabulated value of 2.988 Å, suggesting a in-plane expansion of the crystal structure. An in-plane expansion of about 0.33 % has also been observed by Maat and coworkers in [4] on a 100 nm thick sample. This is in good agreement with the expansion observed in our sample because it is expected to be less pronounced in bulky films. The in-plane orientation has been determined by rotating the sample around the surface normal after having identified the {101} off specular reflection of the FeRh film. From the scan reported on the right side of Fig.5.5 it can be derived that $[110]_{FeRh} \parallel [100]MgO$. This was expected since $\sqrt{2}a_{FeRH} = 4.226\mathring{A}$ which is similar to the tabulated value of the MgO lattice constant.

The time resolved XRD experiments have been performed by imaging the (101) Bragg peak. A detailed description of the experimental setup and of the detector characteristics can be found in [1, 13] and related references. Since the lattice expansion results to be constrained in the in-plane directions, the expansion occurs parallel to the film normal. In Fig.5.6(a) the relative shift of the center of mass of the (101) peak of FeRh is reported as a function of time and fluence. Due to the aforementioned constraint in the expansion the shift occurs only in the perpendicular component of the relative reciprocal vector

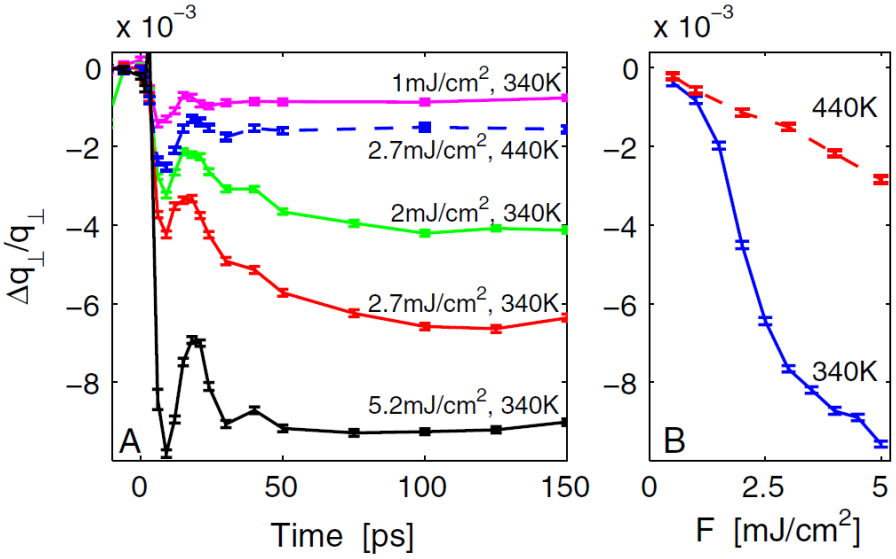

Figure 5.6: (A) The relative change in the position of the center of mass of the Bragg peak as a function of fluence for two different sample temperatures. (B) Shift of the Bragg at 145 ps as a function of fluence for two different starting temperatures. For T=340K a non-linear expansion expansion of the lattice is observed above 1.3 mJ/cm^2. For T=440 K the ferromagnetic phase is fully developed and the usual linear expansion is observed.

$\mathbf{q} = \{q_1, q_2, q_\perp\}$, where the first two components are relative to the in-plane expansion, and $q_\perp$ to the perpendicular expansion. A negative shift in reciprocal space corresponds to an expansion in real space. The curve relative to the fluence of 1mJ/cm^2 is a subthreshold curve taken at a sample temperature below $T_{AFP\rightarrow FP}$ (temperature at which the FP starts to nucleate in the AFP). It can be seen that after two damped oscillations the position of the Bragg peak reaches a new equilibrium position corresponding to the expanded lattice due to heating. The oscillation is a fingerprint of a thermally induced strain wave [14] and the period is given by the time it takes for the wave to travel back and forth along the film thickness. We can extract a value for the speed of sound of 5.1 km/s which is consistent with the one extracted from the phonon echoes and with the value reported in literature [12]. By increasing the fluence the strain wave is still present, but the new equilibrium position of the peak is reached at longer delays. This is particularly true at intermediate fluence where the maximum is reached after 100 ps. At the maximum fluence measured, however, the maximum shift is again reached on a timescale comparable with the strain wave. Due to the difference in the time scales of the strain wave and the maximum shift, we state that the strain wave is not the driving force of the phase transition. The

temperature of the sample has been raised to 440 K, well above T_{FP} (temperature at which the FP is fully developed), and the pump-probe experiment has been repeated. In this way we prevent the transition to occur and, as can be seen in the blue curve, the behavior of the peak shift is the same as that for subthreshold fluence starting from room temperature. This confirms that the peak shift observed at intermediate fluences is strictly related to the induced phase transition. In Fig.5.6(b) the peak shift at a fixed delay of 145 ps is reported as a function of fluence. This is equivalent to a measurement of the shift of the Bragg peak as a function of temperature since at this time delay the system is again in thermal equilibrium (from a three temperature model point of view this means the the three heat baths have all the same temperature, and the final temperature at which they thermalize is given by the fluence of the laser only). The measurements have been made for two different starting temperatures, one below (340 K) and one above (400K) T_{FP}. In the latter case the usual linear dependence of the peak shift is given only by the thermal expansion of the system. In the former case a marked deviation from the linear behavior can be observed at intermediate fluences. This deviation is the unambiguous fingerprint of phase transition in the XRD data.

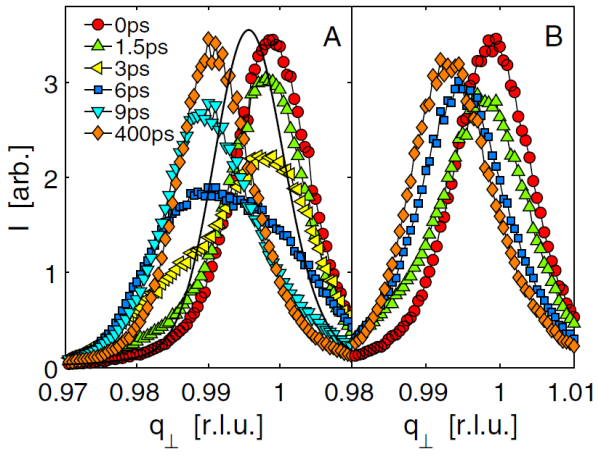

Figure 5.7: Profile of the Bragg peak at different time delays. (A) for 5.2 mJ/cm^2 and (B) 2.7 mJ/cm^2. The solid line marks the expected position of the peak after 6 ps due to only the thermal expansion.

Due to the first order nature of the phase transition, a coexistence of two different phases is expected. From a structural point of view, the two phases have different lattice constants and therefore it is expected that the two phases have different reciprocal lattice, or the Bragg peaks should sit on slightly different positions. It has been show by Kim

and coworkers in [15], that indeed the Bragg peaks of the two different phases are shifted. They measured the peak profile from a thin film of FeRh while statically heating the system above the transition temperature. They show that the peak does not move in the new position but the original peak relative to the AFP decreases while a new peak, slightly shifted, relative to the FP rises. At intermediate temperatures, $T_{AFP\rightarrow FP} < T < T_{FP}$ and $T_{AFP} < T < T_{FP\rightarrow AFP}$ the presence of both the peaks confirms the coexistence of the two phases. We have measured the profile of the Bragg peak at different time delays for two different fluences, and reported the results in Fig.5.7. In the curve at zero delay a single peak is clearly visible for both fluences. At a time delay of 3 ps (yellow triangles curve) it can be seen that the peak develops a shoulder for lower values of $q_{\perp}$, while the maximum of the peak decreases. At higher delays the shoulder develops to a new peak while the initial peak disappears. The position of the new peak is consistent with an out of plane expansion of about 1%. This supplies a strong evidence for the coexistence of the two phases during the development of the transition, and so far it is the first time that the time evolution of the transition is measured. The solid line reported in Fig.5.7(a) marks the position expected for the Bragg peak of the AFP if only a thermal expansion of the lattice was active. The fact that the position of the FP peak does not coincide with the calculated one further confirms the deviation from the linear behavior of the lattice expansion if the phase transition is involved. In order to give a quantitative estimation

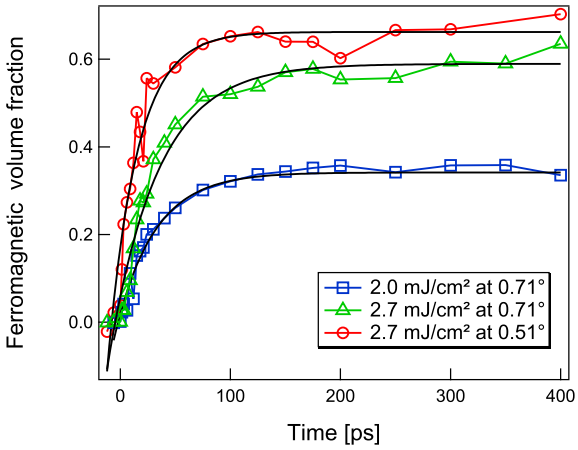

Figure 5.8: The ferromagnetic volume fraction extracted from the peak area, For two different fluences and for two different grazing angle of the x-rays.

of the induced structural change, the contribution of the transition has been separated from the lattice oscillations. The strain wave has been modeled as a damped sinusoidal wave and its contribution subtracted from the measured curves. Even if the separation of the two peaks in our experiment is limited by the grazing incidence and by the relatively

low energy of the x-rays, the contribution of the two phases can be separated by fitting the peak profile reported in Fig.5.7 as a sum of two symmetric functions (reported in [1]). The integral under the Bragg peak of the FP is proportional to the ferromagnetic fraction of the probed volume,V_{FP}/V_{pr}, where V_{pr} is the probed volume. We used two different grazing angles in order to probe different volumes of the sample, at α=0.71° the x-rays probe the entire volume and at α=0.51° their penetration depth is 15 nm. The calculated ferromagnetic volume fraction for two intermediate fluences and for two different values of the X-ray incidence angle are reported in Fig.5.8. It can be seen that the fluences used are not sufficient to induce a full development of the FP since V_{FP}/V_{pr} is always less than 1 when the whole sample is probed (α=0.71°). When the probing depth is reduced (α=0.51°) we notice that the ferromagnetic fraction reaches a maximum of 65% and reaches the saturation value faster. This suggests that the phase transition starts at the free interface of the sample and then expands toward the substrate interface. To model this behavior we assumed that for a certain fluence one can define a maximum ferromagnetic volume fraction V^*_{FM}. We assume further that the sample is impulsively heated at a temperature $T^* > T_{AFP\rightarrow FP}$ and that the growth of the FP is due to the nucleation of independent ferromagnetic domains at a constant rate τ_1. Since $V_{AFP}+V_{FP}=1$ then the following equation holds

$$\frac{dV_{FP}}{dt} = \frac{V_{AFP} - (1 - V^*_{FP})}{\tau_1} = \frac{V^*_{FP} - V_{FP}}{\tau_1} \tag{5.2}$$

This is basically the model for the phase change dynamics proposed by Avrami, where the expansion of the domains is suppressed [16, 17]. The solution of the differential equation is given by an exponential law $V^*_{FP}\left[1 - \exp\left(-t/\tau_1\right)\right]$, where the dependence on the fluence enters through the amplitude constant V^*_{FP}. This function has been used to fit the data reported in Fig.5.8. The value found for the time constants at intermediate fluences when the full depth is probed are the same within the error bars and equal to $\tau_1 = 32 \pm 2$ ps. When only a depth of 15 nm is probed the fit gives $\tau_1 = 14 \pm 3$ ps. Since we have calculated a penetration depth of the pump laser of 14 nm starting from the optical constants of FeRh reported in by Rhee and Lynch [18], for α=0.51 the volume probed by the X-rays is the same as the volume excited by the pump. In this case it can be observed that the volume fraction slightly increases because the deep part of the volume, which is not directly heated by the pump, does not contribute to the signal, hence the ratio V_{FP}/V_{pr} is bigger. The rise of V_{FP} in this volume region is significantly faster, implying that the nucleation starts close to the free surface of the sample. This gives also the critical speed at which the structural phase transition develops.

5.4 Transient MOKE

In this section we present the time resolved MOKE experiments performed on Ta1 for different fluences, and the results are reported in Fig.5.9(a). The Kerr rotation shows

the threshold behavior already noticed in the reflectivity. Like in the reflectivity data, the threshold can be identified at 1.3 mJ/cm^2. For super-threshold fluences the signal increase up to a maximum value reached on the hundred ps range. For fluences lower than 1.3 mJ/cm^2 the Kerr signal is identically zero on the hundred ps range while it shows an oscillatory behavior in the first 40 ps. Since the energy is not sufficient to induce the phase transition, the signal should come from the AFP. A possible explanation is that even if the local temperature is not enough to start a nucleation of FP, in can induce a misalignment of the Fe moments inducing a net local moment. This moment interacts with the external field and relaxes back to the initial position, originating the observed oscillations, Fig.5.9(b). At higher fluences after a first oscillation the Kerr signal experiences a monotonic increase up to the maximum. This suggests that the nucleation and expansion of the FP starts after 10 ps. Our interpretation for the super-threshold Kerr behavior is that the FP nucleates domains which are to far from one another to interact and in each domain the magnetization is randomly oriented. By the interaction with the external magnetic field the local magnetization tends to rotate towards the field direction in order to minimize the dipolar energy. Further more the expansion of the domains will cause the fusion of different domains (coalescence). Since the domains which nucleate with the magnetization already aligned with the external field are energetically favored they will tend to align the magnetization of the neighboring domains. This behavior has been measured on all the other samples investigated with our setup. We conclude that no sub-ps or ps onset of the FP is detected with our setup. In order to describe the observed magnetization dynamics, we propose a model based on the following assumptions. First the ferromagnetic domains nucleate with a magnetization along one of the n fixed direction. This assumption is in accordance with the observed 4-fold anisotropy in the sample plane. Second, among the fixed direction, we assume that one is aligned with the external field. A fraction of the FP volume is occupied by domains with magnetization aligned with the external field, V_1, while in the other fraction, V_{n-1}, the magnetization of the domains points in one of the remaining n-1 directions. Two conditions have to by satisfied: $V_1+V_{n-1}=V_{FP}$ and $V_{FP}+V_{AFP}=1$. As mentioned before expansion of the aligned domains occur per coalescence at expenses of the non aligned domains. Such a process can be modeled with a system of coupled differential equations

$$\frac{dV_{n-1}}{dt} = \frac{n-1}{n}\frac{dV_{FP}}{dt} - \frac{V_1 V_{n-1}}{\tau_2} \tag{5.3}$$

$$\frac{dV_1}{dt} = \frac{1}{n}\frac{dV_{FP}}{dt} + \frac{V_1 V_{n-1}}{\tau_2} \tag{5.4}$$

The first term describes the nucleation of the FP. We assume that this process is the same as that described in the structural dynamics section, namely is well described by an exponential growth with τ_1 as time constant. The second term gives the coupling between the evolution of the two volume fractions, $\frac{V_1 V_{n-1}}{\tau_2}$ as a function of a single time constant τ_2 [1]. The Kerr signal will be proportional to the component of the magnetization along

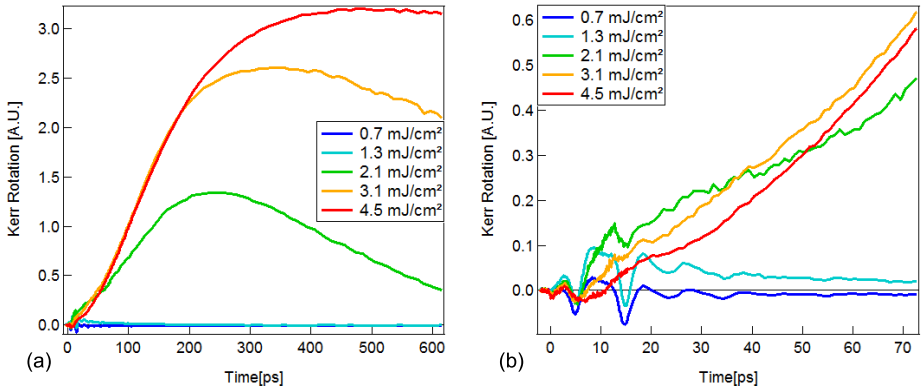

Figure 5.9: (a) Time dependence of the Kerr rotation for 5 different fluences. The appearance of a maximum on the hundred ps range has been measured only for fluences greater than 1.3 mJ/cm^2. (b) Details of the Kerr rotation on the first 75 ps. An oscillation with a frequency of 100 GHz is observed for subthreshold fluences. This oscillation is present also above threshold but it is quenched by the increase of the Kerr rotation due to the development of the FP.

the direction of the external field $\mathbf{m}_1 = V_1 - V_{n-1}/(n-1)$, where V_1 is the volume fraction where the magnetization is directed opposite to the external field. The result of the fitting process for the curve at 4.5 mJ/cm^2 is reported in Fig.5.10(a). The fit has been made keeping the parameter n=4 fixed, which gives the optimum agreement for the fit. This value is compatible with the in-plane magnetization expected for the FeRh thin films (see Appendix A). In Fig.5.10 (b) the extracted time constants are plotted as a function of the fluence. τ_1 shows a weak dependence on the fluence and the value is comparable to that extracted from the XRD experiments for $\alpha = 0.51$. Since the penetration depth of the probe beam is 14 nm we can conclude that the observed nucleation time of the structural and magnetic domains are comparable. The process of re-alignment of the magnetization during the expansion of the FP is governed by τ_2. The dependence from the fluence can be caused by the non complete establishment of the FP, and this is consistent with the XRD data from which we know that at this fluences the development of the FP reaches a maximum of 65%.

5.5 Discussion

The dynamics of the phase transition shows a big degree of complexity, since it involves simultaneously electrons, lattice and magnetic order. The XRD experiments allow to

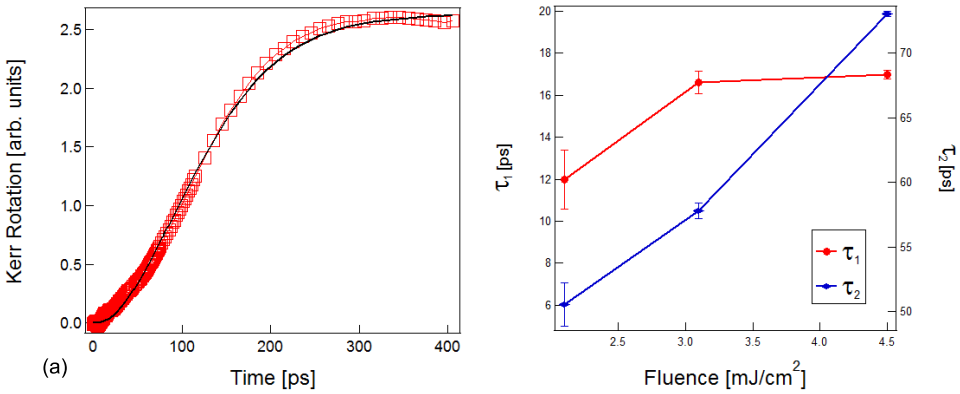

Figure 5.10: (a) The result of the fit using the proposed model of the Kerr rotation measured at 4.5 mJ/cm^2. (b) The time constants extracted from the fit as a function of fluence.

probe selectively the lattice dynamics and from them we can follow the process of nucleation of the new structural phase. We can conclude that the nucleation take place in the first 14 nm close to the free interface within the penetration depth of the pump pulse. Assuming that this volume is uniformly heated, we estimated that the onset of the new phase follows an exponential law with a time constant of 14 $\pm$ 3 ps. The new phase than expands through the sample volume towards the substrate interface. This is the fastest time scale extracted from the fit of the X-ray data, and for this reason we consider it as the limit time scale for the expansion of the ferromagnetic phase under our experimental conditions.This statement finds good agreement with the model we proposed for the magnetization dynamics probed via time resolved MOKE. The model consists of two processes, nucleation and alignment of the magnetic moments, each one governed by a time constant. The fact that the structural nucleation time constant and the magnetic one are found to be the same within the error bars for all the fluences suggests the proposed model gives an accurate and reliable description of the phase transition. Furthermore we can conclude that for FeRh thin films optically excited with an ultra-fast laser pulse, and with a probed circular area with a diameter of 20 μm, no ps or sub-ps onset of the FP can be observed. Ju and coworker observed a sub-picosecond rise in the magnetic signal in [6]. The difference with our result can be due to the difference in the spot diameter since they focused the probe beam down to 3 μm. The observed magnetic contrast on the ps time scale most likely comes from the misalignment of the magnetic moments of the AFP induced by the pump pulse. The time scale of the alignment turns out to be longer that the nucleation one, ranging from 50 ps up to 74 ps. The observed fluence dependence can be caused by the incomplete development of the transition since the used fluences turn

out to be too low.

The interpretation of the reflectivity, and in particular of the so called "lattice contribution" to the reflectivity still remains quite difficult. Since the data are well described by a double exponential function with two time constants one can suppose that they are related with the structural expansion and with the onset of the FP. The value of τ_1 of the reflectivity is smaller than that extracted from the XRD: $\tau_1^{\text{refl}} = 8.1\text{ps} < \tau_1^{\text{XRD}} = 14\text{ps}$. This implies that the reaction of the reflectivity to the excitation is faster the the structural one. Furthermore the similarity between τ_2 of the reflectivity and the alignment of the magnetization extracted from the MOKE data is also poor. In fact τ_2 is found to have a stronger dependence on the fluence and the range of it values is bigger: $20 < \tau_2^{\text{refl}} < 140$ ps while $50 < \tau_2^{\text{MOKE}} < 74$ ps. Even if a correlation between the reflectivity, the lattice expansion and the magnetization order is quite probable, the actual dependence is non trivial. This brings us to the conclusion that a deeper understanding of the reflectivity data requires a model that takes into account the modification of the electronic band structure and the change in the allowed optical transitions.

References

[1] S. O. Mariager, F. Pressacco, A. Caviezel, E. Möhr-Vorobeva, P. Beaud, S. L. Johnson, C.J. Milne, E. Mancini, S. Moyerman, E: E: Fullerton, R. Feidenhans'l, C. H. Back, and C. Quitmann. Structural and magnetic dynamics of a laser induced phase transition in FeRh. *Phys. Rev. Lett*, 108(1):087201, 2012.

[2] J. U. Thiele, M. Buess, and C. H. Back. Spin dynamics of antiferromagnetic-to ferromagnetic phase transition in FeRh on a sub-picosecond time scale. *Appl. Phys. Lett*, 85(14):2857, 2004.

[3] B. Bergman, G. Ju, J. Hohlfeld, R. J. M. van de Veerdonk, J.-Y. Kim, X. Wu, D. Weller, and B. Koopmans. Identifying growth mechanism for laser-induced magnetization in FeRh. *Phys. Rev. B*, 73:060407R, 2006.

[4] S. Maat, J.-U. Thiele, and E. E. Fullerton. Temperature and field hysteresis of the antiferromagnetic-to-ferromagnetic phase transition in epitaxial FeRh films. *Phys. Rev. B*, 72:214432, 2005.

[5] E. Beaurepaire, J.-C. Merle, A. Daunois, and J.-Y. Bigot. Ultrafast spin dynamics in ferromagnetic nickel. *Phys. Rev. Lett*, 76:4250, 1996.

[6] G. Ju, J. Hohlfeld, B. Bergman, R. J. M. van de Veerdonk, O. N. Mryasov, J.-Y. Kim, X. Wu, D. Weller, and B. Koopmans. Ultrafast generation of ferromagnetic order via laser-induced phase transformation in FeRh thin films. *Phys. Rev. Lett.*, 93:197403, 2004.

[7] H. E. Elsayed-Ali, T. B. Norris, M. A. Pessot, and G. A. Mourou. Time-resolved observation of electron-phonon relaxation in copper. *Phys. Rev. Lett.*, 58:1212, 1987.

[8] J. Hohlfeld, S.-S Wellershoff, J. Guedde, U. Conrad, V. Jaenke, and E. Matthias. Electron and lattice dynamics following optical excitation of metals. *Chem. Phys.*, 251:237, 2000.

[9] F. Banfi, F. Pressacco, B. Revaz, C. Giannetti, D. Nardi, G. Ferrini, and F. Parmigiani. Ab initio thermodynamics calculation of all-optical time-resolved calorimetry of nanosize systems: Evidence of nanosecond decoupling of electron and phonon temperatures. *Phys. Rev. B*, 81:155426, 2010.

[10] G. Tas and H. J. Maris. Electron diffusion in metals studied by picosecond ultrasonics. *Phys. Rev. B*, 49:15046, 1994.

[11] S. Wu, P. Geiser, Jun. J., J. Karpinski, and Sobolowski. R. Femtosecond optical generation and detection of coherent acoustic phonons in GaN single crystals. *Phys. Rev. B*, 76:085210, 2007.

[12] J. S. Kouvel and C. C. Hartelius. Model of the antiferromagneitc-ferromagnetic transition in FeRh alloys. *J. Phys. F*, 2:337, 1972.

[13] S. O. Mariager. *Ph.D. Thesis*. PhD thesis, Niels Bohr Institute, Copenhagen, 2010.

[14] C. Thomsen, H. T. Grahn, H. J. Maris, and J. Tauc. Surface influenced magnetostructural transition in FeRh films. *Phys. Rev. B*, 34:4129, 1986.

[15] J.W. Kim, P. J. Rayn, Y. Ding, L. H. Lewis, M. Ali, C. J. Kinane, B. J. Hickey, C. H. Marrows, and D. A. Arena. Surface influenced magnetostructural transition in FeRh films. *Appl. Phys. Lett.*, 95:222515, 2009.

[16] M. Avrami. Kinetics of phase change I. *Jour. Chem. Phys.*, 7:1103, 1939.

[17] M. Avrami. Kinetics of phase change II. *Jour. Chem. Phys.*, 8:212, 1940.

[18] J. Y. Rhee and D. W. Lynch. Optical properties of FeRh alloys. *Phys. Rev. B*, 51:1926, 1995.

Chapter 6

Time Resolved Magnetization Curves on FeRh

The goal of this chapter is to supply more detailed information on the magnetization dynamics in FeRh. In order to gain a deeper understanding of the magnetization dynamics, we measure the magnetization curves as a function of time delay. This detection scheme is of standard use to investigate the demagnetization in ferromagnetic materials [1, 2]. In this case the measured curve is an hysteresis loop. In the particular case of FeRh, an an-hysteretic curve is measured due to the presence of the phase transition, allowing to access the magnetic susceptibility on a sub-nanosecond timescale. It will be shown that such a measurement is equivalent to the time resolved curves presented in the previous chapter. This allows to discuss the laser induced magnetization dynamics as a function of applied field. The results presented in this chapter will be part of a publication which is, at the moment, under preparation.

6.1 Experiment

Using the time resolved MOKE setup described in Chapter 3, we measured the magnetization curves on Pt1 excited at a fixed fluence of 3.5 mJ/cm^2 in a time delay range of 2.5 ns at 33 different time delays. Such curves have been measured by keeping the time delay fixed while sweeping the external field between the opposite values of $\pm$ 2000 Oe [1]. The results are sketched in Fig.6.1. First, we extracted the value of the Kerr rotation at each time delay for H$_{ext}$=2000 Oe, and plotted it as a function of the time delay. The curve obtained, Fig.6.1(a), is similar to the curves measured in the TR-MOKE experiments reported in Chapter 5. It can be seen that the magnetization is close to zero up to 40 ps. Then the signal increases and reaches a maximum after approximately 400 ps. The signal decreases slowly up to 800 ps, when a more pronounced exponential decay starts.

[1] In this chapter the external field **H** is measured in Oersted [Oe], where $1\,Oe = \frac{1}{4\pi}\,\frac{kA}{m}$.

In Fig.6.1(b)-(e) the measured curves at selected time delays are plotted. As expected at -4 ps, the system is in AFP and no magnetic signal can be measured with the applied fields. As discussed in chapter 5, the magnetic signal from the FP can be measured only after 40 ps. By measuring the magnetization curves at time delays greater then 40 ps, we experimentally demonstrate that they are all hysteresis free. This fact can be understood by taking into consideration what happens during the measurement. We perform a stroboscopic experiment in which the value obtained is the result of an average over a certain number of events. In our case the event is the excitation of the system with an ultra-fast laser pulse, from its ground-state and the relaxation back to the initial condition. With this definition in mind one can notice that in FeRh each event implies a transition from an AFP to a FP during the excitation and the transition from the FP to the AFP during the relaxation. This happens under external conditions which we control, such as the delay at which we probe the system and the external field in which the system is embedded. If we suppose to fix a delay t^* and an external field H^*, the Kerr rotation that we measure is induced by the magnetization configuration[2] which is the result of the nucleation and expansion of the FP starting from the AFP in a field H=H^* until t=t^*. The magnetic configuration which gives the Kerr rotation of a single event is completely lost when the system relaxes back to the AFP, due to the phase change. The following pulse will start a process that originate a completely new magnetic configuration, but, for a fixed value of t^* and H^*_{ext}, the average effect on the probe pulse will be the same. Namely, events that happen under the same external conditions will induce the same Kerr rotation. This is the basic assumption for a stroboscopic experiment: under the same external conditions, the system response is the same. Pearson and coworkers have shown that the measurement of the "true" an-hysteretic curve of a ferromagnetic material can be performed when the system is thermally demagnetized (TD) before the application of the external field [3]. In the cited work, a sample is thermally demagnetized when it is heated above the Curie temperature, where the magnetic configuration is completely destroyed, due to the transition to the paramagnetic state. This is in perfect analogy with our experiments: thanks to the anti-ferromagnetic ground state of FeRh, each event implies that the system is thermally demagnetized before performing the new measurement. We want to stress that this possibility is peculiar to FeRh and to each system that shows a phase transition similar to that in FeRh. One can distinguish between two different types of an-hysteretic curves, depending on the experimental process with which they are measured. Following the description of Bertotti in [4], the *initial* or *normal* magnetization curve is obtained by applying a cyclic external field of variable amplitude (Alternate Field Method AFM), starting from $H_{ext} \gg H_c$ and going down to $H_{ext} = 0$. The *virgin* magnetization curve is obtained by first heating the system above the Curie temperature and then cooling the system in an applied external field (thermal demagnetization TD). It has been shown that the two curves are not completely equivalent: in particular, the AFM is prone to an pin-

[2]where for magnetization configuration we mean the distribution and the orientation of the magnetic domains

ning effects of the domain walls which prevent the system to reach its thermal equilibrium magnetic configuration [3]. We can thus conclude that the an-hysteretic magnetization curves measured in our experiments corresponds to the the virgin curves at different time delays.

Lets now consider some special cases. If we do not apply an external field when we induce the phase transition, as discussed in chapter 5, the ferromagnetic domains will nucleate with a random orientation of the local magnetization, implying a zero net magnetization within the probed volume, hence no Kerr rotation will be induced in the probe pulse. This implies that, if H_{ext}=0, the Kerr signal will be zero for all delay times t> 0. This explains the absence of hysteresis in the measured magnetization loops, since all the magnetization curves are measured by continuously sweeping the field from -2000 Oe up to 2000 Oe. If $H_{ext} \neq 0$, it will tend to rotate the moments along the same direction, inducing a net magnetization in the system. For this reason we can measure a Kerr rotation different from zero only when an external magnetic field is applied. Armed with this explanation, we can further interpret the observed magnetization curves. In (c) and (d), for t=64 and t=119 ps, it can be noticed that the curves do not have reached the saturation, implying a non complete alignment of the magnetic moments even for the maximum applied field. The curves saturate after 219 ps, (e)-(g), and reach their maximum value at 344ps. During the relaxation, the shape of the curve remains constant except for their amplitude. At this stage the nucleation and expansion of the AFP takes place which reduces the absolute value of the magnetization.

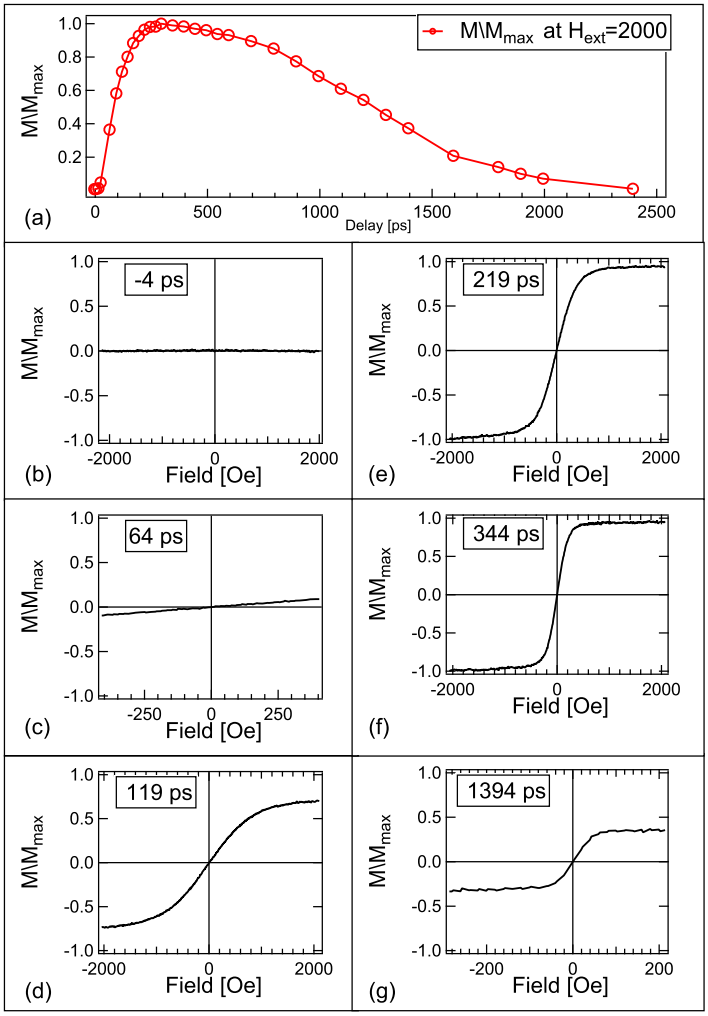

Figure 6.1: (a) Kerr rotation measured on Pt1 as a function of time delay. The values have been extracted from the magnetization curves for $H_{ext} = \pm 2000$ Oe. (b)-(e) Magnetization curves for selected time delays.

6.2 Susceptibility and Magnetization

From the an-hysteretic magnetization curve one can extract the susceptibility of the FeRh film during the phase transition [4]. The susceptibility is a dimensionless quantity which gives the magnetic moment induced by an external field $\mathbf{H}_{ext}$ per unit volume [5]. We evaluate the initial susceptibility as

$$\chi = \lim_{H\to 0} \frac{M(H) - M(0)}{H} \tag{6.1}$$

Experimentally, we estimated χ by taking a minimum value of H=40 Oe, which corresponds to the minimal field increment used in this experiment. The results are reported in Fig,6.2(a). To interpret the measured data we made the following assumptions. First, the system, after 2 ps, has a temperature T$\gg T_{AFP\to FP}$ (where $T_{AFP\to FP}$ is the minimal temperature at which the nucleation of the FP starts, see Chapter 3). This assumption is based on the consideration that on such time scales the energy delivered to the electronic system from the laser pulse has been redistributed to the other two subsystems by the electron-phonon and electron-magnon interaction (this argumentation is based on the Three-Temperature Model, 3TM, see Chapter 1). The temperatures of the electrons, phonons and spins will be in mutual equilibrium, meaning that one can unambiguously define a system temperature as for the static measurements. Due to thermal diffusion the temperature of the probed area will start to decay back to room temperature (RT). It is important for further considerations to keep in mind that the temperature will always be decreasing after the first 4-5 ps. Second, the magnetization curves can be fitted with a Langevin function $L(y)$ which is usually used to model the behavior of the magnetization in paramagnetic systems. Since the fluence used in these measurements is insufficient to fully develop the FP, we assume that in the probed volume FP domains are present immersed within the AFP. The average distance between the domains is large enough to assume that they are independent from one another, and interact only with the external field. Under this conditions the following approximation holds

$$M(H) = M_S L(y) = M_S \left(\coth(y) + \frac{1}{y}\right) \tag{6.2}$$

where y=$\mu_0\mu_{at}$ H/k_BT, M$_S$= n μ_{at}, μ_{at} is the average magnetic moment per ion in the unit cell [3], and n the FP atom density. It can be show that for small external fields, one can derive an expression for the susceptibility by taking the first order in the expansion of Eq.6.2 around y=0. The following relation holds

$$\chi(H=0) = \frac{n\mu_0\mu_{at}^2}{k_b T} \propto \frac{M}{T} \tag{6.3}$$

where $M = n\mu_{at}$. In Fig.6.2(a) the susceptibility has been plotted together with the Kerr

[3] in Chapter 3 we have shown that in the FP the Fe ions carry a magnetic moment of 3.1 μ and the Rh ions carry a magnetic moment of 0.9 μ. We thus assume that the average magnetic moment per ion

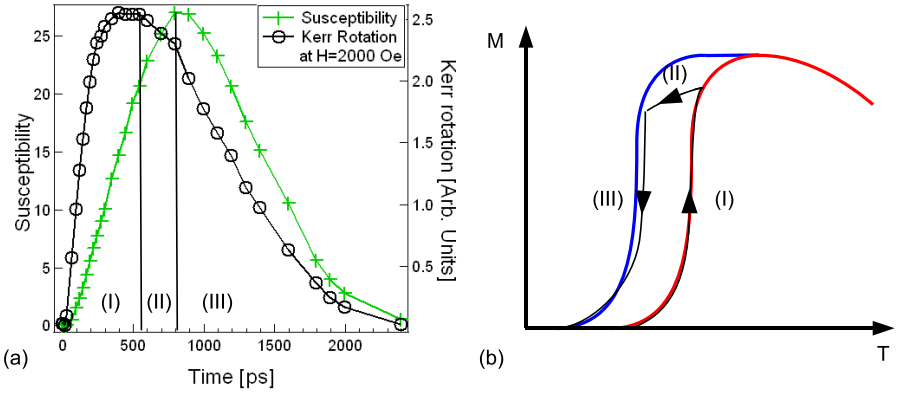

Figure 6.2: (a) The susceptibility χ and the Kerr rotation at H_{ext}=2000 Oe extracted from the magnetization curves are plotted as a function of time delay. The plot has been divided into three regions (I)-(III) depending on the relative behavior of χ and M_S. (b) A sketch of the path (black curve) followed by the system on the M(T) curve. Each section of the path corresponds to a region in (a).

rotation measured at the maximum applied field H_{ext}=2000 Oe which we assume is the value of the saturation magnetization M_S. The plot has been divided into three different regions, depending on the behavior of χ and M_S. A schematic plot of the path followed by the system in the M(T) graphic is plotted in Fig.6.2(b). In region (I), even if $T > T_{FP}$ the magnetization onset is still developing, reaches its maximum after 344 ps, and stays close to this value up to 550 ps. Since the magnetization of the system is increasing and the temperature decreasing, from Eq.6.3 the value of χ is expected to increase. In region (II), the temperature decreased enough to induce a reduction of FP with a reduction of the dimensions of the ferromagnetic domains. This implies a reduction of the magnetization of the system but, due to magnetic inertia (see discussion in Chapter 3), this process is slower than the decrease of temperature. For this reason from 550 to 800 ps, while the magnetic signal decreases, the susceptibility continues to increase, reaching its maximum at 800 ps. In region (III), the temperature of the system is expected to be close to room temperature, hence, due to the exponential nature of the decay of temperature (predicted by simulations on the thermal dynamics in thin films [6]), it will slowly approach room temperature. On the other hand, the reduction of the FP is much more pronounced, as can be seen from the M_S curve. For this reason after 800 ps the susceptibility decreases back to zero with a behavior that mimics the decay of M_S. Within the assumption we

in the unit cell is $\mu_{at} \approx 2\ \mu$.

made, our interpretation of the results gives a plausible description of the process and explains the observed behavior of the susceptibility.

6.3 Field dependent Magnetization Dynamics

Having measured the magnetization curves for a fixed fluence at different time delays implies to have the Kerr rotation as a function of two variables, namely the time delay t and the external field H_{ext}. This allows us to plot the results of the experiment as a surface in two dimensional space: $\Delta\theta_K = \Delta\theta_K(t, H_{ext})$. The obtained surface is plotted

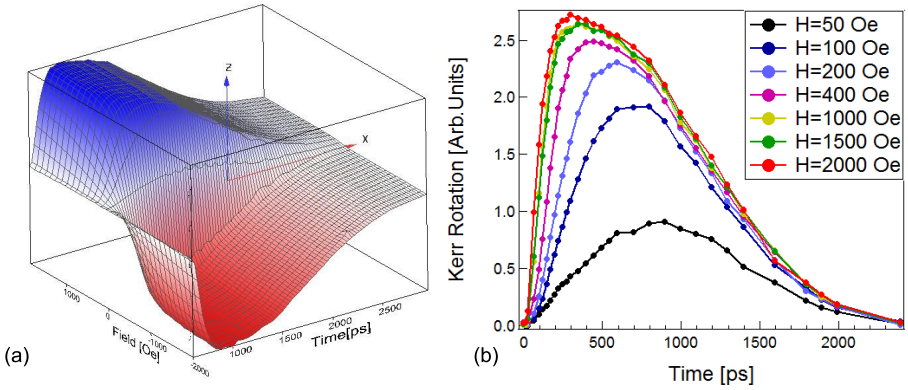

Figure 6.3: (a)The interpolated surface derived from the magnetization loops measured at different time delays. Each point on the surface is the Kerr rotation induced by the magnetization in the sample at a fixed time t and at a fixed field H. (b) Time resolved Kerr curves extracted from the surface for a selection of external fields.

in Fig.6.3(a). It is now possible to extract the value of the Kerr rotation for a fixed value of the field at every measured time delay from the data. Namely, setting $H_{ext} = H^*$, the corresponding $\Delta\theta_K(t, H^*)$ will be a time dependent Kerr curve, like the ones described in Chapter 5, where every curve has a different maximum applied field. This implies that from the magnetization curves one can extract a set of time resolved Kerr curves measured for different values of the external field. The results for a selected set of external field values are reported in Fig.6.3(b). The curves show the same behavior of the TR-Kerr curves, in particular the signal starts from zero and increases up to a maximum value, reached on the hundred ps scale. The signal starts to relax back to zero with an exponential decay. It can clearly be noticed that both the value of the maximum and the dynamics in the time range from zero up to the delay in which the maximum

is achieved, show a strong dependence on the external field. On the other hand, the relaxation process shows an exponential decay with nearly the same time constant for each value of H_{ext}. This confirms that in the relaxation phase the magnetization dynamics is driven by the thermal process. The reduction of the temperature in the probed volume will cause a nucleation and an expansion of anti-ferromagnetic domains, with a consequent reduction of the magnetization. By fitting the relaxation with an exponential function $f(t) = A * exp(-(t-t_0)/\tau_d)$ where τ_d is the decay time constant, we obtain for $H_{ext} > 100$ Oe $\tau_d = 889 \pm 29$ ps. At lower fields we had to reduce the fitting range due to the late attainment of the maximum, resulting in a worse fit quality (see the curve H=50 Oe in Fig.6.3(b)). This results has not been taken into account in the calculation of the average value of the decay time. In order to study the field dependence of the Kerr signal from the external field, we extracted the maximum position and the slope of the rising part of the signal for each value of the applied field. The results are plotted in Fig.6.4. Since we measured the magnetization curves only at 33 different time delays, the time resolution of the curves is quite low. This has two consequences. First, the determination of the maximum has an uncertainty of about 50 ps. This can be noticed in Fig.6.4(a), where the time delay of the maximum is reported as a function of the applied field. The poor time resolution turns out in a high level of noise for the position of the maximum. Nevertheless, a trend is clearly visible. At low fields (20-40 Oe) the signal reaches the maximum 800-900 ps after laser excitation. As the field increases the maximum is reached faster, up to 600 Oe where the dependence of the position of the maximum on the external field il less marked. We estimated the average value of the delay of the maximum for H>600 Oe as 329±44 ps. The second consequence is that the lack of resolution prevented us to apply the model described in Chapter 5 to these magnetization curves. Instead of extracting the time constant as before, we estimated the maximum value of the slope σ, by numerically differentiating the MOKE curves. The slope is defined as follows

$$\sigma(H) = \frac{M(t_2, H) - M(t_1, H)}{t_2 - t_1} \tag{6.4}$$

The maximum of the derivative, estimated in this way, is always achieved within the first 100 ps, meaning that the following discussion will deal with the effect of the external field on the FP onset and with the alignment of the moments. Since the Kerr signal is proportional to the ferromagnetic volume fraction aligned with the external field, the slope gives the rate of expansion and alignment of the FP. The results are reported in Fig.6.4(b). Two regimes can be identified. In the first, up to H_{ext}=600 Oe, one observes a linear increase of the expansion rate starting from zero. This means that the increase of the field is very effective in accelerating the process of alignment of the magnetic moments. For larger fields (600 up to 2000 Oe) the expansion rate still steadily increases with the field, but the dependence is less pronounced. We observe no saturation in the increase of the expansion rate for the investigated field range, suggesting the the expansion rate can be further increased with stronger external fields.

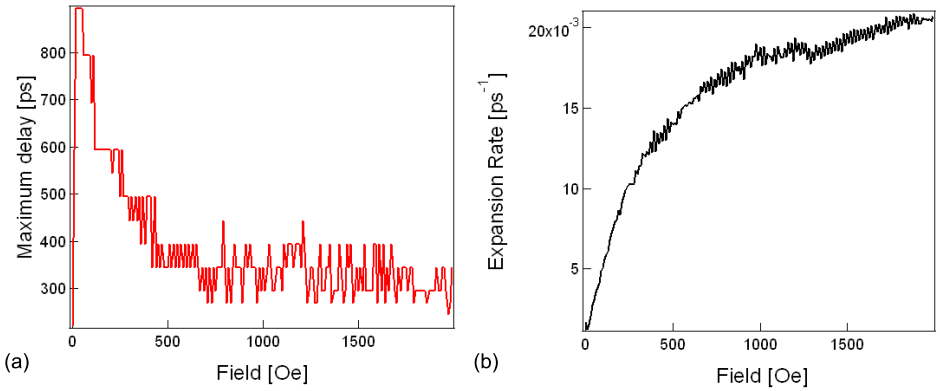

Figure 6.4: (a) Time delay at which the maximum Kerr signal is reached as a function of the external field. (b) The numerically evaluated maximum slope of the Kerr signal as a function of the applied field.

So far this is the first time that a study of the magnetization dynamics as function of the external field, applied in the plane of the film, has been carried on the FeRh system in such a detailed way. Bergmann an coworkers performed time resolved MOKE experiments with an experimental setup similar to our, but with the external field applied at 45° from the surface normal. They observed a oscillation in the Kerr rotation on the 100 ps range, which changed frequency as a function of the external applied field: they interpreted the observed behavior as a precession of the magnetization with a Larmor frequency dependent on the applied external field, during the process of alignment with the external field [7]. We applied a field in the plane of the sample and we observed no oscillations during the alignment process. This suggests that the oscillatory behavior is present only if the magnetization is forced out of the sample plane by the external field. In this case the magnetization precess around the demagmetizing field $\mathbf{H}_d$, which for a thin film has a component different from zero only in the the direction normal to the sample plane (see Section 1.3). Maat and coworkers report the effect of the application of high external fields on the transition temperature of a $Fe_{49}Rh_{51}$ thin film grown on MgO and on sapphire [8]. They show that a negative shift of the transition temperature is induced by the external field and they estimate a regression coefficient of -8 K/T, which is consistent with previous measurements on bulk samples [9]. Moving the transition temperature towards lower values means that the application of an external field eases the transition: one has to supply a smaller amount of energy to induce the phase transition if an external field is present. We want to stress that in our measurements we investigate the

dynamics with which the ferromagnetic phase develops while the previously cited works had performed static experiments. Nevertheless, since every measurement we performed has been made with an applied external field, a decrease of the transition temperature is present: for our applied field a shift of -2 degrees of the transition temperature is expected. This is consistent with the observed behavior of the maximum position for fields lower than 500 Oe. Our interpretation of the origin of the magnetization dynamics during the phase transition is based both on the expansion of the ferromagnetic volume fraction and on the rotation of the local moments within the ferromagnetic domains. It is legitimate to expect that the rotation of the moments will depend on the intensity of the external field and a stronger field will be more effective in re-aligning the local moments. Our experiments show that in this process one can identify two regimes.The up to 600 Oe the increase in the field intensity speeds up the process. For fields larger than 600 Oe the maximum delay seems to reach a constant value. Due to the high level of noise in the reported data, we can not exclude that a trend pushing the maximum position towards earlier delays is present for higher fields. Furthermore, the magnetization curves measured within the first 100 ps show no saturation at our maximum applied field. This suggests that the application of stronger external fields will modify the observed behavior of the magnetization in the first 100 ps. On the other hand, the rate at which the process develops, which we estimate as the slope of the Kerr curve during the increase of the signal, increases for each field we applied.

References

[1] E. Beaurepaire, J.-C. Merle, A. Daunois, and J.-Y. Bigot. Ultrafast spin dynamics in ferromagnetic nickel. *Phys. Rev. Lett*, 76:4250, 1996.

[2] E. Carpene, E. Mancini, C. Dallera, M. Brenna, E. Puppin, and S. De Silvestri. Dynamics of electron-magnon interaction and ultrafast demagnetization in thin iron films. *Phys. Rev. B*, 78:174422, 2008.

[3] J. Pearson, P. T. Squire, and D Atkinson. Which anhysteretic magnetization curve? *IEEE transaction on magnetics*, 33(5):0018–9464, 1997.

[4] G. Bertotti. *Hysteresis in Magnetism.* Accademic Press, 1998.

[5] S. Blundel. *Magnetism in condensed matter.* Oxford University Press, 2001.

[6] F. Banfi, F. Pressacco, B. Revaz, C. Giannetti, D. Nardi, G. Ferrini, and F. Parmigiani. Ab initio thermodynamics calculation of all-optical time-resolved calorimetry of nanosize systems: Evidence of nanosecond decoupling of electron and phonon temperatures. *Phys. Rev. B*, 81:155426, 2010.

[7] B. Bergman, G. Ju, J. Hohlfeld, R. J. M. van de Veerdonk, J.-Y. Kim, X. Wu, D. Weller, and B. Koopmans. Identifying growth mechanism for laser-induced magnetization in FeRh. *Phys. Rev. B*, 73:060407R, 2006.

[8] S. Maat, J.-U. Thiele, and E. E. Fullerton. Temperature and field hysteresis of the antiferromagnetic-to-ferromagnetic phase transition in epitaxial ferh films. *Phys. Rev. B*, 72:214432, 2005.

[9] I. A. Zakharov, A. M. Kadometseva, R. Z. Levitin, and E. G. Ponyatovskii. Magnetic and magnetoelastic properties of a metamagnetic fe-rh alloy. *Sov. Phys. JEPT*, 19:1348, 1964.

Chapter 7

Conclusion and outlook

7.1 Conclusions

In this thesis the magnetization dynamics and the structural dynamics in thin films of FeRh has been investigated with TR-MOKE, TR-XRD, and FMR while the system has been driven across the first order phase transition.

First we performed temperature dependent FMR which allowed us to determine the damping constant of the system in the ferromagnetic phase and to confirm the first order nature of the transition. Furthermore we where able to determine the anisotropy constants of the material which were not previously reported in the literature. The TR-MOKE and TR-XRD experiments addressed the magnetization and the lattice dynamics triggered by a laser pulse. This allows us to selectively determine the timescales governing the development of the ferromagnetic phase. We demonstrate how a single exponential law can well describe the structural phase transition. For the magnetic transition we propose a model which consists of two distinct steps: the onset of the magnetic phase happens with a nucleation of magnetic domains with a random orientation of the local magnetization, which then tends to align with the external field. The intensity of the field has a strong influence on the alignment process: we demonstrated how by increasing the field intensity the time it takes for the local magnetic moment to align is reduced. We further demonstrate how it is possible to access the magnetic susceptibility of the system during the transition by measuring the magnetization curves as a function of the time delay.

In chapter 4 we have reported the results of the FMR experiments. From the comparison of the temperature dependence of the integral of the FMR line-shape with the M(T) curve measured with static MOKE we were able to confirm the first order nature of the transition. The measured line-width shows an increase when the temperature of the system approaches the critical temperatures. We argue that this can be induced by the inhomogeneities induced in the system by the formation of domain boundaries when

the two phases coexists.

After setting the system in the ferromagnetic phase, we studied the angular dependence of the FMR line-shape position and of the line-width. From these measurements the value of the anisotropy constants were extracted. Even if films of FeRh show an easy-plane in the film plane, we observed a fourfold anisotropy, which we attribute to the strain induced by the substrate due to a lattice constant mismatch. From the angular dependence of the resonance field we extracted the g-factor of FeRh γ=2.05±0.06. The study of the angular dependence of the line-width we demonstrate that the two-magnon process is active and gives a large contribution to the damping.

The frequency dependence of the resonance field and of the line-width done in perpendicular configuration allows us to determine the damping constant α of FeRh. We found a value surprisingly small of α=0.0013±0.0008.

In chapter 5 the magnetization and the structural dynamics of the AFP to FP transition in a FeRh thin film are discussed. We were able to observe the growth of the new phase and the coexistence of the two phases after laser excitation. By the comparison of the TR-XRD and the TR-MOKE data we were able to identify two distinct time scales, one relative to the nucleation of the ferromagnetic phase and a second one related to the expansion of the new phase and to the alignment of the atomic moments with the external field. We developed a model that can describe both the nucleation of the ferromagnetic phase and the realignment of the magnetic moments. This model follows the interpretation given by Bergmann and coworkers in their PRB of 2006.

In chapter 6 we report the measurement of the magnetization curve during the evolution of the transition. We show how the measured curves are equivalent to the first magnetization curve measured statically. From these curves we were able to extract the susceptibility of the system during the transition. We demonstrate how one can extract the field dependence of the time evolution of the Kerr signal from the measured magnetization curves, and hence the expansion of the ferromagnetic phase together with the realignment process. We show how the speed of the realignment process increases with the field intensity.

7.2 Outlook

In the last 5 years the FeRh system has again attracted the interest of the magnetism community, both on a theoretical and experimental point of view. Since there is a tight interplay of electrons, phonons and magnons during the phase transition many theoretical group investigated the electronic and magnetic properties of this system using density functional theory (DFT), ab-initio or MonteCarlo simulations to provide an insight in the driving mechanism of the transition. Nevertheless a comprehensive picture of the basic

physical mechanisms is still missing.

On the experimental point of view, the amount of data on the phase transition is large. Thanks also to this work the timescales of the dynamics of the transition in thin film is known with a certain accuracy. This can be considered the starting point for future developments. In particular, two are the field in which the research on FeRh is moving. Different research groups are now able to produce nano-structures of FeRh which show the phase transition discussed in this work. The aim is to determine if a constrained geometry influences the time scale of the transition and if is possible to effectively control the nucleation process and the orientation of the magnetization during the onset.

A second field of research is that of the magnetic multi-layers, and in particular the FePt/FeRh bilayer. It is known that FePt has a strong out-of-plane anisotropy which forces the magnetic moments to be perpendicularly oriented with respect to the film plane, but is difficult to switch the magnetization. The presence of the FeRh layer discloses the possibility of generation of a local in-plane magnetic field generated only during an ultra fast laser excitation. This field will interact with the FePt magnetization making the switching process easier. This system has already been studied in the past, but the recent progress in the growth and fabrication of the layers will probably improve its efficiency, making it a good candidate for the Heat Assisted Magnetic Recording Devices.

Appendix A

Demagnetization Dynamics in FeRh

In order to give a complete description of the magnetization dynamics in FeRh, we measured the laser induced demagnetization with the Magneto-Optic Kerr Effect. In usual ferromagnets this is one of the most used experimental techniques to investigate the interplay of electron, phonon and magnetic system. The origin of the ultra-fast demagnetization is still under debate, and different models have been proposed. Each model identifies a certain mechanism as responsible for the redistribution of the angular momentum in the system: electron-phonon scattering [1], angular momentum transfer from the photons to the magnetic system [2], or super-diffusive dynamics of the spin polarized electron gas [3]. To perform this experiment on FeRh, the system needs to be in the ferromagnetic phase. For this reason we set the temperature of the system to T=420 K, which is well above T_{FP}. In this case no phase transition is involved and the system is expected to behave like a normal ferromagnet. We performed the measurements for three different fluences (0.8, 1.2 and 2.8 mJ/cm^2), and the results are reported in Fig.A.1. As it can be seen the demagnetization is completed within the first ps, as expected for such process. To extract the time constant of the demagnetization process we we use the following fitting function [4]

$$f(t) = G(t) \otimes \left[A * (1 - exp(\frac{t - t_0}{\tau_D})) + B * exp(\frac{t - t_0}{\tau_R}) \right] \tag{A.1}$$

where G(t) is the temporal shape of the laser pulse given by a Gaussian distribution with a FWHM of 200 fs[1], and $\otimes$ indicates the convolution operator. A and B are proportionality constants satisfying the relation $A \gg B$. In the exponential dependence one assumes that the demagnetization process develops with a time constant τ_D and the re-magnetization with τ_R. This function describes only a demagnetization and a following first re-magnetization which is usually accomplished within the first few ps, for this reason we fit the measured curves only within the first 1 ps. We fit the curves up to this delay, and the results are reported in Tab.A.1. As expected the demagnetization time constant

[1]The pulse duration has been determined with an APE mini autocorrelator right after the output window of the laser

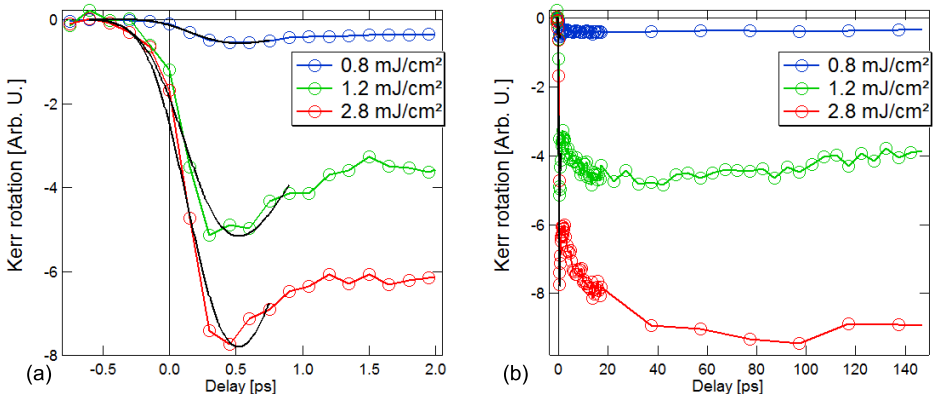

Figure A.1: (a) Fluence dependent measurement of the demagnetization in FeRh plotted in the first 2 ps. (b) The recovery of the magnetization on the hundred ps time scale as a function of fluence.

Fluence mJ/cm^2	τ_D [fs]	τ_R [ps]
0.8	103.4	12.6
1.2	132.7	6.38
2.8	157.6	5.93

Table A.1: List of the demagnetization and re-magnetization time constants extracted from the fit.

τ_D is on the order hundred femtoseconds and it increase with fluence. Since we can only record a limited number of experimental points on the femtosecond scale the uncertainty on the value does not allows us to make any detailed discussion of the results. We can say that the demagnetization in FeRh under our experimental conditions has a time constant of about 130 $\pm$ 20 fs. In Fig.A.1(b) the re-magnetization dynamics is reported up to 150 ps after the excitation. For 0.8 mJ/cm^2 the re-magnetization is monotonic towards zero. For the two other fluences the observed behavior is quite different. After fast demagnetization depicted in Fig.A.1(a), the recovery of the signal slows down up to 2 ps after the excitation. After this delay the signal decreases again but with a slower dynamics until reaching a second minimum: for 1.2 mJ/cm^2 the minimum is reached at 40 ps, while for 2.8 mJ/cm^2 at 100 ps. The signal then starts a slow recovery that is completed on the ns time scale. This behavior is quite unusual for the re-magnetization dynamics. We are not aware of other experimental observations, or theoretical predictions, of the described behavior. Roth and coworkers in [5] propose a model to describe the two-steps demag-

netization dynamics observed in a time-resolved MOKE experiment for high fluences (5 mJ/cm^2) in Ni. This model can account for demagnetization with a time scale up to tens of ps. The analogy with our observed dynamics is quite poor since the mentioned model does not predict any re-magnetization on the ps scale but just a monotonic decrease down to a minimum. Up to know we can not further speculate on the origin of the observed behavior, but such a phenomenon deserves further investigation both on experimental and theoretical sides.

References

[1] B. Koopmans, G. Malinowski, F. Dalla Longa, M. Steiauf, M. Faehnle, T. Roth, M. Cinchetti, and M. Aeschlimann. Explaining the paradoxical diversity of ultrafast laser-induced demagnetization. *Nature Materials*, 10:1038, 2009.

[2] G. P. Zhang and W. Huebner. Laser-induced ultrafast demagnetization in ferromagnetic metals. *Phys. Rev. Lett*, 85:3025, 2000.

[3] M Battiato, K. Karva, and P. M. Oppeneer. Superdiffusive spin transport as a mechanism of ultrafast demagnetization. *Phys. Rev. Lett*, 105:027203, 2010.

[4] I. Radu, C. Stamm, N. Pontius, T. Kachel, P. Ramm, J.-U Thiele, H. A. Duerr, and C. H. ack. Laser-induced generation and quenching of magnetization on ferh studied with time-resolved x-ray magnetic circular dichroism. *Phys, Rev. B*, 81:104415, 2010.

[5] T. Roth, A. J. Schellekens, S. Alebrand, O. Schmitt, D. Steil, M. Cinchetti, B. Koopmans, and M. Aeschlimann. Temperature dependence of the laser-induced demagnetization in Ni- a key for identifying the underlying mechanism. *Phys. Rev. X*, 2:021006, 2012.

Appendix B

What does the static phase transition in FeRh look like!

To investigate the phase transition we imaged the onset of the ferromagnetic phase in FeRh by X-ray magnetic circular dichroism (XMCD) in a photoemission electron microscope (PEEM). The measurements have been performed at the Paul Scherrer Institute in (Villigen, Switzerland) at the beamline SIM, in the group of Prof. Nolting. This technique allows to obtain images with magnetic contrast with a spatial resolution down to 50 nm (for a detailed description of the setup, see http://www.psi.ch/sls/sim/endstations).

We have taken XMCD-PEEM images at different temperatures during heating and cooling cycles on the Pt2 sample. In order to apply an in-plane magnetic field as done in the experiments reported in this work, a set of Co nano-magnets were deposited on the sample surface. The direction of the field in the magnet gap is parallel to the sensitivity axes of the PEEM. In Fig.B.1 the images taken at different temperatures across the transition upon heating are reported. As can be seen in (a) and (b) a diffuse magnetic contrast is observed, which has already been seen on other samples. The increase of temperature induces the nucleation of the ferromagnetic phase and the consequent expansion and coalescence (c)-(e). When the ferromagnetic phase is established a domain is clearly visible in the gap of the magnets (f).

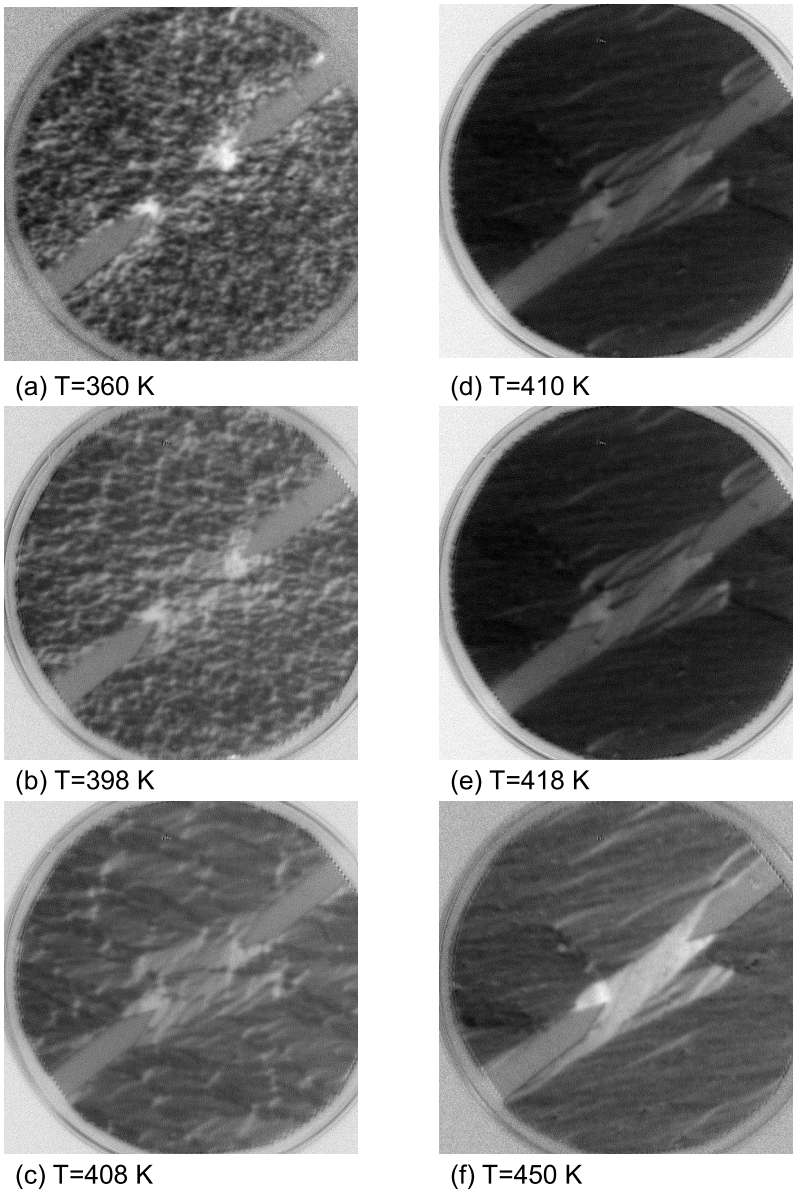

Figure B.1: XMCD images at different increasing temperature of Pt2. The contrast in the picture is proportional to the component of the magnetization along the sensitivity axis of the microscope, which is directed along the long edge of the Co nano-magnets.

Chapter 8

Acknowledgments

Now is time to thank all the persons that I met during my staying in Regensburg and contributed to my work. For this reason I want to thank ...

... Prof. Dr. Christian Back for the possibility to work in his group and for the interesting subject he gave me. He always managed to give me the right motivation for my study and precious advices for the development of my research.

... Dr. Georg Woltersdorf for the fruitful discussions and explanations on the experimental methods and on the theory of the ferromagnetic resonance.

... Dr. Eduardo Mancini for many different things. First for the help and the support in the lab during the constructions of the experimental setup and for sharing the time shifts during the measurements. Furthermore for the precious advices and suggestions during the analysis and interpretation of the data. Second for the good time spent together at the university and in Regensburg (maybe you should go out a bit more....)

... Dr. Jean-Yves Chauleau which together with Eduardo forms the perfect office crew! I liked to share the office with you because of the nice discussions and talks not only about physics. Your passion for music and your good mood, always present except on Mondays when you come back from France, make a really pleasant atmosphere in the office. (Don't worry, we will have occasion to collaborate...)

... Christian Back, Eduardo Mancini and Jean-Yves Chauleau for having read and correct my thesis.

... Dr. Alexander Weber for the introduction he gave me to the world of laser systems and Stefan Guenther for the collaboration in the laser lab.

... Dieter Schierl, Tobias Stoeckl, and Markus Hollnberger for all the technical things. I could not manage it without your advices and help.

... the team of the elektronische werkstat for your quick and effective help with the electronic devices (now I will no more spoil your storage of resistances and thermo-sensors)

... Dr. Simon Mariager, Dr. Gerard Ingold, Prof. Dr.Christof Quitmann and the other members of the FEMTO group at PSI for the TR-XRD measurements.

... Prof. Dr. Fritjof Nolting, Dr. Loic Le Guyader, Michel Buzzi and Simon again for the PEEM measurements at SIM.

... Markus Haertinger and Georg Woltersdorf for support and help during the FMR measurements.

... Dr. Marcello Soda for the precious advices he gave me at the beginning of my staying in Regensburg

... all the members of the Group of Magnetism in the university of Regensburg for the pleasant atmosphere and the nice outdoor activities that have been organized.

... Marie Curie 7FP and the FANTOMAS project that financially supported my studies and gave me the possibility to get in contact with many different research groups and institutions.

... all the friends that I met here in Regensburg. A city is just a collection of houses and building, nothing special. What makes a city special are the persons you know which lives there.

At last some special acknowledgments.

Un pensiero speciale va alla mia famiglia: Guido, Marina, Caterina ed Eleonora. Ci sono tante cose di cui vorrei ringraziarvi e non so da dove iniziare. L'entusiasmo che avete dimostrato durante il mio periodo di studio qui in Germania é stato il miglior aiuto che potevate darmi: mi ha dato la sicurezza e la tranquillitá indispensabili per giungere fino in fondo. Vi ho sempre sentito vicini nonostante la distanza che ci separa. Grazie.

A special thank to Uliana Yazhinova. Having met you here has made this last two years special for me. Thank you for the patience you reserved to me in this last months: now is over, I will be a much more pleasant company.

I want to dedicate this work to this five persons: Guido, Marina, Caterina, Eleonora and Uliana.